

DOTTORATO DI RICERCA IN

IL FUTURO DELLA TERRA, CAMBIAMENTI CLIMATICI E SFIDE SOCIALI

Ciclo XXXVII

Settore Concorsuale: 04/A4 GEOPHYSICA

Settore scientifico disciplinare: GEOS-04/C OCEANOGRAFIA,

METEOROLOGIA E CLIMATOLOGIA

SEASONAL FORECASTING OF EAST AFRICAN RAINS

Presentata da Agumase Kindie Tefera

Coordinatore Dottorato Supervisore

Prof. Silvana Di Sabatino Prof. Antonio Navarra

Co-Supervisore

Dott. Giovanni Liguori

Esame finale anno 2025

PhD scholarship of the National Operational Programme for Research and Innovation 2014-2020 (CCI 2014IT16M2OP005), ESF resources react-eu, Action IV.4 "Doctorates and research contracts on innovation issues" and Action IV.5 "Doctorates on Green topics." CUP: J35F21003110006.

i

ACKNOWLEDGEMENTS

First and foremost, I would like to express my heartfelt gratitude to my supervisors, Prof. Antonio Navarra and Prof Giovanni Liguori, for granting me the opportunity to pursue my PhD under their esteemed guidance. I am deeply appreciative of their unwavering support, continuous encouragement, and insightful mentorship throughout every phase of my research. This achievement would not have been possible without Prof Giovanni Liguori for his great support in every step of my study. Thank you so much for everything

Next, I would also like to extend my sincere gratitude to Prof. Wiliam Cabos, University of Alcalá, Madrid, Spain, for graciously accepting me during my time abroad and for his invaluable remote collaboration and guidance throughout my stay. I would also like to acknowledge the University of Bologna, and European Union, and PON for giving this scholarship.

My acknowledgement also goes to Dario Nicoli, Giovanni Zizi, Massimiliano Drudi, and Antonella Sanna at CMCC for their guidance in programming setups and data preprocessing when I started my research. I would also like to thank Loredana Amato for her support and assistance during my stay, especially for sharing office space at CMCC.

Finally, I would like to express my deepest gratitude to my mother Yelbie Gedif, my father Kindie Tefera and my sister Bezawit Kindie for their great support and encouragement throughout my education. This achievement would not have been possible without their enduring love and support. Last, but not least, I would like to thank my wife, Netsanet Fentahun, for her great support, love, encouragement, and patience in caring for our child during a period of my PhD study. I am also very thankful to my lovely child Mahilet Agumase for her funs and happiness that makes me motivated through my study.

ABSTRACT

In East Africa (EA), rainfall variability has a significant effect on socioeconomic and environmental impacts on the region, making accurate seasonal rainfall predictions essential. This variability particularly impacts rainfed agriculture, which forms the backbone of livelihoods and food security for millions. Rainfed agriculture is particularly vulnerable to erratic rainfall patterns since it depends significantly on seasonal rainfall for crop planting, harvesting, and management. This susceptibility frequently leads to lower yields, food shortages, and severe financial hardship. Global teleconnections such as El Niño-Southern Oscillation (ENSO) and the Indian Ocean Dipole (IOD) have a strong influence on the interannual variability of East African rains. Even though ENSO and IOD are known as the major large-scale atmospheric and oceanic systems that influence the seasonal East African rainfall patterns, the individual roles are not fully understood.

In this work, we evaluated the predictability of East African short rains using model ensembles from the multi-system seasonal retrospective forecasts from the Copernicus Climate Change Service (C3S). We assess the prediction skill for 1- to 5month lead times using forecasts initialized in September for each year from 1993 to 2016. Although most models exhibit significant mean rainfall biases, they generally show skill in predicting OND (October-December) precipitation anomalies across much of East Africa. However, skill is low or absent in some northern and western parts of the focus area. Along the East African coasts near Somalia and over parts of the western Indian Ocean, models demonstrate skill throughout the late winter (up to DJF: December-February), likely due to the persistence of sea surface temperature (SST) anomalies in the western Indian Ocean. Years when models consistently outperform persistence forecasts align with the mature phases of El Niño Southern Oscillation (ENSO) and/or Indian Ocean Dipole (IOD). When tracked using the Dipole Mode Index, this latter mode can generally predict the sign of the rainfall anomaly in all models. Despite East Africa's proximity to the West pole of the IOD, the correlation between short rains and IOD maximizes when both east and west are considered. This finding confirms previous studies based on observational datasets, which indicate that broader-scale IOD variability associated with changes in the Walker Circulation, rather than local SST fluctuations, is the primary driver behind East African rainfall.

In this study we also evaluate the predictability of East African long rainy season since it is a critical period for agricultural sector in the region. Therefore, we assessed the skill of the state-of-the-art seasonal prediction models from the C3S in forecasting East African long rains up to 3 lead seasons: May-March (MAM) to March-July (MJJ) as initialized in February for each year from 1993 to 2016. Using lead-time-dependent anomaly correlation analysis, we identify the years where the model consistently performs better than persistence forecasting. Therefore, we found that long rains have a connection with ENSO phase, showing significant correlations in both observational data and models. Consequently, the C3S seasonal prediction system is more effective at reproducing the long rains, particularly when the ENSO phase is active, compared to periods dominated by IOD phases.

In this study, we also examined the independent roles of ENSO and IOD in influencing the variability of EASR using CESM model experiments. Through partial correlation and composite anomaly techniques, our findings highlight the primary influence of the IOD, with warm (cool) SST anomalies strongly linked to above(below) normal OND rainfall anomaly over EA. In contrast, the direct impact of ENSO is less pronounced and largely dependent on its interactions with IOD. This result was also further confirmed in dynamical models such as CESM_noENSO and CESM_noIOD experiments. Overall, the IOD plays a critical role in shaping East African short-term rainfall variability. Its influence remains significant even when ENSO variability is excluded, highlighting its capacity to drive rainfall anomalies independently.

TABLE OF CONTENTS

ACK	KNOWLEDGEMENTS	ii
ABS	TRACT	iii
LIST	T OF FIGURES	vii
LIST	T OF TABLES	xiv
LIST	「OF ABBREVIATIONS	xv
1 IN	TRODUCTION	1
1.1	East African Rainfall Regimes	1
1.2	Driving mechanisms of East African rainfall variability	4
1.2	2.1 Global teleconnections	4
1.2	2.2 Local drivers	9
1.3	Role of the Intertropical Convergence Zone (ITCZ)	11
1.4	State-of-the-art Seasonal Prediction Systems	12
1.5	Dissertation structure	16
1.6	Objectives	17
2 F	ORECASTING EAST AFRICAN SHORT RAINS	18
2.1	Introduction	18
2.2	Datasets, models, and methods	20
2.2	2.1 Observational data set	20
2.2	2.2 C3s model descriptions	21
2.2	2.3 Skill evaluation method	23
2.3	Model climatology and inter-annual variability	24
2.4	Predictive skill of coupled models	31
2.5	Predictability conditional on ENSO and IOD phases	35
2.6	Discussion and Conclusion	45
3 F	ORECASTING EAST AFRICAN LONG RAINS	48
3.1	Introduction	48
3 2	Datasets models and methods	51

3.3	Model Climatology and Inter-annual variability	.51
3.4	Predictive skill of coupled models	.58
3.5	Predictability conditional on ENSO and IOD phases	.62
3.6	Discussion and Conclusion	.69
	ESTIGATE THE ROLES OF ENSO AND IOD ON EAST AFRICAN T RAIN USING EARTH SYSTEM MODEL EXPERIMENTS	
4.1	Introduction	.71
4.2	Dataset, Model, and Methods	.75
4.2.1	Observational data and CESM experiments	. 75
4.2.2	Method of analysis	. 77
4.3	Rainfall Climatology	.79
4.4	Rainfall variability	.83
4.5	Characterization of ENSO and IOD	.85
4.6	IOD and ENSO Driven East African Short Rain Variability	.90
4.6.1	Positive phases	.92
4.6.2	Negative phase	. 94
4.6.3	Independent roles of ENSO and IOD	. 95
4.7	Discussion and Conclusion	.99
6 GEN	NERAL DISCUSSION	104
neiere	nces	(UU)

LIST OF FIGURES

Figure~2.1~Rainfall~climatology~during~the~short~rains~(OND)~derived~from~GPCP~(i),
ERA5 (j), shown upper panels, and the seasonal prediction systems from
Copernicus Climate Change Service (C3S), which includes 8 ocean-atmosphere
coupled model ensembles and cover the period 1993–2016 (a-h). The lower panel
shows area-averaged OND rainfall anomalies for part of Eastern Africa (30-
50°E, 5°S-10°N; blue dashed box in i) for models, ERA5, and the GPCP dataset.
Anomalies are computed relative to the climatology shown in the upper panel. 27
Figure 2.2 Rainfall standard deviation during the short rains (OND) derived from the
seasonal prediction systems from C3S, which includes 8 ocean-atmosphere
coupled model ensembles and covers the period 1993–2016 (c-j) and GPCP (i), ERA5 (j) datasets28
Figure 2.3 Seasonal mean bias computed as the difference between GPCP and C3S
model predictions for lead season 1 (OND), lead season 2 (NDJ), and lead season
3 (DJF) of rainfall climatology (ensemble mean), which was initialized in
September during 1993-201630
Figure 2.4 Pointwise-correlation maps between GPCP and C3S model predictions for
lead season 1 (October-December: OND), lead season 2 (November-January:
NDJ), and lead season 3 (December-February: DJF) of rainfall anomalies
(ensemble mean) during 1993-2016. Stippling indicates areas where the
correlation between the hindcast and observation is statistically significant at a
90% confidence level, as calculated by a two-sided Student t-test for 22(N-2)
degrees of freedom32
Figure 2.5 Anomaly correlation coefficient (ACC) between GPCP and each C3S model
(a-h; upper panels) for monthly rainfall anomaly over part of Eastern Africa (blue
dashed box of Fig. 1i) for each year (grey lines) from lead month 0 (September)
to lead month 5 (February). In each subfigure, the top three forecasts stand out
with distinct colours: the most accurate year is highlighted in red, the second-best
in blue, and the third-best in magenta. These forecasts are determined by sorting

all predicted years based on their average ACC values across September and
October. The black dashed line indicates the persistence forecast. The lower pane
(i) illustrates the spatial correlation between each model and GPCP rainfal
anomaly patterns for the OND seasonal mean, calculated over Equatorial Eastern
Africa (30–50°E, 5°S-10°N)34
Figure 2.6 SST persistence from lead seasons 1(OND) to 3(DJF) for individual C3.
coupled models. Persistence is quantified in each grid point by the autocorrelation
between the SON and lead season time series37
Figure 2.7 Scatterplot of Niño3.4 index (N34; x-axis) versus Dipole Mode Index (DMI
y-axis) during OND season for each of the 24 years analyzed in both mode
predictions (a-h) and GPCP dataset (i). The area of the circle is proportional to
the absolute value of OND rainfall anomaly averaged over part of Eastern Africa
(blue dashed box of Fig. 2.1i), with positive (negative) anomaly coloured in green
(orange). As in Fig. 2.5 the best forecasted year is highlighted in red, the second
best in blue, and the third-best in magenta. Additionally, the correlation coefficien
between N3.4 and DMI is provided at the top of each subfigure for reference. (j
r) shows a similar analysis but with the western pole of the DMI index (DMIw)
Figure 2.8 Scatterplot of El Niño Modoki index (EMI; x-axis) versus Dipole Mode Inde.
(DMI; y-axis) during the OND season for each of the 24 years analyzed in both
model predictions (a-h) and GPCP dataset (i). The area of the circle i
proportional to the absolute value of OND rainfall anomaly averaged over part of
Eastern Africa (blue dashed box of Fig. 2.1i), with positive (negative) anomaly
coloured in green (orange). As in Fig. 2.5 the best forecasted year is highlighted
in red, the second-best in blue, and the third-best in magenta4
Figure 2.9 Correlation between East African RFa index and climate indices for the
OND season. Asterisks (*) and (**) indicate significance at the 95% and 99%
confidence levels, respectively. The RFa index is the area-averaged over Eastern
Africa (30–50°F 5°S-10°N) for both models and FRA5

Figure 2.10 Interannual variation of short rainy season derived from ERA5, an
individual coupled models' ensemble mean field anomalies: a) N34, b) EMI, o
DMI, d) sea level pressure anomaly index over DMI region (slpDMI), a
Equatorial wind anomaly index (UEQ)4
Figure 3.1 Seasonal rainfall climatology during the long rains (Maech-May: MAM
derived from GPCP (i), ERA5 (j), and the seasonal prediction systems from C3.
which includes 8 ocean-atmosphere coupled model ensembles and cover th
period 1993–2016 (a-h). The lower panel shows area-averaged MAM rainfa
anomalies for parts of Eastern Africa (30–50°E, 5°S-10°N; blue dashed box in
for models, ERA5, and the GPCP dataset. Anomalies are computed relative to the
climatology shown in the upper panel5
Figure 3.2 Seasonal rainfall standard deviation during the long rains (MAM) derive
from the seasonal prediction systems from C3S, which includes 8 ocean
atmosphere coupled model ensembles and covers the period 1993–2016 (c-j) an
GPCP (i), ERA5 (j) datasets5
Figure 3.3 Mean bias (Model-GPCP) for C3S model predictions for lead season
(March-May: MAM), lead season 2 (April-June: AMJ), and lead season 3 (May
July: MJJ) of rainfall climatology (ensemble mean) which initialized in Februar
during 1993-20165
Figure 3.4 Pointwise-correlation maps between GPCP and C3S model predictions for
lead season 1 (May-March: MAM), lead season 2 (April-June: AMJ), and lea
season 3 (May-July: MJJ) of rainfall anomalies (ensemble mean) during 1993
2016. Stippling indicates area where the correlation between the hindcast an
observation are statistically significant at 99% confidence level, as calculated b
a two-side Student t-test for 22(N-2) degrees of freedom
Figure 3.5 Anomaly correlation coefficient (ACC) between GPCP and each C3S model
(a-h; shown in the upper panels) for monthly rainfall anomaly over part of Easter
Africa (blue dashed box of Fig. 1i) for each year (grey lines) from lead month
(February) to lead month 5 (February). In each subfigure, the top three forecast

second-best in blue, and the third best in magenta. These forecasts are determined
by sorting all predicted years based on their average ACC values across February
and March The lower panel (i) illustrates the spatial correlation between each
model and GPCP rainfall anomalies for the MAM season, calculated over
Equatorial Eastern Africa (30–50°E, 5°S-10°N)61
Figure 3.6 Scatterplot of Niño3.4 index (N34; x-axis) versus Dipole Mode Index (DMI;
y-axis) during MAM season for each of the 24 years analyzed in both model
predictions (a-h) and GPCP dataset (i). The area of the circle is proportional to
the absolute value of MAM rainfall anomaly averaged over part of Eastern Africa
(blue dashed box of Fig. 1i), with positive (negative) anomaly coloured in green
(orange). As in Fig. 3, the best forecasted year is highlighted in red, the second-
best in blue, and the third-best in magenta. Additionally, the correlation coefficient
between N3.4 and DMI is provided at the top of each subfigure for reference. (j-
r) shows a similar analysis but with the western pole of the DMI index (DMIw).
64
Figure 3.7 Scatterplot of El Niño Modoki index (EMI; x-axis) versus DMI (y-axis
during MAM season for each of the 24 years analyzed in both model predictions
(a-h) and GPCP dataset (i). The area of the circle is proportional to the absolute
value of MAM rainfall anomaly averaged over part of Eastern Africa (blue dashed
box of Fig. 2.1i), with positive (negative) anomaly coloured in green (orange). As
in Fig. 3.5, the best forecasted year is highlighted in red, the second-best in blue,
and the third-best in magenta65
Figure 3.8 Correlation between RFa and climate indices for MAM season. Asterisks
(*) and (**) indicate significance at the 95% and 99% confidence levels,
respectively66
Figure 3.9 Interannual variation of MAM seasonal mean observed, individual coupled
model's ensemble means anomalies a) N34(SST anomalies averaged over 120°W–
170°W, 5 °S -5 °N) b) DMI, c) sea level pressure anomaly index over DMI region
(slpDMI), d) Equatorial wind anomaly index (UEQ). The rainfall index is area-

stand out with distinct colours: the most accurate year is highlighted in red, the

averaged over Eastern Africa (30–50°E, 5°S-10°N) for both models and ERAS
Figure 4.1 Seasonal OND rainfall climatology for ERA5 (a), model (b-f) and seasonal
cycle of monthly rainfall (g) averaged over Equatorial East Africa region (30
50°E, 5°S-10°N) for observational dataset (dotted line) and CESM coupled model
averaged over available years (801-1000), GPCP (1979 to present), and ERA (1958-2022)
Figure 4.2 Seasonal OND rainfall anomalies over East Africa derived from CESM
experiments for the period 800–1000. The anomaly calculated over Equatoric
Eastern Africa (30–50°E, 5°S-10°N)8
Figure 4.3 Seasonal OND rainfall bias (a-e) for CESM coupled models. The mean bia
is computed as the difference between each model (CESM_CTRL an
CESM_amipFULL (801-1000), CESM_AMIP (400-2200), and the observation
dataset ERA5(1958-2022)8
Figure 4.4 Composite SST anomaly over tropics for the OND season from
observational data (ERA5) and the CESM model experiment. The anomalies ar
computed for climatological periods for ERA5 (1958-2022), and models (801
1000) when only IOD occurs (first column panels), only El Niño occurs (secon
column panels), and both IOD and ENSO occur together (the third column panels)
Figure 4.5 Composite SST anomaly over Tropics for OND season from CESM noENSO
experiment8
Figure 4.6 Composite SST anomaly for the OND season from the CESM noENSO
experiment. The DMI index computed the difference between the West and East
Indian Ocean model experiments9
Figure 4.7 Scatterplot of East African short rain index (EASRi) versus N34 (first
column indicated in blues colour) and IOD (the second column indicated in re

solid line indicates the linear regression line92
Figure 4.8 Composite rainfall anomaly over East Africa region for OND season from
observational data (ERA5) and CESM model experiment during positive phase of
ENSO/IOD. The anomalies are computed for climatological periods (ERA5 1958-
2022) and models (0801 -1000) when pure positive IOD (pIOD) occurs (first
column panels), pure El Niño occurs (second column panels), and co-occurring og
pIOD and El Niño (the third column panels). The sample size(n) is the number of
events that exceed the threshold standard deviation of SST anomaly indices. The
Stippling indicates significant composite anomalies ($p < 0.05$) relative to neutral
years94
Figure 4.9 Composite rainfall anomaly over East Africa region for OND season from
observational data (ERA5) and CESM model experiment during negative phase of
ENSO/IOD. The anomalies are computed with respect to climatological periods
(ERA5 1958-2022) and models (0801 -1000) when pure negative IOD (nIOD)
occurs (first column panels), pure La Niña (second column panels) and co-
occurring nIOD and La Niña occur together (the third column panels). The sample
size(n) which numbers of events that exceeds threshold standard deviation of SST
anomaly indices. The Stippling indicates significant composite anomalies (p $<$
0.05) relative to neutral years95
Figure 4.10 Composite rainfall anomaly over East Africa region for OND season from
CESM noIOD and noENSO experiments during positive phase (first column) and
negative phase (second column). The anomalies are computed with respect to
climatological models (0801 -1000) The sample size(n) which numbers of events
that exceeds threshold standard deviation of SST anomaly indices. The Stippling
indicates significant composite anomalies ($p < 0.05$) relative to neutral years97
Figure 4.11 Partial correlation between SST indices and rainfall anomaly from the C3S
models after excluding Niño-3.4 (upper) and DMI (bottom) during the OND
season. Stippling indicates the area where the correlation between sea surface
temperature indices and RF anomaly, which are statistically significant at 99%

colour) during the OND season for ERA5 reanalysis, CESM experiments. The

confidence level as calculated by a two-sided Student t-test for 22(N-2	!) degrees of
freedom	98

LIST OF TABLES

Table 2.1 Descriptions of coupled models' multi-seasonal prediction systems from C	
accessible at (https://cds.climate.copernicus.eu/cdsapp)	23
Table 4.1 Description of CESM model configuration applied for this study	76

LIST OF ABBREVIATIONS

AGCM Atmospheric General Circulation Model

AMIP Atmospheric Model Intercomparison Project

CESM Community Earth System Model

C3S Copernicus Climate Change Service

CESM Community Earth System Model

CMCC Euro-Mediterranean Center on Climate Change

DEM Digital Elevation Model

DJF December January February

DMI Dipole Mode Index

DWD Deutscher Wetterdienst

ECCC Environment and Climate Change Canada

ECMWF European Centre for Medium-range Weather Forecasts

ENSO El Niño-Southern Oscillation

EOF Empirical Orthogonal Function

ERA5 ECMWF Reanalysis

GPCP Global Precipitation Climatology Project

ITCZ Intertropical Convergence Zone

IOD Indian Ocean Dipole

STRM Shuttle Radar Topography Mission

NACR National Centre for Atmospheric Research

OND October-November December

OGCM Oceanic General Circulation Model

NCEP National Centers for Environmental Prediction

NEMO Nucleus for European Modelling of the Ocean model

JMA Japan Meteorological Agency

1 INTRODUCTION

1.1 East African Rainfall Regimes

East Africa's climate is highly diverse due to its equatorial location, varying altitudes, the presence of the Great Rift Valley, large lakes, and proximity to the Indian Ocean (Nicholson, 2017). The region's major lakes, such as Lake Victoria, the largest freshwater lake in Africa, also play a crucial role in shaping local weather patterns (Chamberlain et al., 2014; Williams et al., 2015). The region is characterized by tropical humid, semi-arid, and arid climates. Generally, lowland areas such as the coastal zones and rift valley depressions tend to experience warm temperatures, while higher elevations, such as the Ethiopian Highlands, receive abundant rainfall due to orographic effects (Yang et al., 2014).

The timing and intensity of precipitation across East Africa vary considerably, typically following either a unimodal or bimodal rainfall regime. The northern parts of the region, including the Ethiopian Highlands, generally exhibit a unimodal rainfall climatology, with a single rainy season extending from July to September (Dunning et al., 2016). However, notable differences in seasonality exist across sub-regions (Diro et al., 2011). Further south, in countries such as Kenya, Uganda, and Burundi, a bimodal rainfall pattern is more typical, with the "long rains" occurring from March to May and the "short rains" from October to December (Yang et al., 2015a). Some studies define the short rains more narrowly, concentrating primarily on October and November (Nicholson, 2017).

These climatic variations are illustrated in Fig. 1.1, The central map displays elevation zones alongside selected locations where mean monthly rainfall (blue bars) and 2-meter air temperature (shown by red lines) are plottedIn the northern regions, including the Ethiopian Highlands, rainfall follows a unimodal pattern, peaking between July and September. Conversely, southern areas near Lake Victoria and coastal zones experience a bimodal distribution, with peak rainfall occurring in March–May and October–December. The figure further reveals that lowland and coastal regions

maintain consistently high temperatures throughout the year, while highland areas are significantly cooler. Particularly, Kenya's central highlands record rainfall maxima exceeding 250 mm per month in April and November. Similarly, heavy precipitation occurs along Lake Victoria's eastern edge in April and in coastal areas during May. However, Lake Turkana remains consistently dry, receiving less than 100 mm/month of rainfall even during the rainy seasons. Overall, within the broader continental context, East Africa exemplifies a complex climatic landscape shaped by topographic variations and proximity to major water bodies.

Numerous studies have emphasized that the broader East African region is predominantly characterized by a bimodal rainfall pattern with two primary rainy seasons: the "long rains" from March to May and the "short rains" from October to December (Schreck & Semazzi, 2004; Palmer et al., 2022). However, the short rains tend to show greater interannual variability than long rains (Palmer et al., 2023; Behera et al., 2005; Nicholson, 2015). The seasonal fluctuation significantly impacts many sectors in the region. The agriculture sector is particularly vulnerable, as rainfed farming dominates in many East African countries, affecting agricultural productivity and water availability, especially in Kenya, Tanzania, Uganda, and Ethiopia (MacLeod, 2018).

East Africa is highly vulnerable to climate extremes, such as prolonged droughts and devastating floods (Haile et al., 2020), which have severely impacted local economies and food security over the years (Niang et al., 2014). Recent studies indicate a declining trend in rainfall during the long rains season and increased variability during the short rains (Cattani et al., 2018; Gebrechorkos et al., 2018). This pronounced variability, coupled with the rising frequency of extreme events, has made East Africa one of the most food-insecure regions globally, heavily reliant on humanitarian assistance.

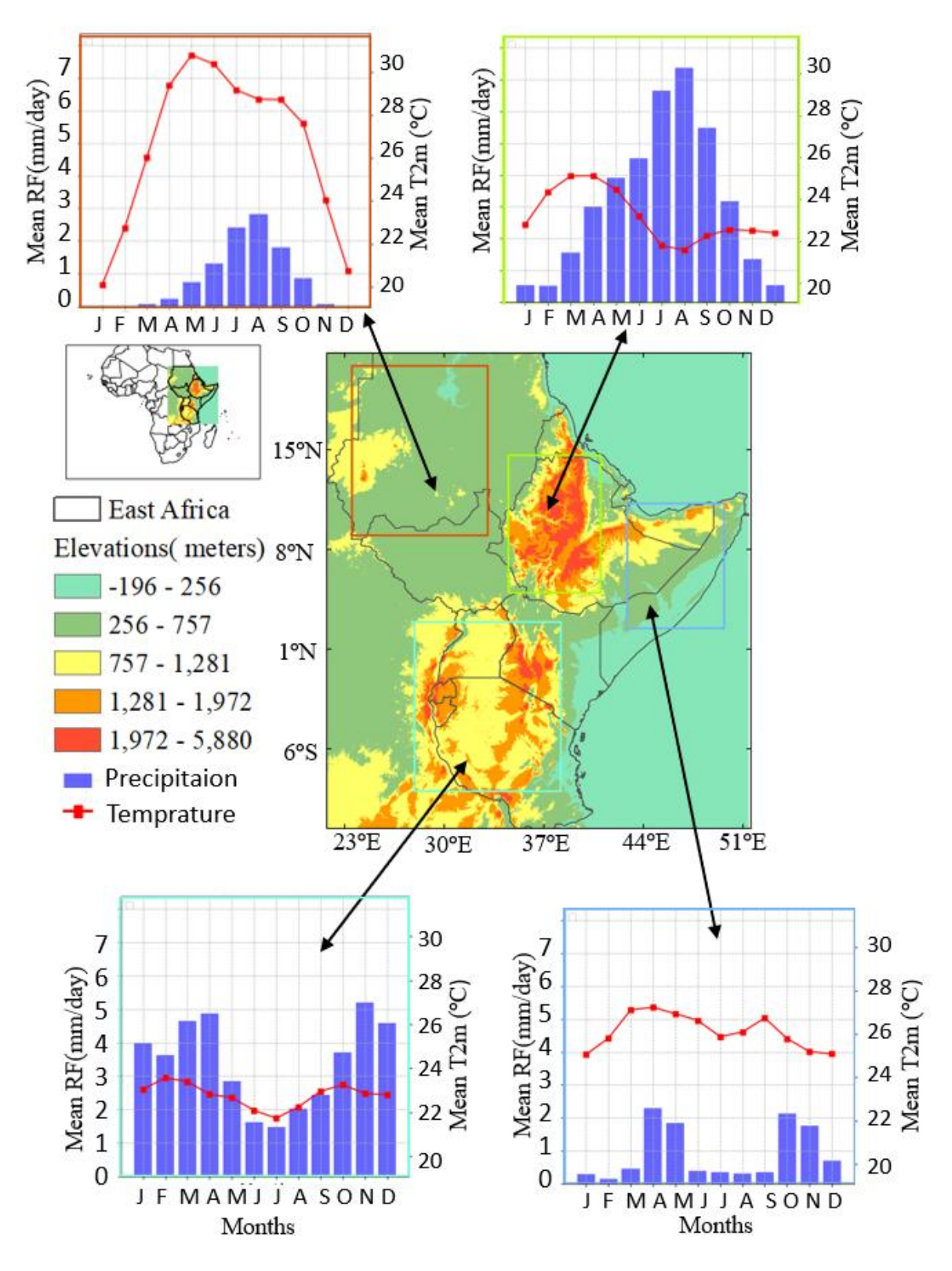


Figure 1.1 Geographic features and topography of East Africa. Elevation is extracted from the Digital Elevation Model (DEM) from STRM. The panels show the annual

cycle of rainfall and temperature over different regions of East Africa. The precipitation and temperature of two-meter (T2m) data are taken from ERA5.

1.2 Driving mechanisms of East African rainfall variability

A complex interaction of local, regional, and global climatic factors affects East African rainfall variability, resulting in significant variations in precipitation patterns over time and space. Broadly, we can classify global and local driving mechanisms that affect the distribution and intensity of EA rainfall from interannual to intraseasonal time scales. These drivers and their roles in the EA rainfall pattern are discussed in the following sections.

1.2.1 Global teleconnections

Global teleconnections are large-scale climate phenomena that link oceanic and atmospheric processes over remote have a significant impact on the variability of tropical rainfall, including over East Africa (Behera et al., 2005; Black et al., 2005; Schreck & Semazzi, 2004). These influences of regional climate systems from seasonal and interannual time scales and in turn, can regulate rainfall patterns by modifying air circulation, moisture transport, and SSTs (Lyon & DeWitt, 2012; Nicolson, 2017). This is especially true in equatorial Africa, where patterns like changes in SSTs over tropical oceans are strongly associated with these interactions. Rainfall variability is influenced by atmospheric components, including wind systems associated with teleconnections, which can either amplify or suppress precipitation patterns (Liu, 2007). Identifying sources of variability has been given major focus so far in equatorial East Africa (Hills, 1979; Schneider et al., 2014; Chobo and Huo, 2024), which is directly impacted by ENSO's modification of the Walker Circulation (Sasaki, 2015). Examining these oscillating patterns is essential for managing water resources, agriculture, and the livelihoods of millions of people in East Africa. Moisture transport into Africa is altered by the IOD and ENSO, which involves temperature differences between the eastern and western Indian Oceans.

El Niño-Southern Oscillation (ENSO)

The ENSO in the Pacific Ocean plays a critical role in East African rainfall variability (Indeje et al., 2000). It is widely regarded as the primary source of skill for seasonal-to-interannual rainfall predictions in the region. In EA, drought is strongly associated with the complexity and variability of the ENSO and land-atmosphere feedback (Zeng, 2003; Liebmann et al., 2014; Hua et al., 2016). During El Niño years, warmer SST disrupts global air circulation, leading to above-average rainfall over East Africa, particularly during the OND rainy season, which often causes flooding (Behera et al., 2005). Global atmospheric circulation patterns, e.g., ENSO, which alternates between warm (El Niño) and cool (La Niña) phases, hence influencing regional climates worldwide, including East African regions (Ashok & Yamagata, 2003). El Niño years cause the Pacific Ocean's SST to be much warmer than normal, which throws off the Walker circulation and other global air circulation patterns (Navarra et al., 2013). Particularly, during the short rainy season, this disturbance causes more convection and moisture transfer to East Africa, which results in above-normal rainfall (Palmer et al., 2023). In 2019, intense ENSO-related rainfall triggered widespread flooding that affected millions across Kenya, Tanzania, and Uganda. This extreme seasonal anomaly led to catastrophic impacts across the region (Wainwright et al., 2021).

The excessive rains underscored the region's vulnerability to ENSO-driven extremes, leading to widespread flooding and significant disruptions to local economies, infrastructure, and agricultural activities (Roy et al., 2022). In contrast, La Niña years—marked by cooler-than-average sea surface temperatures in the central and eastern Pacific—are often associated with reduced rainfall across East Africa (Hoell & Funk, 2014). Drought conditions are frequently linked to this ENSO phase, which has a major effect on the region's food security and water availability (Park et al., 2020). Particularly in the eastern and southern regions of East Africa, the possibility of drier weather is increased by La Niña's cooling effect on the Pacific Ocean (Camberlin et al., 2001; Lott et al., 2013). The periodic warming (El Niño) and cooling (La Niña) of sea surface temperatures in the central and eastern Pacific—known collectively as ENSO-have a profound impact on tropical rainfall patterns. During East Africa's short rainy season, El Niño events are often linked to above-average rainfall, largely due to

enhanced convection over the western Indian Ocean and East Africa, driven by ENSO-related shifts in atmospheric circulation (Izumo et al., 2010). However, the effects of El Niño and La Niña may be altered by the Rift Valley and local topographical features in East Africa that might alter the ENSO's large-scale climatic effects (Hamilton et al., 2020).

El Nino Modoki

El Niño Modoki is a climate phenomenon characterized by SST anomalies in the central Pacific, flanked by cooler SSTs in the eastern and western Pacific, differing from the conventional El Niño, which features peak warming in the eastern Pacific (Ashok et al., 2007). This phenomenon has distinct atmospheric and oceanic impacts, influencing global weather patterns differently from traditional El Niño events (Marathe et al., 2015). The ENSO Modoki affects African seasonal rainfall variability. During March-May, both El Niño types reduce rainfall in southern regions while increasing it in the north, but they consistently suppress northern rainfall from June to September. In October-December, canonical El Niño and positive IOD enhance East African rainfall, while El Niño Modoki reduces it. Beyond Walker circulation, this driver also impacts African rainfall by altering jet stream dynamics, particularly weakening the tropical easterly jet and shifting the African easterly jet southward, reducing rainfall in northern tropical regions like the Sahel (Preethi et al., 2015).

Canonical El Niño and El Niño Modoki generally reduce (increase) rainfall in the southern (northern) hemisphere during March-May, but both suppress northern rainfall in June-September. In boreal spring and summer, Indian Ocean drivers often counteract Pacific influences. During October-December, El Niño and positive IOD enhance rainfall in Eastern Africa, while El Niño Modoki has the opposite effect. These drivers influence African rainfall by altering the Walker circulation and jet streams, affecting the tropical easterly and African easterly jets (Preethi et al., 2015).

Depending on local conditions, these drivers affect the distribution and intensity of rainfall, with some regions impacted by the larger climatic drivers (Vellinga & Milton, 2018a). Even though ENSO has a significant impact, the interaction of these local and regional elements highlights how challenging it is to forecast rainfall patterns.

Previously, although ENSO is known as the best predictor of rainfall variability in East Africa, however, IOD has recently become a major source in predicting EA rainfall variability (Behera et al., 2005). Efforts to produce precise and trustworthy rainfall forecasts are made more difficult by its interactions with other climatic factors, such as the IOD and regional topography (Wang et al., 2019).

Indian Ocean Dipole (IOD)

Indian Ocean Dipole (IOD) key driver of natural variability over the Indian Ocean, which controls the variability of East African rainfall patterns (Black, 2005; Behera et al., 2005). To track the influence of IOD variability, define as dipole mode index (DMI; Saji et al., 1999) calculated as the difference between SST anomalies in the western Indian Ocean (50°E - 70°E, 10°S - 10°N) and the eastern Indian Ocean (90°E - 110°E, 10°S - 0°). Previous studies found that the variability in the IOD is often associated with droughts and floods in East Africa. For instance, the severe East African floods of 1961 were linked to a strong west-east SST dipole in the Indian Ocean. Recent studies have also shown that countries in the region, including Kenya, Tanzania, and Ethiopia, are particularly vulnerable to flooding and landslides during positive IOD episodes, which bring heavier-than-average rainfall (Xiao et al., 2022). Conversely, negative IOD phases, characterized by cooler western Indian Ocean near East African coast and warmer SSTs over eastern Indian Ocean near Indonesia, tend to increase the likelihood of drought conditions over the Horn of Africa (Abiy et al., 2019).

The variability of IOD has the power to either amplify or lessen the effects of ENSO on rainfall in East Africa. The western Indian Ocean warms more than the eastern Indian Ocean during a positive IOD phase, which frequently intensifies El Niño's effects by increasing rainfall in East Africa. On the other hand, East Africa often has less rainfall during a negative IOD phase, especially during the long rains (MAM season). Given that ENSO and the IOD can affect atmospheric and oceanic conditions either separately or in combination, these interactions add a great deal of complexity to the forecasting of seasonal rainfall patterns (Luo et al., 2010; Saji et al.,1999). The IOD can occur independently or coexist with ENSO events (Ashok & Yamagata, 2003). For example, in 1961 and 1967, IOD events occurred during East Africa's short rainy season

without coinciding with ENSO events. In contrast, in years like 1972, 1982, 1994, and 1997, the IOD coincided with warm-phase ENSO events (Meyers et al., 2007). The 1997 IOD event, which remains one of the most significant on record, exhibited two notable features: the IOD tends to emerge in summer, peak in October, and rapidly subside by December. The IOD's biennial pattern may reflect its interaction with the monsoon system, as well as other tropical climate models that show a similar quasibiennial oscillation, such as monsoon cycles. The argument that the ocean-atmosphere coupling observed during the 1997–1998 severe droughts in Indonesia and intense flooding in East Africa, surpassed what would typically be expected from ENSO alone (Webster et al, 1999). However, this discrepancy suggests that the IOD's influence on East African precipitation is not always consistent because other factors, such as the Madden-Julian Oscillation (MJO), may modulate rainfall patterns on intraseasonal timescales.

Madden-Julian Oscillation (MJO)

MJO is an intraseasonal tropical climate phenomenon characterized by large-scale convective disturbances that move eastward along the equator (C. Zhang, 2005). Wet and dry spells in the East African region are also shaped by the MJO from a 30 to 60-day oscillating pattern of enhanced and suppressed convection that has a major impact on intra-seasonal east rainfall patterns over East Africa (Ochieng et al, 2023). These disturbances significantly influence East African weather patterns by modulating rainfall, wind patterns, and atmospheric circulation, with implications for East Africa (Kimani et al., 2020).

The MJO is divided into two phases: an active convective phase and a suppressed phase. When the active phase of the MJO moves over the Indian Ocean, it enhances convection and moisture availability, leading to increased rainfall across parts of East Africa, particularly during the short rainy season (Fig 1.2). The suppressed phase, on the other hand, is often associated with drier conditions (Pohl & Camberlin, 2006). These dry conditions led to profound implications for agricultural productivity and water resources (Berhane & Zaitchik, 2014) in which the interaction between the MJO and local weather patterns exacerbates drought conditions or (Kimani et al., 2020)

lead to intense rainfall events affecting both food security and infrastructure (Wheeler & Hendon, 2004). In some regions of Africa, such as the Congo Basin and East Africa, the MJO signal is visible. Rainfall is often higher while the MJO convective core is over the Indian Ocean and lower when it is over the eastern Pacific during the East short and long rainy seasons (Macleod et al., 2021; Maybee et al., 2023). The typical Easterly winds become weaker during "wet" periods and stronger during "dry" ones (Pohl & Camberlin, 2006).

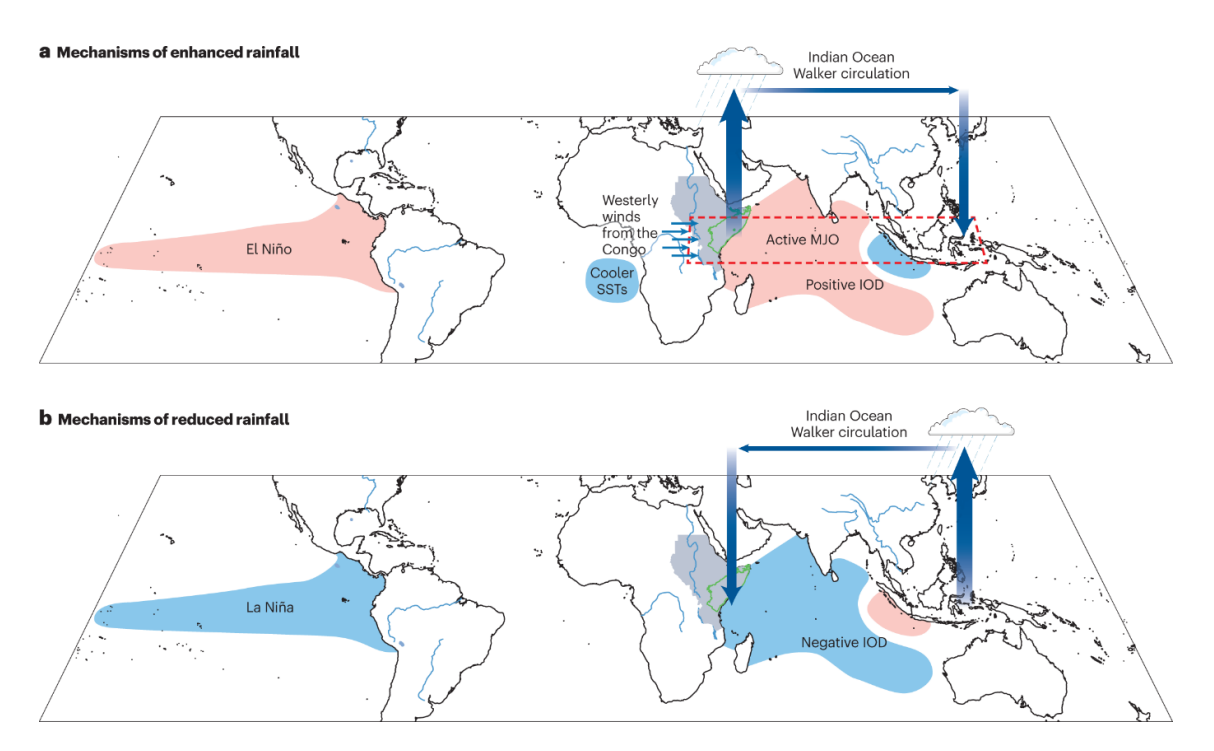


Figure 1.2 The teleconnection mechanisms that cause a) enhanced (shaded in orange color) and b) reduced (shaded in blue color) rainfall across Eastern Africa by warm and cold SST, respectively. The green contour denotes the region of Eastern - two wet seasons annually (Palmer et al., 2023).

1.2.2 Local drivers

Local drivers such as East African highlands, lakes, and the Turkana channel have a role in regional distribution, seasonality, and diurnal fluctuations of rainfall (Camberlin & Philippon, 2002). A substantial maximum of rainfall occurs over Lake Victoria because of the mesoscale circulation system it forms (Anyah & Semazzi,

2006). The complex topography of East Africa significantly influences the region's low-level atmospheric circulation, which in turn affects rainfall variability (Kinuthia & Asnani, 1982). The diverse geography, ranging from arid lowlands near the Indian Ocean coast to steep highlands, poses challenges for accurately forecasting rainfall patterns (Nicholson, 2017). The EA's topography is diverse, with a ring of mountains that includes Africa's highest peaks (>5000m above mean sea level) and a low-lying area in the east, such as the Afar Depression, located in Ethiopia's eastern edge (Fig. 1.1).

The Turkana Channel serves as a narrow opening that connects the generally low-lying (northwest) surface to the eastern coastal plain. The inner highlands are likewise divided by the channel from the north Ethiopian highlands and southeast African highlands (Kinuthia and Asnani, 1982). These orographic channelling causes of constant jet (which is known as the Turkana Jet), which has mean winds of around 10–12 m.s.1, and peaks at a geopotential height of 850 hp (Nicholson, 2015; Sun et al., 1999; Indeje et al., 2001). At the jet's entrance, there is a noticeable divergence during the day, descent takes place above its core (Sun et al., 1999), which may prevent convection and add to northern Kenya's aridity (Nicholson, 2015). However, the advection of moisture from the Indian Ocean to the Ethiopian highlands depends on the jet (Viste and Sorteberg, 2013). These highlands usually receive more consistent rainfall due to orographic lifting, where moist air is forced to rise over mountain ranges, cooling and condensing into precipitation (Viste & Sorteberg, 2013). In contrast, lowland areas such as the Eastern tip of Ethiopia, northern Kenya, and parts of Somalia are more arid, receiving far less rainfall (Haile et al., 2020). This implies, complex interaction between atmospheric circulation and topography contributes to the diversity in rainfall distribution (Hamilton et al., 2020), causing some areas to be more susceptible to seasonal droughts while others have more consistent rainfall (Onyutha et al., 2022).

The highlands form a north-south barrier from the Red Sea to southern Tanzania (Fig. 1.1). These barriers in the northern East African Rift System (EARS) still suffer from the underrepresentation of predictive models (Mologni et al, 2024). Over the Ethiopian Massif, the most extensive highland area in Africa, with almost 50% of the

continent's area above 1500 m (McCann, 1995). Large tablelands are dissected by deep valleys and dominated by several summits culminating above 4000 m. Further south lie the East African Highlands, organized as two mountain arcs following the eastern and the western Rift valleys, from about 4°N to 10°S. In the east, the Kenya Highlands, at an average elevation of 1500-2500m, are flanked to the east and south-east by Africa's two highest mountains: Mt Kenya (5199 m) and Mt Kilimanjaro (5895m). To the southern parts of the region, these mountains are prolonged by the Eastern Arc Mountains, of lower elevation. In the west, the western Rift Mountains run from western Uganda to southern Tanzania, and several peaks above 3000 m, among which are the Rwenzori Mountains (5109 m). Between the two arcs is a large tableland around 1000-1200 m, on which lies Lake Victoria. Overall, the East African Highlands have a major impact on both the regional and extra-regional climate variability over the regions (Slingo et al., 2005). In particular, the wet conditions prevailing over the Congo Basin are a result of the presence of the East African highlands (Nicholson, 2017).

1.3 Role of the Intertropical Convergence Zone (ITCZ)

The ITCZ plays a crucial role in East African rainfall. It is a band of low pressure near the equator where trade winds from both hemispheres converge, leading to uplift and precipitation. The seasonal migration of the ITCZ northward and southward dictates the timing and intensity of rainfall in East Africa. During its northern passage, the ITCZ brings the long rains, while its southern shift contributes to the short rains. However, the positioning and movement of the ITCZ are influenced by global and regional climate drivers, which add variability to rainfall patterns. The location of the ITCZ matters in the magnitude of the precipitation field in the EA region (Kebacho, 2023). However, its variability is primarily driven by large-scale atmospheric and oceanic systems that influence seasonal weather patterns (Nicholson, 2017; Palmer et al., 2023).

One of the most significant factors is the movement of the ITCZ, which is a band of clouds and rain that forms where the northeast and southeast trade winds meet near the equator (Nicholson, 2018; Zhao & Cook, 2021). The ITCZ brings a fluctuating amount of rainfall to different parts of East Africa as it migrates north and south with

the changing of the seasons (McGee et al., 2014). The bimodal rainfall pattern of long rain and short rainy season is due to the migration of the ITCZ across the region, which also controls the seasonal cycle of rainfall. For example, the ITCZ sweeps over the region during the long rainy season, resulting in extensive rainfall; during the short rains, it backs away southward and contributes to precipitation, though less intensely. As confirmed by Camberlin & Philippon (2002), short rains are influenced by the ITCZ when it migrates from the north to the southern hemisphere, while the long rains are influenced by its migration from the south to the north.

The movement ITCZ is inherently variable, leading to significant interannual fluctuations in rainfall patterns across East Africa (Lashkari & Jafari, 2021). Shifts in the ITCZ are a major contributor to anomalous rainfall events (Camberlin & Philippon, 2002), which can result in extreme outcomes such as floods and droughts (Cioffi et al., 2016; Nicholson, 2016). While local factors, including East Africa's complex topography, play a critical role in shaping regional rainfall variability, several studies (Behera et al., 2005; Indeje et al., 2000; Vellinga & Milton, 2018) have demonstrated that large-scale climate drivers, particularly ENSO and the IOD, are primary influencers of this variability.

1.4 State-of-the-art Seasonal Prediction Systems

Skillful seasonal-time-scale predictions are currently made on a real-time basis for several tropical regions around the world, including equatorial east Africa (Gualdi et al., 2020; Hitoshi et al., 2022; Saha et al., 2014). For example, C3S seasonal prediction models are a suite of numerical models used for generating global and regional rainfall seasonal forecasts. The models used for such predictions are based on empirical associations between elements of the general circulation of the atmosphere and ocean derived from historical data (Johanson et al., 2019). Such associations are used to define predictors of regional circulation or rainfall. Recently, huge efforts on improvements of dynamical seasonal prediction systems have become essential to predict climatic variability ahead of time (Gualdi et al., 2020; Stevens et al., 2013). These forecasting systems provide vital information for many sectors in the world, especially for climate-affected countries like EA. A couple models that integrate

interactions between the atmosphere, oceans, land, and ice are essential to replicate physical processes in the Earth's climate system(Merryfield et al., 2013). This strategy differs from statistical methods, which depend on correlations found in hindcast data. Dynamical prediction systems aim to provide more accurate and reliable forecasts of phenomena such as monsoon variability, drought likelihoods, and temperature anomalies by integrating real-time observations with physical laws and numerical models (Christensen & Berner, 2019).

The main components of dynamical seasonal prediction systems are coupled systems, including atmospheric models, ocean models, and (Stockdale, 1997). Atmospheric models simulate large-scale circulation patterns and thermodynamic processes, which are essential for identifying weather variability over different timescales (Sillmann et al., 2017). Ocean models focus on capturing SST and ocean dynamics, which are critical for phenomena such as the ENSO (Luo et al., 2007). Coupled systems integrate the atmosphere and ocean to account for complex feedback mechanisms, significantly improving the skill of seasonal forecasts (Webster et al., 1999). These models depend on data assimilation techniques, which combine observational data from satellites, buoys, and ground stations with model simulations to ensure accurate initialization. Data assimilation bridges the gap between real-world observations and theoretical models, enhancing the overall reliability of forecasts (Merryfield et al., 2020).

Recent advances in dynamical seasonal prediction systems have significantly improved forecast accuracy and applicability. For example, ECMWF's SEAS5 has demonstrated skill in predicting temperature and precipitation anomalies using high-resolution coupled models and advanced data assimilation (Johnson et al., 2018). It successfully predicted the 2015–2016 El Niño, highlighting its ability to anticipate extreme climate events. Despite recent advancements, several challenges hinder the full potential of dynamical seasonal prediction systems, and model biases remain a significant issue, which should account for accurate precipitation forecasts (Manzanas, 2020). The bias may arise due to resolution constraints due to computational limitations that hinder the ability of models to capture localized phenomena. Moreover, uncertainties in coupled interactions, especially in regions with sparse observational

data, add complexity to long-term projections (Parker, 2010). Addressing these challenges requires innovative approaches, such as integrating machine learning algorithms for improved parameterization and leveraging hybrid systems that combine statistical and dynamical methodologies. Additionally, expanding observational networks and increasing computational resources will play a crucial role in advancing these systems.

Coupled forecasting systems that integrate sea ice, land, and ocean components are increasingly adept at simulating a broad range of physical processes within the Earth system, across timescales from days to seasons. However, a persistent challenge in seasonal prediction lies in the inadequate representation of model physics, particularly cloud processes, which can compromise forecast accuracy (Morcrette et al., 2018). These limitations often result in model drifts, where simulations gradually diverge from observed values, and in persistent biases, defined as systematic deviations between model outputs and real-world data (Vitart and Balmaseda, 2017). Advancing seasonal prediction, therefore, hinges on improving cloud parameterizations and related physical processes (Merryfield et al., 2020; Sillmann et al., 2017).

Another major hurdle is the accurate initialization of the ocean and sea ice components. Current seasonal prediction systems still exhibit considerable spread in initialized sea ice fields, which undermines forecast reliability (Chevallier et al., 2017; Zampieri et al., 2018). Despite these challenges, effective forecasting on sub-seasonal to decadal timescales remains a critical tool for decision-makers, as weather and climate variability can have profound social, economic, and environmental consequences. As a result, there is growing interest across scientific, operational, and applied sectors in developing more skilful forecasts to improve our understanding and management of extreme events.

The several sources of predictability in the Earth's climate system (Fig. 1.4) are based on the periods in which they have an impact, ranging from days to centuries (Merryfield et al., 2020). Short-term predictability (days to weeks) is dominated by key phenomena like weather, the MJO, and the North Atlantic Oscillation (NAO). Soil moisture, the stratosphere, and phenomena like the quasi-biennial oscillation (QBO)

and IOD all affect subseasonal and seasonal forecasts. Oceanic patterns such as the Pacific Decadal Variability (PDV) and Atlantic Multidecadal Variability (AMV) and sources such as the ENSO offer predictability on longer periods. From weather forecasts to climate projections, natural and human-induced forcing become important drivers across decades to centuries.

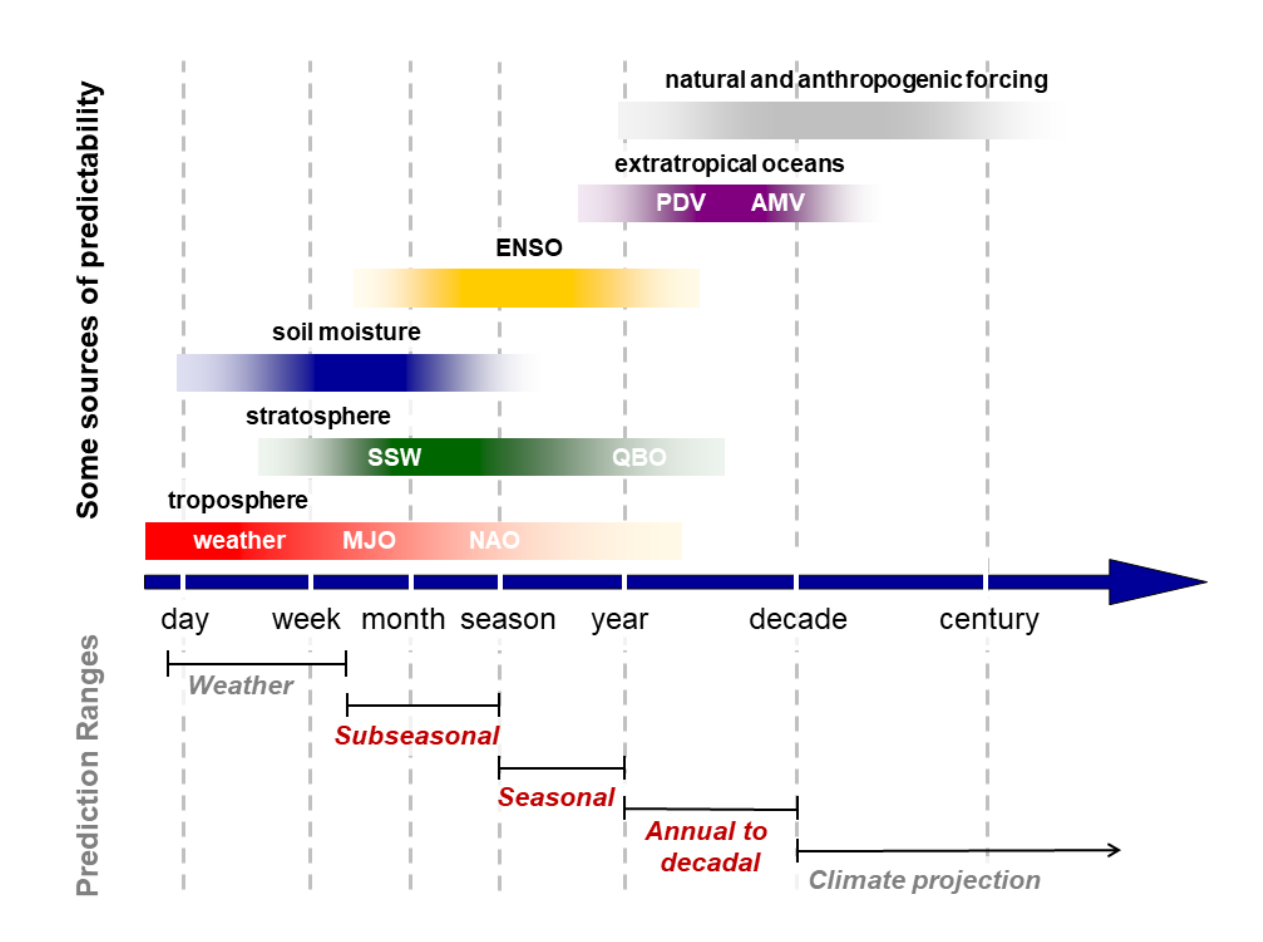


Figure 1.3 A schematic representation of the sources of predictability and temporal ranges for climate and weather forecasting (adopted from Merryfield et al., 2020)

1.5 Dissertation structure

This PhD thesis is divided into six chapters. Chapter 1 provides a general introduction to East African rainfall regimes and their driving mechanisms.

Chapter 2: Explores the seasonal predictability of the East African short rains (EASR) using state-of-the-art seasonal prediction models. Our findings indicate that while most models exhibit significant mean rainfall biases in certain regions, they demonstrate notable skill in capturing rainfall patterns during the short rainy season across much of East Africa. However, their performance is less consistent over the northern and western parts of the study region. In particular, the models struggle to accurately represent rainfall patterns along the East African highlands, especially in the Ethiopian and Kenyan highlands. This suggests that the influence of topographical features in these regions may not be well-represented in the models.

Chapter 3: Assess the predictability of the East African long rains using dynamical models, employing similar methodologies to those in Chapter 2 but with different initial conditions. Additionally, we compare model outputs to the GPCP dataset to examine systematic errors at each lead time. We identify periods when the models consistently outperform persistence forecasts and determine years with higher predictability at monthly lead times. The results indicate that the models more accurately reproduce long rains (i.e., MAM rainfall anomalies) during ENSO years than during IOD periods. This suggests that large-scale interactions between atmospheric and oceanic conditions, particularly those driven by ENSO, have a stronger influence on the long rainy season in East Africa.

Chapter 4 Investigate the independent roles of ENSO and IOD variability in influencing East African short rain variability using Community Earth System Model (CESM) experiments. The study examines four CESM experiments: CESM-CTRL (control simulation), CESM-noENSO (suppressed ENSO variability), CESM-noIOD (suppressed IOD variability), and CESM-amipFULL (atmosphere-only simulation with SST prescribed from CESM-CTRL).

1.6 Objectives

This study aims to assess the seasonal predictability of East African rainfall by analyzing model ensembles and investigating the influence of large-scale climate phenomena, with a particular focus on the region's two main rainy seasons. The key research questions addressed include: To what extent do dynamical seasonal prediction systems capture the spatial and temporal characteristics of East Africa's major rainy seasons? Which climate drivers exert the greatest influence on the variability of the short (March–May) and long (October–December) rainy seasons? When and why does forecast skill vary—i.e., under what conditions is predictability enhanced or diminished? Additionally, the study evaluates how model performance depends on the phases of ENSO and the IOD, considering both their independent and combined effects on East African rainfall patterns. Specifically, the study addresses the following objectives:

- Assess the predictability of East African short rains (OND season) using C3S prediction models initialized in September.
- Assess the predictability of the East African long rains (MAM season) using
 C3S prediction models initialized in February.
- 3. Evaluate Model Biases: Identify and quantify mean rainfall biases in dynamical climate prediction models to understand systematic errors in seasonal forecasts.
- 4. Investigate the roles of ENSO and IOD on East African short rains using Earth system model experiments, exploring how suppressing these drivers alters regional rainfall patterns.

2 FORECASTING EAST AFRICAN SHORT RAINS

2.1 Introduction

The East African region is exposed to climate variability such as recurrent drought and floods, which leads to food insecurity. In recent years, intense droughts occurred in 1996, 1998, 2005, 2016, 2020, and 2021 (Doi et al., 2022). For example, (Amha et al., 2023) confirmed the extended meteorological drought from 2020 to 2021 caused much crop failure and livestock production in eastern Ethiopia, Kenya, and Somalia. Since the region highly relies on rain-fed agriculture, the delayed onset or early cessation of the rainy seasons has a direct impact on crop patterns (MacLeod, 2019). This region experiences two rather distinct wet seasons, each linked to the seasonal north-south movement of low-pressure systems (Camberlin & Philippon, 2002; Kebacho & Chen, 2022a; Palmer et al., 2023b). The first wet season, known as the long rains, typically occurs during the boreal spring months of March to May (MAM), characterized by heavier and more prolonged rainfall. However, recent studies indicate that some countries, including Kenya and Uganda, have experienced rainfall in January and February, extending the wet season into these months (Kebacho, 2024). The second wet season, or the short rains, generally takes place during the autumn months of October to December (OND), featuring shorter and less intense rainfall episodes (Nicholson, 2017; Palmer et al., 2023; Gamoyo et al., 2015). Compared to the long rainy season, the short rains exhibit greater interannual variability, which has significant socioeconomic implications for the region (Behera et al., 2005).

Previous studies (Bahaga et al., 2016; Oelfke et al., 2003) assessed the predictability of the interannual variability of East African rains using both statistical and dynamical model outputs, as well as global observational datasets. For instance, Walker et al. (2019) evaluated the predictability of East African short rains using operational seasonal forecasts of Greater Horn of Africa Climate Outlook Forum (GHACOF) model, which produced seasonal forecasts through a combination of dynamical and statistical climate models, expert judgment, and consensus-building, integrating global model outputs with regional climate knowledge and historical data. Their analysis revealed significant limitations, including low predictive skill and

systematic errors, such as a pronounced dry bias in December over the southern parts of East Africa. In contrast, Ogutu et al. (2017) identified a wet bias during the short rainy season across many parts of the region while evaluating ensemble climate forecasts from the European Centre for Medium-Range Weather Forecasts system-4 (ECMWF-4). Their analysis, employing metrics like the anomaly correlation coefficient (ACC), demonstrated that ECMWF-4 captured El Niño-Southern Oscillation (ENSO)-related anomalous years with region-dependent skill. Additionally, Bahaga et al. (2016) explored the predictability of September-October-November (SON) rainfall anomaly using the Asia-Pacific Climate Center Ocean-Atmosphere coupled multi-model ensemble hindcasts initialized on August 1. They reported that 5 out of 10 coupled models showed statistically significant skill in predicting short rains over the East African equatorial region. However, skill was limited over most land areas, with better performance along sections of the western Indian Ocean coastline. Their findings also revealed a strong correlation between observed and predicted rainfall anomalies during SON, driven by the phase of a dominant regional climate mode, the Indian Ocean Dipole (IOD; Saji et al., 1999). Prediction of short rainy season over East Africa at least one season ahead has been successfully predicted using the dynamical coupled model, as in previous studies (Begera et al, 2005).

ENSO and IOD modes have a strong influence on the interannual variability of east African short rains (Endris et al., 2019; Indeje et al., 2000), with their independent roles, as drivers of East African short rains, that have been studied using Scale Interaction Experiment-Frontier Research Center for Global Change, version 1 (SINTEX-F1) model (Behera et al., 2005). The latter study found that the SON rainfall anomaly (RFa) exhibited significant correlation with the pure IOD (i.e., an IOD event occurring during neutral ENSO phases), while the correlation with ENSO was found to be not statistically significant. When positive IOD coincided with strong El Nino in years like 1972 and 1997, East African short rains experienced excess precipitation (Saji et al., 1999). Yet, some studies (Macleod & Caminade, 2019) suggest that positive ENSO phases, like the 2015 El Niño event, may occasionally exhibit a stronger association with East African short rains than the positive phase of the IOD. Consequently, a comprehensive assessment of East African rainfall predictability

should account for the combined effects of ENSO and IOD on rainfall variability (Cherchi & Navarra, 2013) as has been done for other regions (e.g., Liguori et al., 2022).

In addition to ENSO and IOD, factors such as Madden-Julian Oscillation (MJO) influence the fluctuations in East African brief rains. By regulating convection across the Indian Ocean and East Africa, the MJO, a prominent form of intraseasonal variability, has a major impact on rainfall patterns (e.g., Roundy & Kravitz, 2009; Liebmann et al., 1994). Moisture transfer from the Indian Ocean into East Africa is also significantly influenced by the position and intensity of the subtropical anticyclones, especially the Mascarene High (Behera et al., 2005; Williams et al., 2012). Moreover, depending on its strength and direction, the Somali Jet, a crucial part of the low-level atmospheric circulation, either promotes or inhibits moisture advection (Findlater, 1971; Nicholson, 2017). The timing and intensity of the short rains are also influenced by the seasonal fluctuations in the ITCZ (Waliser & Gautier, 1993; Nicholson, 2018). Furthermore, by influencing surface heat fluxes and atmospheric stability, land-atmosphere feedback such soil moisture and vegetation dynamics can locally increase or decrease rainfall (Taylor et al., 2012; Anyah et al., 2006).

To date, no study has assessed the predictability of East African short rains using the multi-system seasonal retrospective forecasts provided by the Copernicus Climate Change Service (C3S), which employs state-of-the-art seasonal prediction systems. This study aims to fill this gap by not only evaluating the predictive skill of these systems but also examining the models' skill dependency on ENSO and IOD phases, considering both their independent and combined effects on the East African short rain patterns.

2.2 Datasets, models, and methods

2.2.1 Observational data set

Forecast verification requires good observational data (Maraun *et al.*, 2010) and robust verification methodologies. Over East Africa, a sparse climatological station network limits the use of pure in situ observations to verify gridded forecast products.

We therefore utilize observed rainfall data from the Global Precipitation Climatology Project (GPCP) version 3.2 and the European Centre for Medium-Range Weather Forecasts (ECMWF) fifth-generation reanalysis (ERA5). GPCP version 3.2 provides estimates with a resolution of $0.5^{\circ} \times 0.5^{\circ}$ from 1979 to the present (Adler et al., 2003; Huffman et al., 2023). The dataset contains monthly analyses of global precipitation, merging observations from rain gauges with precipitation estimates from low-orbit satellite microwave data, geosynchronous-orbit satellite infrared data, and sounderbased estimates. The ERA5 dataset provides global climate reanalysis data with a spatial resolution of $0.25^{\circ} \times 0.25^{\circ}$. It integrates observational data from various sources, including surface stations, upper-air observations, and satellite data, using data assimilation. ERA5 offers data for multiple variables, including precipitation and sea surface temperature, spanning from 1979 to the present (Hersbach et al., 2020). Each dataset offers distinct advantages: GPCP assimilates precipitation data from multiple sources, and ERA5 provides a higher-resolution precipitation field that is physically consistent with the SST field used in this study.

2.2.2 C3s model descriptions

To assess the predictability of the East African short rain, i conducted an evaluation of eight coupled ocean-atmosphere model seasonal prediction systems available from Copernicus Climate Change Service (C3S) offers a comprehensive multi-system seasonal forecast service, presenting data from various state-of-the-art seasonal prediction systems. These systems offer insights into future climate patterns up to six months in advance. The service includes aggregated forecasts from multiple systems, as well as detailed information from individual participating centers, such as ECMWF, Met Office, Météo-France, Deutscher Wetterdienst (DWD), Euro-Mediterranean Centre on Climate Change (CMCC), National Centers for Environmental Prediction (NCEP), Japan Meteorological Agency (JMA), and Environment and Climate Change Canada (ECCC).

The JMA model, developed by the Japan Meteorological Agency, uses the JMA-GSM atmospheric general circulation model with a resolution of TL319 (\sim 55 km) and 100 vertical levels. Its ocean component is MRI.COM v4.6, configured with a 0.25°

tripolar grid and 60 vertical levels, and the ensemble size is 10 (Hitoshi et al., 2020). The ECMWF model employs the IFS 43r1 AGCM at TCO319g resolution with 91 levels and the NEMO v3.4 OGCM, which runs on a 0.25° ORCA grid with 75 vertical levels, using an ensemble size of 25 (Johnson et al., 2019). Similarly, the ECCC model from Environment and Climate Change Canada integrates the CanAM4 AGCM at T63 (~2.8° lat-lon) with 35 levels and the CanOM4 OGCM at ~1.4° longitude by 0.94° latitude resolution with 40 levels, using 10 ensemble members (Merryfield et al., 2013). The UKMO model (UK Met Office) employs the GC3.2 AGCM at N216 (~0.83° longitude, 0.56° latitude) with 85 vertical levels, coupled with the NEMO v3.6 OGCM on a 0.25° ORCA grid with 75 levels, and has an ensemble size of 28 (Williams & Funk, 2011).

The CMCC model, developed by the Centro Euro-Mediterraneo sui Cambiamenti Climatici, uses the CESM 1.2 AGCM (~0.5° latitude/longitude resolution with 46 levels) and the NEMO 3.4 OGCM at 0.25° resolution with 50 levels, employing 40 ensemble members (Gualdi et al., 2020). The current version is CMCC-SPS3.5, i.e., Euro Mediterranean Center for Climate Change - Seasonal Prediction System, Version 3.5. The System is based on a coupled Ocean-Atmosphere Global Climate Model operated monthly in Ensemble seasonal mode (6-month predictions) and comprises monthly ensemble hindcasts covering the period 1993-2016. It includes 46 vertical levels at a spatial resolution of roughly 0.5° latitude/longitude. The NEMO 3.4 ocean general circulation model (OGCM), which has 50 vertical levels and a better spatial resolution of 0.25°, is also incorporated into the CMCC model to provide precise representations of oceanic processes including heat flux and currents.

The MeteoF model, from Météo-France, incorporates the global numerical weather prediction model ARPEGE (Action de Recherche Petite Echelle Grande Echelle) is an essential tool for operational weather forecasting at Météo France. v6.4 AGCM with TL35 (~0.5° resolution) and 137 levels, coupled with the NEMO v3.6 OGCM on a 0.25° ORCA grid with 75 levels, using an ensemble size of 25(Baté et al., 2021). The DWD model, from the Deutscher Wetterdienst, features the ECHAM 6.3.05 AGCM at T127 (~100 km) resolution with 95 levels and the MPIOM 1.6.3 OGCM configured at TP04 with 40 levels, running with 30 ensemble members (Stevens et al.,

2013). The NCEP model, developed by the National Centres for Environmental Prediction, uses the GFS AGCM at T128 (~1° resolution) with 64 vertical levels and the GFDL MOM4 OGCM, which operates on a 0.25° equatorial grid to 0.5° resolution with 40 levels, featuring an ensemble size of 24(Saha et al., 2014). Table 2.1 provides a detailed summary of all models, highlighting differences in resolution and ensemble sizes. Climate variables, including precipitation and SST, were retrieved for a common hindcast period spanning from 1993 to 2016, at a monthly time scale.

Table 2.1 Descriptions of coupled models' multi-seasonal prediction systems from C3S accessible at (https://cds.climate.copernicus.eu/cdsapp).

Organizatio	AGCM	Atm. resolution	OGCM	Ocean resolution	Ensembl	Reference
n name	AGUM	Aun. resolution	UGCM	ocean resolution	e size	Reference
JMA	JMA- GSM	TL319 (~55km)/100 levels	MRI.CO M v4.6	0.25º tripolar grid/ 60 levels	10	(Hitoshi et al., 2020)
ECWMF	IFS 43r1	TCO319g/ 91 levels	NEMO v3.4	0.25° ORCA / 75 levels	25	(Johnson et al., 2019)
ECCC	CanAM4	T63 (~2.8° latlon) / 35 levels	CanOM4	~ (1.4°lon, 0.94°lat)/ 40 levels	10	(Merryfield et al., 2013)
UKMO	GC3.2	N216 (~0.83°lon, 0.56°lat) / 85 levels	NEMO v3.6	0.25° ORCA/75 levels	28	(Williams et al., 2018)
СМСС	CESM 1.2	~0.5°lat-lon/46 levels	NEMO 3.4	0.25°/50 levels	40	(Gualdi et al., 2020)
MeteoF	ARPEGE v6.4	TL35 (~0.5°) / 137 levels	NEMO v3.6	0.25° ORCA / 75 levels	25	(Baté et al., 2021)
DWD	ECHAM 6.3.05	T127(~100 km)/ 95 levels	MPIOM 1.6.3	TP04/40 levels	30	(Stevens et al., 2013)
NCEP	GFS	T128 (~ 1°) / 64 levels	GFDL MOM4	0.25° (equator) to 0.5° /40 levels	24	(Saha et al., 2014)

2.2.3 Skill evaluation method

The anomaly correlation coefficient (ACC) analysis is a widely used statistical measure in climate prediction and forecasting to evaluate the skill of models in

reproducing observed anomalies (Wilks, 2011). It quantifies the degree of spatial or temporal agreement between simulated and observed anomalies, concerning their respective climatological means. Anomalies are deviations from a model's ensemble or observation's climatological average, which help isolate signals of variability from the background climate state. The ACC measures how well the simulated anomalies match the observed anomalies in both pattern and magnitude. A positive ACC indicates that the model has skill in predicting the observed anomalies, where a value of 1 implies perfect agreement, 0 suggests no correlation, and a negative value indicates anticorrelation, meaning the model's predictions deviate systematically in the opposite direction. In seasonal and interannual prediction studies, the ACC is often applied to assess model performance across different lead times, regions, or seasons. For example, it can be used to compare predicted precipitation or sea surface temperature anomalies against observations over a specific region, such as East Africa, during key rainy seasons. The robustness of ACC results often depends on the verification dataset used (e.g., reanalysis data like ERA5) and the presence of large-scale climate drivers like ENSO and the IOD, which influence the anomaly patterns. Mathematically, it can be expressed by the following equation (1):

$$ACC_{(Fc,Ob)} = \frac{\sum_{i=1}^{n} \left((Fc_i - \overline{Fc}) \left(Ob_i - \overline{Ob} \right) \right)}{\sqrt{\sum_{i=1}^{n} (Fc_i - \overline{Fc})^2} \sqrt{\sum_{i=1}^{n} \left(Ob_i - \overline{Ob} \right)^2}}$$
(1)

Where, in the case of temporal ACC, Ob_i is observational data for each year, Fc_i is an ensemble mean of forecast anomaly at initialized time for each year, and n is the number of years. \overline{Fc} and \overline{Ob} are the time means of models' ensembles and observations, respectively. At 90% or 95% confidence levels, p-values obtained from the two-tailed Student's t-distribution are used to assess the statistical significance of the correlation coefficient (r).

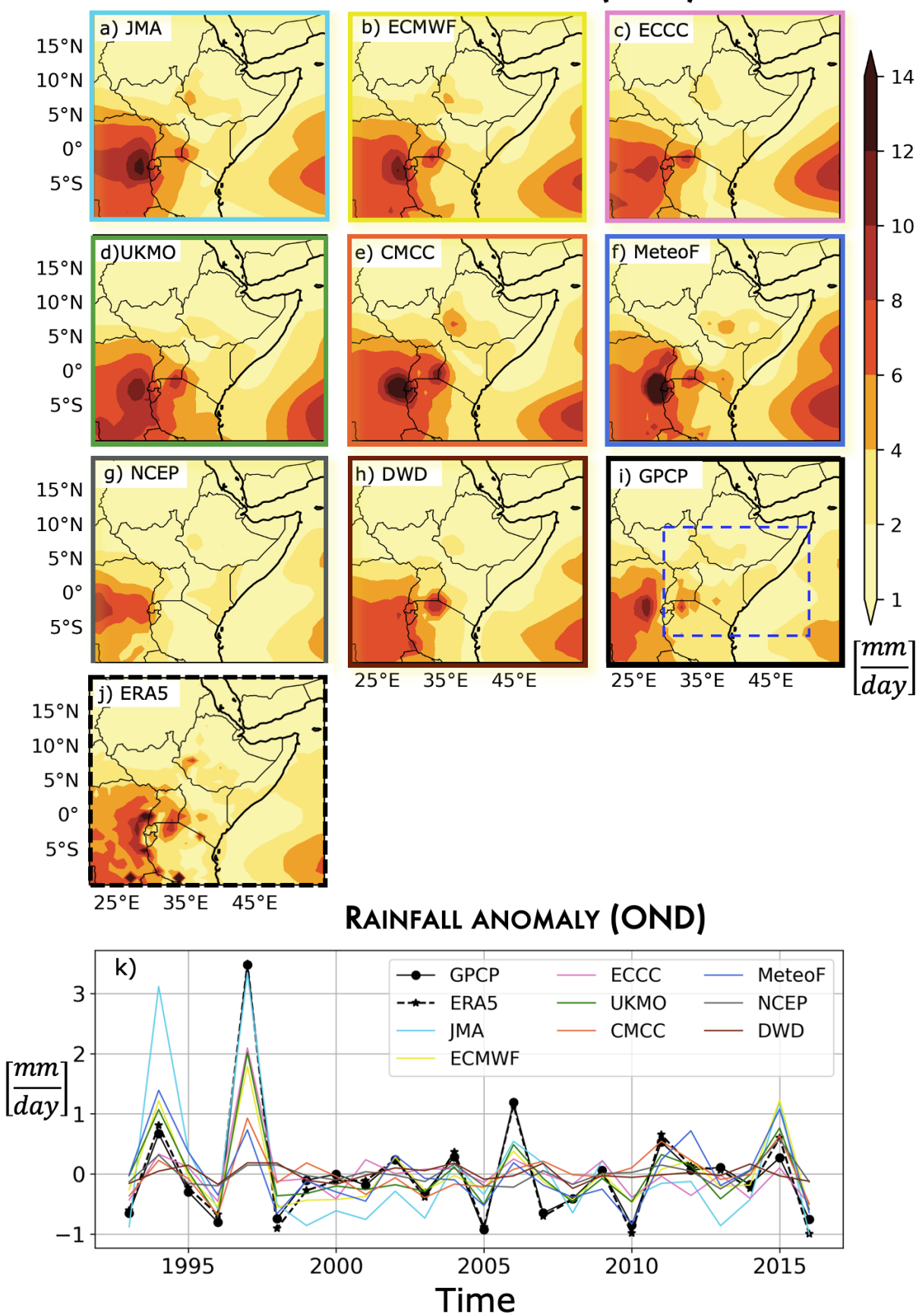
2.3 Model climatology and inter-annual variability

To characterize the mean bias in forecasting precipitation during the East African short rain season, we compare the rainfall climatology of each model (i.e., ensemble mean) with GPCP and ERA5 observational products (Fig. 2.1). Observational

datasets and models present high precipitation over the southwest parts of the analyzed region. Specifically, the maximum rainfall pattern is observed over the Congo Basin with secondary peaks over Lake Victoria and southern Ethiopia, all located inland and away from the coast. These high rainfall areas appear to be closely linked with orographic features, such as the Mitumba Mountains stretch along the Western Rift Valley in Eastern Congo and the East African highlands (e.g., Ethiopian and Kenyan highlands). However, both GPCP and ERA5 have little precipitation over the Indian Ocean with a relative maximum located between the Equator and 5°S. While models represent this feature, all but NCEP overestimate the rainfall pattern. Overall, the climatology depicted by observations and all models except NCEP presents main features associated with orographic precipitation. However, a small-scale local precipitation maximum in the westernmost part of Ethiopia (i.e., the Ethiopian highlands, approximately around 7°N–38°E) is captured by only 50% of the models (i.e., JMA, ECMWF, CMCC, and MeteoF). While this feature is absent in the GPCP dataset (Fig. 1i), it appears to be realistic as it is also evident in ERA5 (Fig. 2.1j), which provides precipitation estimates at a higher spatial resolution (0.25° for ERA5 vs. 0.5° for GPCP). As expected, compared to observational datasets, the models' climatology generally exhibits smoother precipitation patterns.

We also examined the year-to-year variation of short rainy season (Fig. 2.1k) by averaging RFa over part of East Africa between 5°S-10°N and 30°-50°E (blue box in Fig. 2.1i). Subsequently, we derived an equatorial East African rainfall index (EEARi), following a methodology like that of Palmer et al. (2023). The index reveals that 1997 appears to represent the peak rainfall for both models and observations. However, it also indicates that some models, such as DWD and NCEP, significantly underestimate this event. Generally, GPCP and ERA5 present more year-to-year variations than the models, as the ensemble means smoothing out most of the internal variability that grows from the perturbation in the initial conditions. Both models and observations generally exhibit consistency during the years with relatively strong positive rainfall anomalies. This consistency also holds for a few negative events presented in 1996 and 2010.

RAINFALL CLIMATOLOGY (OND)



26

Figure 2.1 Rainfall climatology during the short rains (OND) derived from GPCP (i), ERA5 (j), shown upper panels, and the seasonal prediction systems from Copernicus Climate Change Service (C3S), which includes 8 ocean-atmosphere coupled model ensembles and cover the period 1993–2016 (a-h). The lower panel shows area-averaged OND rainfall anomalies for part of Eastern Africa (30–50°E, 5°S-10°N; blue dashed box in i) for models, ERA5, and the GPCP dataset. Anomalies are computed relative to the climatology shown in the upper panel.

In addition to the evolution of the EEARi, we looked at the spatial pattern of rainfall variability during the OND season as represented by the inter-annual standard deviation for both models and the observational dataset (Fig. 2.2). Over the ocean, GPCP and ERA5 present a double maximum variability at both sides of the equator at +- 5°, while in the model this is true only for ECCC MeteoF and NCEP. Furthermore, several models, but especially JMA and UKMO, present a significant bias in OND variability over the Eastern Indian Ocean. This high rainfall variability is also shown over the East African highlands and near to Congo basin. Consistent with the GPCP and ERA5 climatology, some models, including JMA, CMCC, and NCEP, demonstrate high rainfall variability over the highlands (Fig. 2 .2a, e, and g), while all models show minimal variability over northern parts of East Africa.

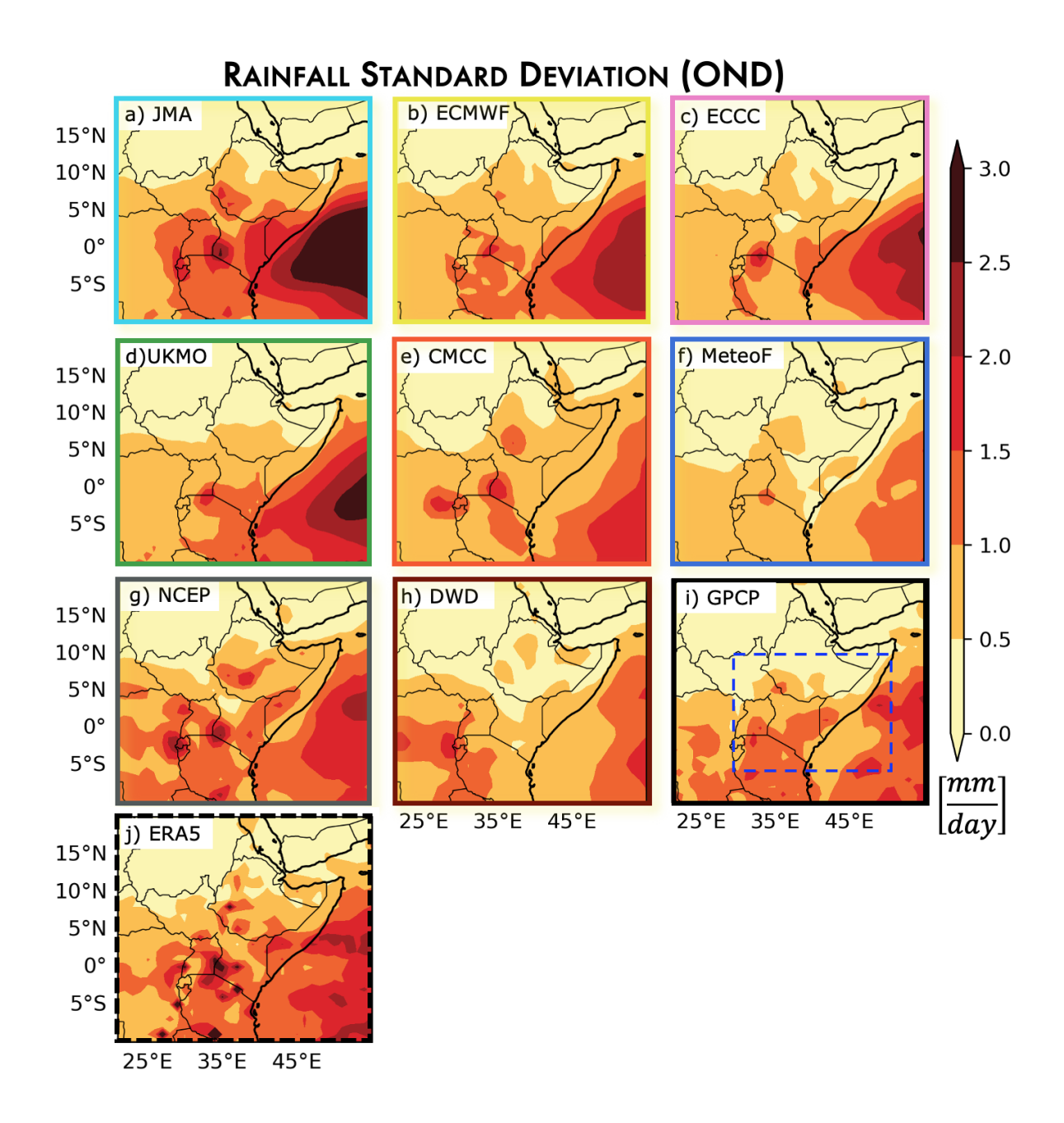


Figure 2.2 Rainfall standard deviation during the short rains (OND) derived from the seasonal prediction systems from C3S, which includes 8 ocean-atmosphere coupled model ensembles and covers the period 1993–2016 (c-j) and GPCP (i), ERA5 (j) datasets.

In dynamic climate models, rainfall bias may arise from the model's lower resolution, initial conditions, boundary conditions, or physical process representation, parameterizations of convective processes, are some examples of common biases that can lead to overestimation or underestimation of rainfall in specific regions, particularly

in tropical and subtropical zones. The model biases (Fig. 2.3) are computed as the difference between the GPCP dataset and the ensemble mean of the individual models at lead season 1 (OND), 2 (AMJ), and 3 (MJJ) when the hindcast is initialized in September. Models like JMA, ECCC, CMCC, and MeteoF show notable positive biases over the western part of the region. Particularly, models such as CMCC and MeteoF exhibit a significant overestimation of precipitation over the Ethiopian humid highlands, with the first two lead seasons showing up to 6 mm/day. It is noteworthy that the MeteoF model shows the tendency for these positive biases to increase with lead time, indicating the challenges of sustaining reliability over long forecasting lead seasons. Relatively, UKMO and ECMWF have smaller biases throughout the region up to the late winter season. These findings highlight the necessity of better model calibration, especially to capture rainfall variability in important areas such as the major highlands.

SEAOSONAL MODEL BIAS OND NDJ DJF N 10°N 10°N 5°N 0° 5°S ECM 10°N 5°N 0° 5°S 15°N 10°N 5°N 0° 5°S 2 O 15°N 10°N 5°N 0° 5°S 0 15°N CMCC 10°N 5°N 0° 5°S -2 15°N 10°N MeteoF 5°N 0° 5°S 15°N 10°N 5°N 0° 5°S NCEP mm15°N 10°N 5°N 0° 5°S 25°E 35°E 45°E 25°E 35°E 45°E

Figure 2.3 Seasonal mean bias computed as the difference between GPCP and C3S model predictions for lead season 1 (OND), lead season 2 (NDJ), and lead season 3 (DJF) of rainfall climatology (ensemble mean), which was initialized in September during 1993-2016.

2.4 Predictive skill of coupled models

The predictive skills of coupled models for East African short rains are assessed using spatial (i.e., timeseries of pattern correlation) and temporal (i.e., pointwise-correlation map) anomaly correlation coefficient (ACC; Nicolì et al., 2023). The ACC analysis is a common statistical metric used to measure the spatial (or temporal) correlation between the simulated and the observed anomaly, each computed relative to their respective climatology (see methods as shown in Eq. 1).

We perform the correlation analysis between the ensemble means of each model and the observed East African rainfall anomalies during lead seasons 1 (OND), 2 (NDJ), and 3 (DJF). The forecasts are initialized in September for each year from 1993 to 2016 (Fig. 2.4). At lead season 1, nearly all coupled models exhibit a significant correlation exceeding 0.6 across the western tropical Indian Ocean and the central to eastern African coastal regions. Moreover, along the East African coasts, models such as JMA, ECMWF, ECCC, UKMO, and CMCC (shown in Fig.2.4a-e) demonstrate robust predictive capabilities extending up to lead season 3. These skillful forecasts up to lead season 3 can be attributed in part to the persistence of SST over the Indian Ocean, which present autocorrelation values as high as 0.9 in both lead seasons 1 and 2 (Fig. 2.6). However, the DWD and NCEP models exhibited poor predictive skill, presenting correlations below 0.2 across several parts of the region in East Africa.

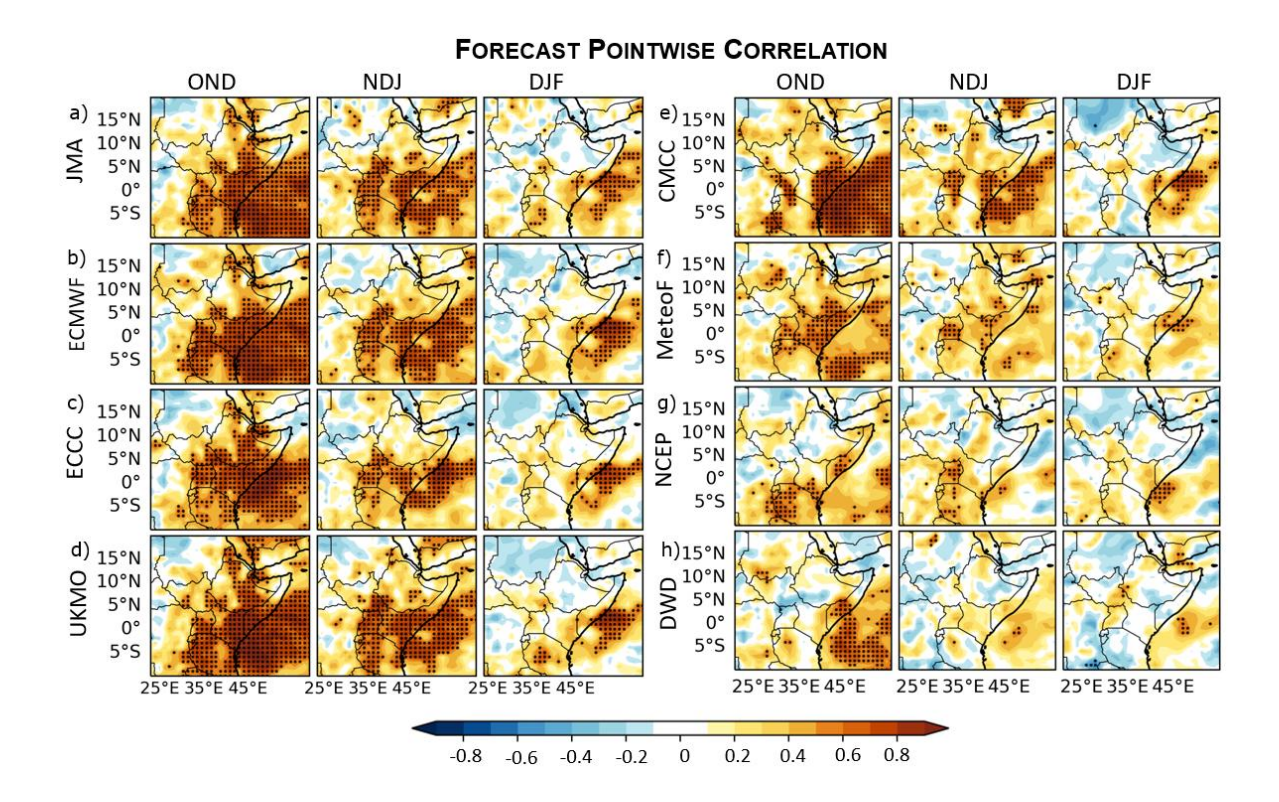


Figure 2.4 Pointwise-correlation maps between GPCP and C3S model predictions for lead season 1 (October-December: OND), lead season 2 (November-January: NDJ), and lead season 3 (December-February: DJF) of rainfall anomalies (ensemble mean) during 1993-2016. Stippling indicates areas where the correlation between the hindcast and observation is statistically significant at a 90% confidence level, as calculated by a two-sided Student t-test for 22(N-2) degrees of freedom.

Furthermore, we also looked at the dependency of the prediction skill on monthly lead-time computing from ACC for patterns of anomalous precipitation. To understand the predictive skills of each model at a specific year, we highlighted the 3 most skillful years in which the models consistently outperform the persistence forecasts for lead time from 1 to 3 months (Fig. 2 .5a-h). Specifically, when compared to persistence forecasts, 75% of coupled models present skillful predictions for the year 1997 at 1-3 lead months. Similarly, only two coupled models, such as UKMO and MeteoF, depict the highest skill in 2010, resulting in the ACC values greater than the persistence at the 2nd lead months (Fig. 2 .5d and f). After lead month 2 (i.e., November, N), there is a decreasing skill, with most years exhibiting significantly lower ACC values compared to the persistent skill level. Overall, precipitation anomalies in

the years 1997 and 2010 are more predictable, with 70% of models presenting ACC values that outperform the persistence skill up to October, that is lead month 2.

To assess the interannual predictive skill of coupled models for the East African short rainy season, we looked at the correlation between the observed and predicted RFa (computed over the EEAR box) across the hindcast periods (Fig. 2.5i). The highest skill was presented in all models during the year 1997. Moreover, the skills of most coupled models are similar during the years 1994, 1999, 2008, and 2010 (Fig. 3i). Particularly, 1994 is the second-most skillful year after 1997, with higher ACC values evident in models such as ECMWF, CMCC, MeteoF, NCEP, and DWD. Similarly, in the year 2008, we observe high correlation values across most coupled models, except for the ECCC and MeteoF. Several years with improved predictive accuracy seem to align with ENSO and IOD events, highlighting the significant impact these climate patterns have on both the variability and predictability of East African rainfall.

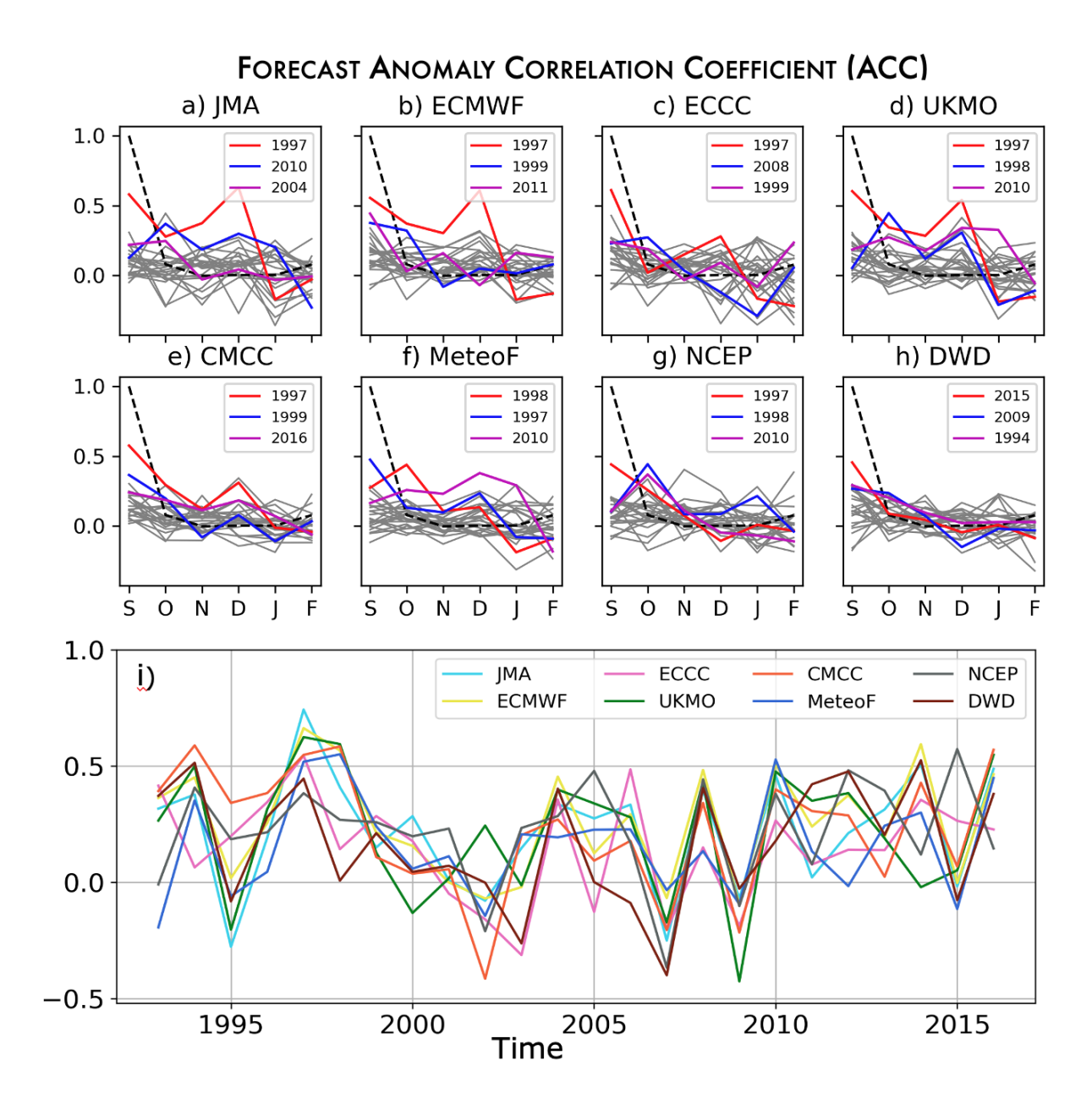


Figure 2.5 Anomaly correlation coefficient (ACC) between GPCP and each C3S model (a-h; upper panels) for monthly rainfall anomaly over part of Eastern Africa (blue dashed box of Fig. 1i) for each year (grey lines) from lead month 0 (September) to lead month 5 (February). In each subfigure, the top three forecasts stand out with distinct colours: the most accurate year is highlighted in red, the second-best in blue, and the third-best in magenta. These forecasts are determined by sorting all predicted years based on their average ACC values across September and October. The black dashed line indicates the persistence forecast. The lower panel (i) illustrates the spatial

correlation between each model and GPCP rainfall anomaly patterns for the OND seasonal mean, calculated over Equatorial Eastern Africa (30–50°E, 5°S-10°N).

2.5 Predictability conditional on ENSO and IOD phases

Several studies have shown how modes of interannual variability in the Indian and Pacific tropical oceans represent a main source of predictability for seasonal rainfall patterns (Palmer & Anderson, 1994; Troccoli, 2010). These studies indicate a clear association between mature phases of IOD and ENSO events (Saji et al., 1999; Behera et al., 2005). Thus, we investigate the role of tropical SST in influencing variability in East African short rains, utilizing indices that monitor rainfall (i.e., EEARi), ENSO, and IOD. Specifically, the Niño 3.4 index (N3.4; SST anomalies averaged over 120°W–170°W, 5°S–5°N) tracks ENSO, while the Dipole Mode Index (DMI; SST anomalies difference between the western Indian Ocean (DMIw), 50°E–70°E, 10°S–10°N, and eastern Indian Ocean (DMIe), 90–110°E, 10°S–0) monitors IOD variability (Saji et al., 1999, Liguori et al., 2022).

The relationship between EEARi, N3.4, and DMI across models (Fig. 2.7a-h) and ERA5 (Fig. 2.7 i) indicates that negative (positive) RFa are consistently linked to the concurrent negative (positive) phases of IOD and ENSO, with the magnitude of the anomaly that depends on the intensity of these two drivers in various years. ENSO and IOD present an important co-variability that results in a significant N3.4-DMI correlation during the OND season in both observations and models (0.74 for the observation and between 0.65 and 0.78 for the models; Fig. 2.7).

The persistence of SST has a significant impact on the variability of rainfall in East Africa. Seasonal rainfall can be significantly impacted by persistent SST anomalies in important locations, such as the Pacific and Indian oceans, which can alter atmospheric circulation patterns and moisture delivery. For example, over portions of East Africa, warmer-than-normal SSTs in the western Indian Ocean are frequently linked to greater convection and rainfall, especially during the short rainy season. Similarly, SST anomalies in the Pacific can cause El Niño and La Niña events, which can either increase or decrease rainfall in the area and cause extremes like droughts or floods.

Therefore, to gain further insight into the impact of local SST fluctuations on the Easta African short rains, we computed the seasonal persistence values over the western Indian Ocean, which is adjacent to the East African coast (Fig. 2.7). Notably high persistence values were found, extending throughout the NDJ season, suggesting that the variations in SST in the western Indian Ocean tend to remain stable for some months which can impact atmospheric conditions during short rainy season in Easta Africa.

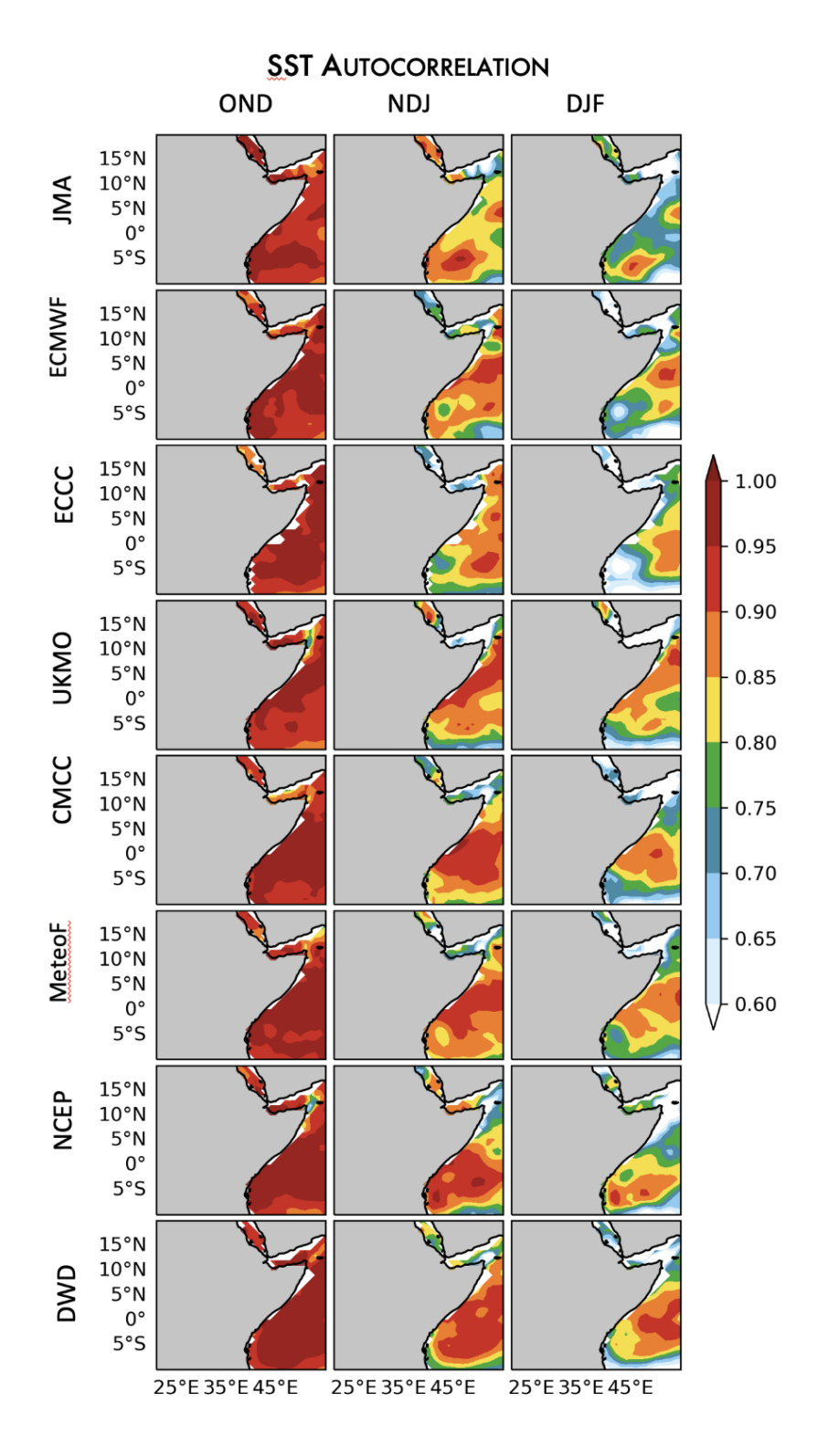


Figure 2.6 SST persistence from lead seasons 1(OND) to 3(DJF) for individual C3S coupled models. Persistence is quantified in each grid point by the autocorrelation between the SON and lead season time series.

When both IOD and ENSO are in the positive phase, all coupled models and GPCP present above-normal OND rainfall (green colors on Fig. 2.8) across the East African region. The best predicted year (Fig. 2.5) is associated with the strongest El Niño event on record (1997/1998), which co-occurred with a strong positive IOD phase. During the short rainy season of 1997, East Africa experienced the largest positive RFa, reaching up to 3 mm/day (Fig. 2.1k). While all models represent a high correlation between ENSO and IOD, the observed extreme 1997 precipitation event is particularly evident only in six out of eight models (i.e., JMA, ECMWF, ECCC, UKMO, CMCC, and NCEP). In this year, however, only the DWD model fails to simulate this RFa event, despite the high correlation between DMI and N34, as presented in Fig. 2.7 h.

On the other hand, during negative ENSO and IOD phases, all models and GPCP tend to exhibit negative OND RFa (as shown by the yellow-filled circles in Fig. 2.7). For instance, during the 1998 negative ENSO and IOD phase (Fall 1998) that immediately followed the record-breaking 1997/1998 El Niño event, the observed negative RFa were successfully forecasted at lead months in only three models, such as UKMO, MeteoF, and NCEP (Fig. 2 .7d, f, and g). However, when lead season is considered, only MeteoF, ECMWF, and JMA can predict an amplitude of the OND anomaly comparable to the observation (Fig. 2.7i). Additionally, 2010 is identified as the second most skillful year by JMA (Fig. 2.7a), and as the third most skillful year by UKMO, MeteoF, and NCEP models (Fig. 2 .7f and g), showing negative OND seasonal anomalies during negative phases of DMI and N34 (Fig. 2 .8a, f, and g).

CONNECTION WITH ENSO AND IOD PHASES

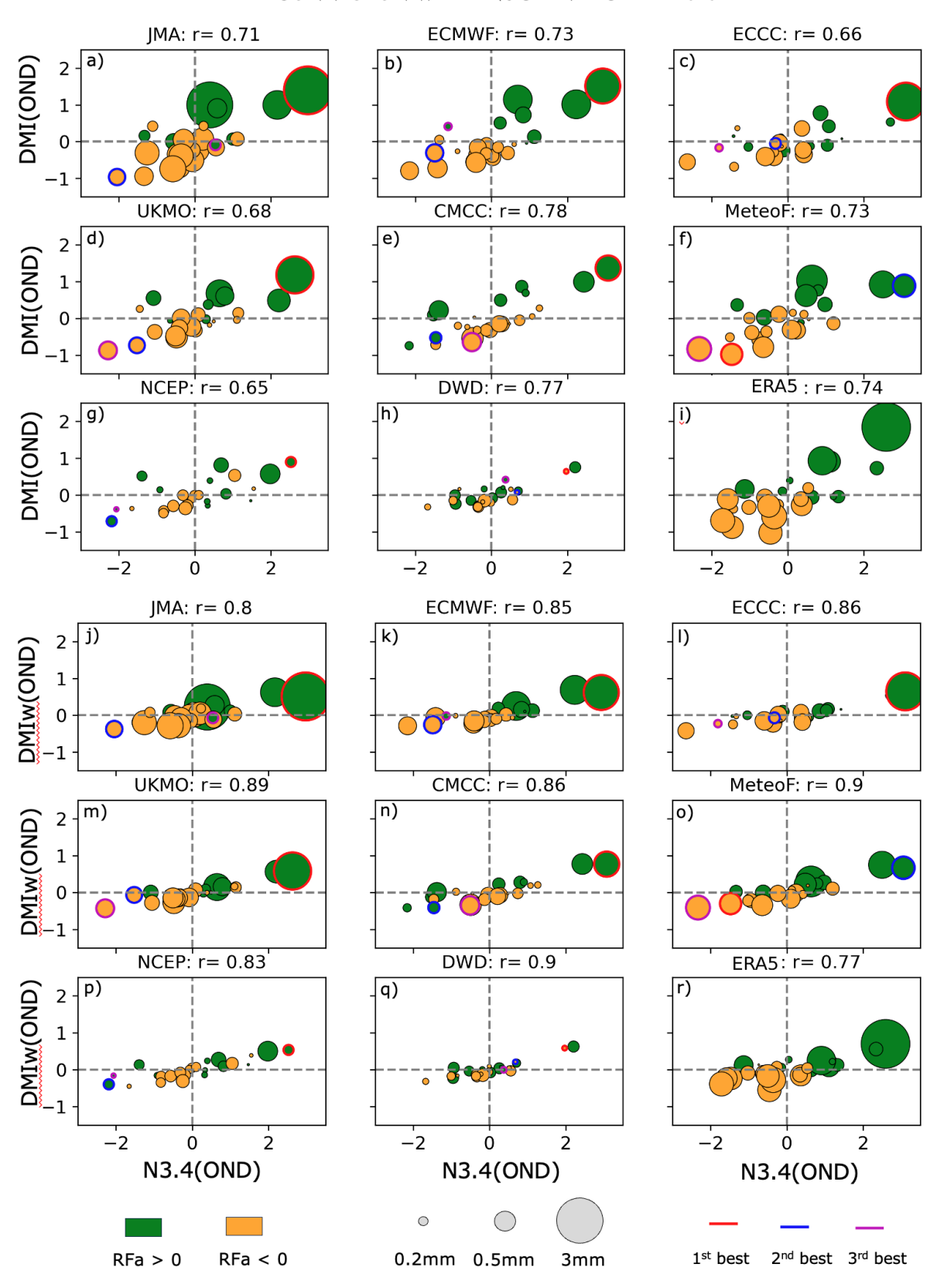


Figure 2.7 Scatterplot of Niño3.4 index (N34; x-axis) versus Dipole Mode Index (DMI; y-axis) during OND season for each of the 24 years analyzed in both model predictions (a-h) and GPCP dataset (i). The area of the circle is proportional to the absolute value of OND rainfall anomaly averaged over part of Eastern Africa (blue dashed box of Fig. 2.1i), with positive (negative) anomaly coloured in green (orange). As in Fig. 2.5 the best forecasted year is highlighted in red, the second-best in blue, and the third-best in magenta. Additionally, the correlation coefficient between N3.4 and DMI is provided at the top of each subfigure for reference. (j-r) shows a similar analysis but with the western pole of the DMI index (DMIw).

El Nino Modoki

The relationship between the El Niño Modoki Index (EMI) and the Dipole Mode Index (DMI) during the OND season across eight seasonal forecast models and the ERA5 observational dataset (Fig.2.8). The EMI is calculated following the methods Ashok et al., (2007) as follows:

$$EMI = [SSTA]_A - \frac{1}{2}[SSTA]_B - \frac{1}{2}[SSTA]_C$$
 (2)

The square bracket in Eq. (2) represents the area-averaged SSTA over each of the regions: A (165°E–140°W, 10°S–10°N), B (110°W–70°W, 15°S–5°N), and C (125°E–145°E, 10°S–20°N), respectively

As shown in Fig. 2.8, a stronger vertical spread of anomalies along the DMI axis indicates that positive DMI events tend to produce larger rainfall anomalies over Eastern Africa, even when EMI values are near zero. While both EMI and DMI contribute to OND rainfall variability, DMI appears to exert a stronger influence on the magnitude of rainfall anomalies, particularly in years with significant IOD activity.

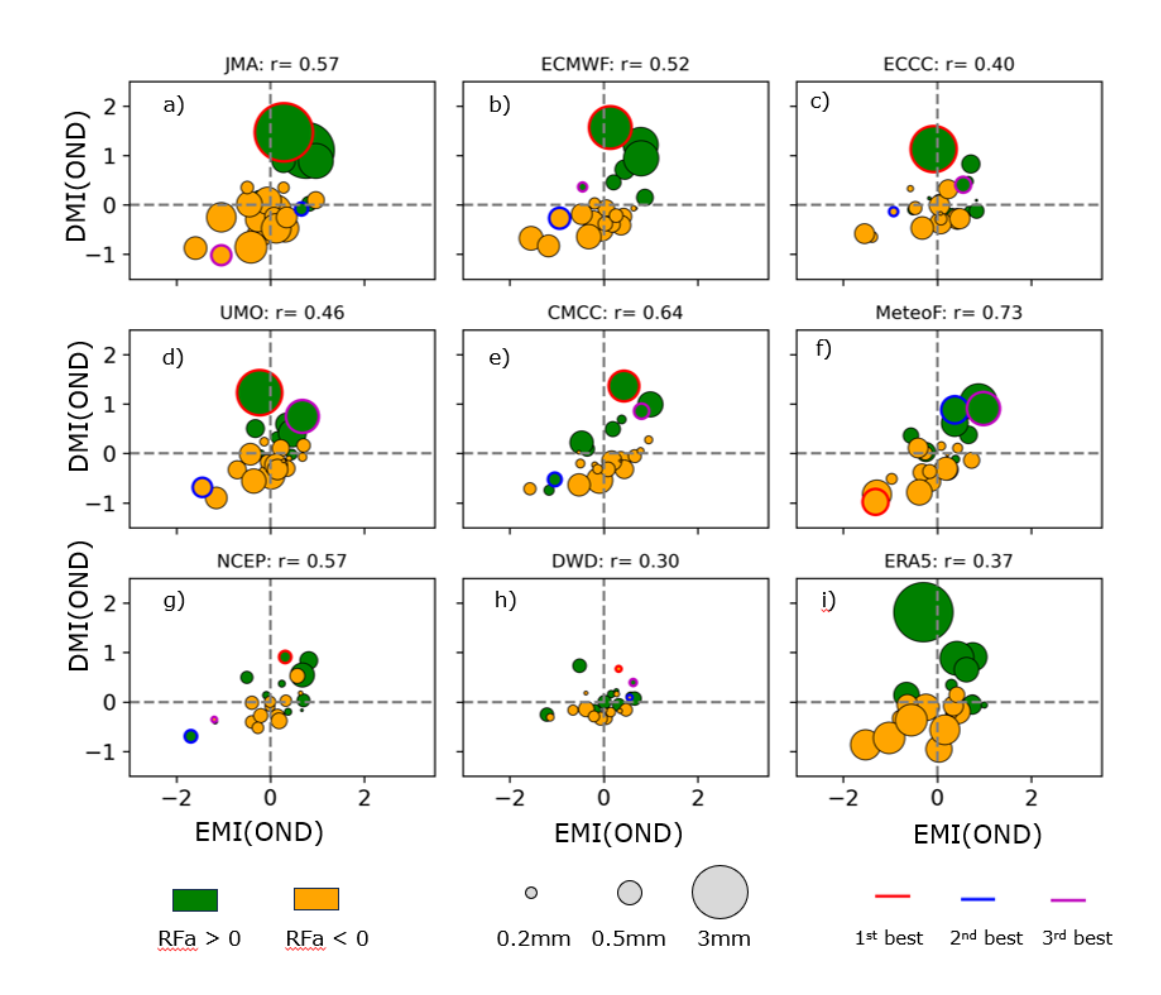


Figure 2.8 Scatterplot of El Niño Modoki index (EMI; x-axis) versus Dipole Mode Index (DMI; y-axis) during the OND season for each of the 24 years analyzed in both model predictions (a-h) and GPCP dataset (i). The area of the circle is proportional to the absolute value of OND rainfall anomaly averaged over part of Eastern Africa (blue dashed box of Fig. 2.1i), with positive (negative) anomaly coloured in green (orange). As in Fig. 2.5 the best forecasted year is highlighted in red, the second-best in blue, and the third-best in magenta.

Given the vicinity of East Africa to the Western pole of the IOD (i.e., DMIw region), we wanted to explore if the interannual variability of East African short rain was more strongly connected to fluctuations in the DMIw index, which has been shown to exhibit slightly higher predictability (Bahaga et al., 2016). However, despite this geographical closeness, the correlation between OND RFa in the EEAR region (i.e., EEARi) and DMIw is slightly lower than the correlation between EEARi and the overall DMI (see Fig. 2.9). This finding is remarkable considering that ENSO presents

a stronger connection with the DMIw compared to the DMI, as evidenced in both observational data and climate models (Fig. 2.7 j-r). The stronger correlation between EEARi and the DMI, despite the expectation that local SST variations would play a more significant role, emphasizes the importance of broader-scale IOD variability. This suggests that the key factor influencing East African rainfall is the IOD-driven disruption of the zonal atmospheric circulation associated with the Indian Ocean branch of the Walker Circulation (see Fig. 2.8).

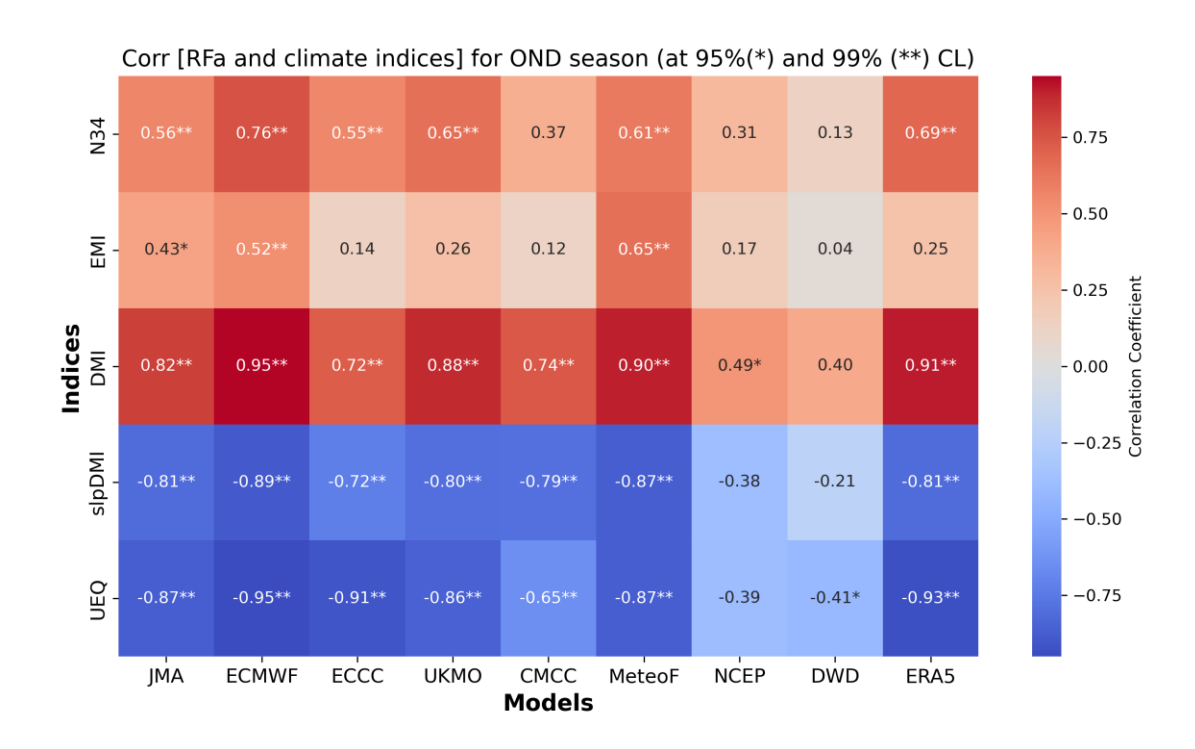


Figure 2.9 Correlation between East African RFa index and climate indices for the OND season. Asterisks (*) and (**) indicate significance at the 95% and 99% confidence levels, respectively. The RFa index is the area-averaged over Eastern Africa (30–50°E, 5°S-10°N) for both models and ERA5

In addition to DMI and N34, we have also computed the correlation between the sea level pressure (SLP) and the rainfall anomalies to illustrate the association between the variation of SLP and the East African rainfall during the OND season. To do this, following the methods of Behera &Yamagata (2003), the SLP anomaly index is computed over the DMI region (slpDMI; Fig. 2 .10c) and equatorial wind anomaly index (UEQ; Fig. 2 .10d), evaluated across multiple models and observational datasets. The association between seasonal OND RFa anomalies index and each index from

ERA5 and individual models is evaluated at a statistical significance of 95% and 99% confidence level. As a result, the SLP dipole index is significantly negatively correlated with the SST dipole index during the OND season, which is displayed in most models and observational data sets (ERA5; black dots line shown in Fig. 2.10), which serves as a reference. The same is true for UEQ anomalies, representing equatorial wind anomalies. Both ERA5 and models demonstrate consistently high negative correlations with EASRi during the OND season. Relatively, EASRi has a negative correlation with UEQ presented in the NCEP and DWD models, showing correlation coefficients of 0,41 and -0.39, respectively.

The interannual variability of East African short rains is linked to canonical El Niño and El Niño Modoki events, with notable peaks during the 1997-98 and 2015-16 El Niño episodes. Both indices show interannual variability but with different amplitudes and peak years (Fig. 10, a and b). For example, during 1997–1998, both indices peaked, indicating a strong canonical El Niño. However, in some years, like 2004, 2009, and 2014, show stronger EMI than N34, suggesting those may be El Niño Modoki years. The second panel displays DMI anomalies for each model, showing strong agreement with ERA5. Similarly, the third panel, reflecting sea level pressure variations over the DMI region, we call it slpDMI (Behera et al, 2005). The negative slpDMI anomaly (Fig. 2.8) observed during positive DMI and ENSO events indicates the interplay between warmer SSTS, altered convection patterns can shift the Walker circulation over the tropical Indian Ocean. Similarly, negative UEQ is observed during both positive ENSO and positive IOD occur together, suggesting their combined effects strengthen the disruption of zonal wind patterns. More noticeable is the trade winds' reversal or weakening. Negative U-wind anomalies are strengthened by the suppression of the normal east-to-west wind flow caused by the diminished zonal pressure gradient across the Pacific and Indian tropical oceans.

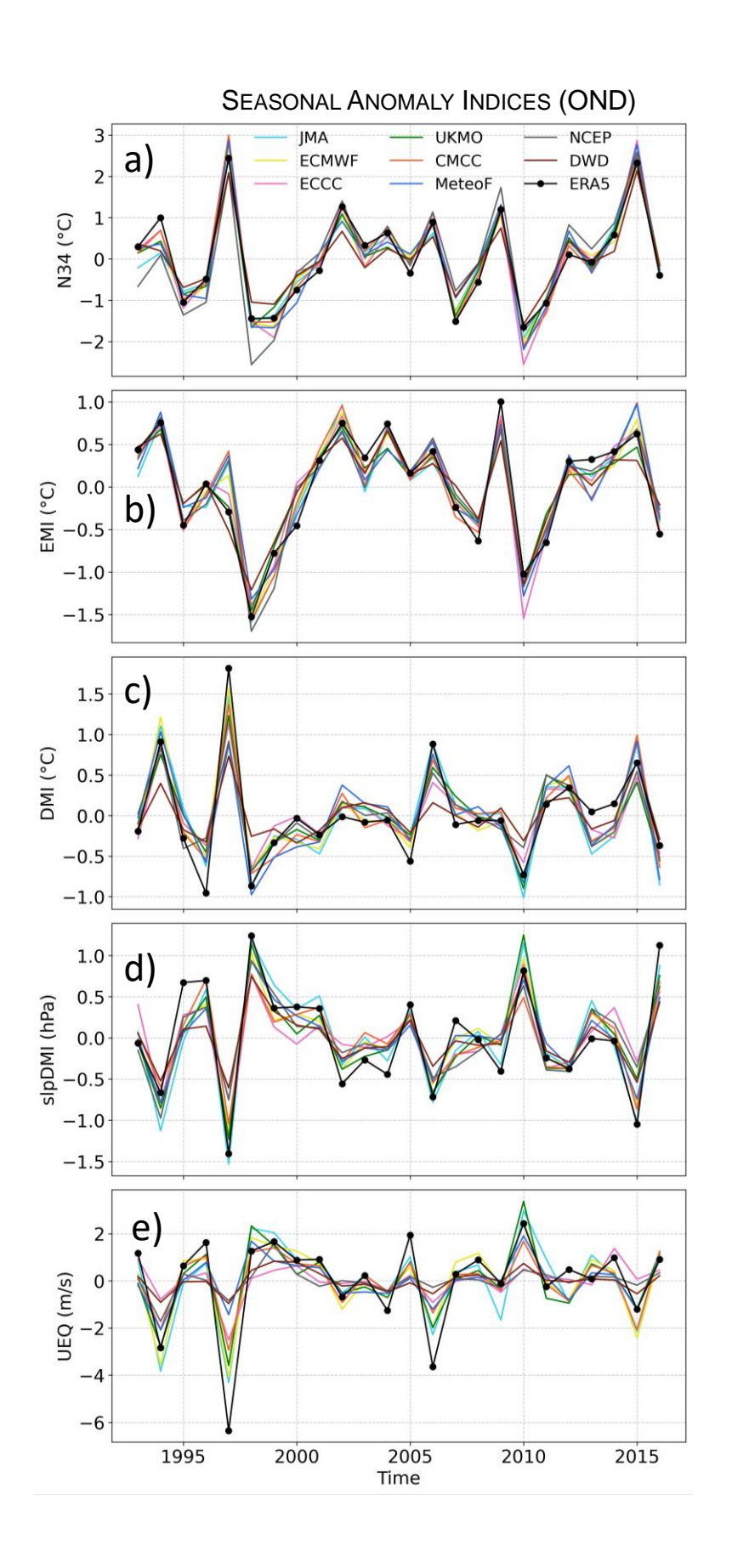


Figure 2.10 Interannual variation of short rainy season derived from ERA5, and individual coupled models' ensemble mean field anomalies: a) N34, b) EMI, c) DMI, d) sea level pressure anomaly index over DMI region (slpDMI), e) Equatorial wind anomaly index (UEQ).

2.6 Discussion and Conclusion

In this study, we evaluate the predictability of East African short rains using eight state-of-the-art seasonal retrospective forecast systems from the Copernicus Climate Change Service (C3S), with a focus on forecasts initialized at the onset of the OND rainy season, namely in September. Despite the presence of localized biases (Fig. 2.1), most models demonstrate appreciable skill in predicting OND precipitation anomalies across much of East Africa, although regions in northern and western parts of the study region remain challenging, exhibiting low or no skill.

Importantly, the models show considerable skill extending into the DJF season along coastal East Africa, particularly near Somalia and parts of the western Indian Ocean. This is likely linked to persistent SST anomalies in the western Indian Ocean (Fig. 2.6), which remain significant well into the boreal winter across most models. These findings align with previous evaluations of the SINTEX-F1 model (Behera et al., 2005) and the APCC Ocean–Atmosphere coupled multi-model ensemble (Bahaga et al., 2016), confirming the relevance of oceanic memory in sustaining forecast skill beyond the target season.

Robustness of model performance is further supported by analyses using different verification datasets (e.g., ERA5 reanalysis), which show minimal variation in skill scores (Fig. 2.2). However, the anomaly correlation at various lead times (Fig. 2.7) reveals a strong interannual dependency of model skill, particularly within the first six months. For instance, 2010 emerges as the second most skilful year only when ERA5 is used as the reference, illustrating some sensitivity to the verification dataset. These variations highlight the influence of major tropical modes of variability—especially ENSO and IOD—on regional predictability (Hastenrath et al., 1993; Behera et al., 2005; Wang et al., 2009).

Particularly, skilful years often coincide with mature ENSO and IOD phases, with the most significant rainfall anomalies recorded during years when these modes occur simultaneously. Although El Niño years are typically associated with intense OND precipitation, the correlation between rainfall anomalies (RFa) and the Dipole Mode Index (DMI) is generally stronger than the correlation with Niño3.4 (N3.4) SST anomalies. This suggests that the Indian Ocean SST response to ENSO exerts a more pronounced influence on East African rainfall than ENSO's direct teleconnections via atmospheric bridges. In most cases, the sign of the DMI successfully predicts the sign of seasonal rainfall anomalies, a consistency not always matched by N3.4. This finding resonates with earlier research emphasising the east—west SST dipole and associated atmospheric circulation patterns as key drivers of East African short rains (Yamagata et al., 2002; Black et al., 2003).

Surprisingly, the extreme 2015/2016 El Niño event—one of the strongest on record—posed significant challenges for most models, which struggled to accurately simulate the rainfall patterns during the OND season. Only the NCEP and ECCC models (Fig. 2.3i) captured these anomalies adequately. The underperformance is likely due to the relatively weak positive IOD phase in 2015/2016 compared to the 1997/1998 El Niño, which limited the amplification of the Indian Ocean Walker circulation (Macleod & Caminade, 2019). This underscores the complex and non-linear interactions between ENSO and IOD in shaping East African rainfall. We also analysed that canonical El Niño, positive IOD, and El Niño Modoki contribute to enhanced East African rainfall. Compared to the IOD, both indices (N34 and EMI) exhibit interannual variability with similar amplitudes (Fig. 10 and b), however, they show a weaker correlation with OND RFa. In some years, for instance, 1997–1998 saw peaks in both indices, indicating a strong canonical El Niño. Beyond Walker circulation, this driver also impacts African rainfall by altering jet stream dynamics, particularly weakening the tropical easterly jet and shifting the African easterly jet southward, reducing rainfall in northern tropical regions like the Sahel (Preethi et al., 2015).

Furthermore, both model simulations and observational data reveal that negative sea level pressure anomalies (slpDMI) during concurrent positive ENSO and IOD events are associated with intensified convection and significant changes in the

Walker Circulation over the tropical Indian Ocean. These atmospheric responses are well represented in the models, as evidenced by their strong agreement with ERA5 slpDMI anomaly patterns. At the same time, negative upper equatorial wind (UEQ) anomalies point to a synergistic effect of ENSO and IOD in altering zonal wind patterns—weakening or even reversing the trade winds—via a reduced zonal pressure gradient across both the Pacific and Indian Oceans. Collectively, these feedback mechanisms significantly influence the variability of OND rainfall in East Africa. Despite the region's proximity to the western pole of the IOD, the strongest correlations with rainfall appear when both eastern and western poles are considered. This suggests that broader-scale IOD variability and its associated impact on the Walker Circulation play a more dominant role than local SST anomalies in driving rainfall variability.

In summary, while current seasonal forecast models show promising skill in capturing OND rainfall anomalies across East Africa, particularly when both ENSO and IOD phases are accurately represented, limitations remain, especially in simulating complex interactions during extreme years. These findings highlight the importance of improving model representations of Indo-Pacific climate variability and their coupled teleconnections to enhance seasonal forecasting in this highly vulnerable region.

3 FORECASTING EAST AFRICAN LONG RAINS

3.1 Introduction

East African long rains, which run from March to May (MAM), are known locally as Gu in Somalia, *Belg* in Ethiopia, and Masika in Kenya, Tanzania, and Uganda. Its variability is linked to the migration ITCZ, which is taken as a major factor in the East African long rains (MacLeod, 2019; Yang et al., 2014). When the ITCZ shifts northward, it brings more moisture and convective activity. SSTs of the nearby Indian oceans, such as the Indian, and in the broad-scale air circulation patterns, affect its position and intensity. Changes in the ITCZ's position can cause variations in the long rains' timing, intensity, and spatial distribution, which frequently lead to either droughts or floods in EA (Lashkari & Jafari, 2021; Nicholson, 2018). Due to the significant rainfall it brings, which boosts agricultural production, restores water supplies, and increases economic activity, this season is vital to the region (MacLeod, 2019). The long rains are particularly vital for food security, as they coincide with key planting and growing periods for staple crops. Its significance underscores the need for accurate forecasting to mitigate risks associated with variability, such as droughts or flooding, which can disrupt these critical sectors (Roy et al., 2024).

During the last 30 years, East Africa has experienced a persistent decline in rainfall during the long rainy season (Funk et al., 2008; Williams and Funk, 2012). This has had major consequences for regional food security, where agriculture largely depends on rainfall and is thus highly vulnerable to climatic change (Funk et al., 2008; Lyon, 2014). It is unclear whether this decline is caused by internal multidecadal variability associated with changes in the tropical Pacific (Yang et al., 2014) or anthropogenically driven warming in the Indian Ocean or western Pacific region (Liebmann et al., 2014). Furthermore, this declining trend is confirmed by recent studies such as Palmer et al. (2023). Since 1985, marked variability and consistent negative trends in the long rains have been detected. Unusual rainfall during long rains can result in droughts over the region (Nicholson, 2017a). Due to this, it has led to persistent droughts, which have had increasingly severe impacts the agriculture and the broader economy in recent decades. For instance, from 2008 to 2010, the Horn of Africa

experienced a drought that affected over 13 million people, and it cost about \$1 billion to respond to the crisis. This widespread drought exemplified the dire consequences of unpredictable weather patterns in East Africa, leading to a significant humanitarian crisis (Amha et al., 2023; Gebremeskel et al., 2019).

Over the past two decades, EA experienced many drought episodes during the long rains, leading to severe food insecurity (Funk et al., 2014). For instance, between April 2016 and December 2017, Somalia experienced three extremely poor rainy seasons, which created a persistent and extensive drought that caused significant losses in livestock and agricultural harvests (Funk et al., 2018). These extreme events, observed over many years, are linked to the variability of sea surface temperature in the tropical oceans (Gebremeskel et al., 2019; Saji N. et al., 1999). Recurrent droughts are often associated with negative phases of SST anomalies over the central Pacific Ocean (Park et al., 2020). Numerous scholars have underlined that the variability in East Africa's long rains is driven by both local factors, such as topography and land use, and remote drivers (Nicholson, 2017).

Driving mechanisms of long rains variability and trends are connected to local and global drivers that influence atmospheric circulation, ocean temperatures, and precipitation patterns (Camberlin & Philippon, 2002; Palmer et al., 2023; Walker et al., 2020). ENSO plays a significant role in influencing the long rains in East Africa, with its various phases driving changes in precipitation patterns and variability (Vellinga & Milton, 2018b). Typically, strong El Niño events increase atmospheric moisture, often leading to enhanced rainfall. However, during La Niña conditions, particularly following strong El Niño episodes, warmer SST in the western Pacific can correspond to drier conditions over East Africa (Indeje et al., 2000). During the 2016–2017 period, weakened Walker circulation due to El Niño, along with increased SSTs in the central and eastern Pacific, disrupted rainfall patterns and contributed to the dry seasons and droughts over East Africa observed (Funk et al., 2018). However, the tropical ocean and East African rainfall are complex and can result in both wetter and drier conditions. As the IOD peaks between September and November, long rain variability is less responsive to changes in IOD (Shaaban & Roundy, 2017).

However, the long rains are primarily influenced by ENSO, particularly through its associated atmospheric teleconnections, rather than through interactions with the Indian Ocean. Lyon and DeWitt (2012) found that the decline in long rains is closely linked to abrupt changes in the tropical Pacific, challenging earlier suggestions that emphasized the role of the Indian Ocean. Variations in zonal wind patterns, including regional monsoonal flows and the Walker circulation's strength, are also quite important (Nicholson, 2017). The intricacy of East Africa's climate system, where several factors work together to affect seasonal rainfall variability. The increased or suppressed rainfall during the long rainy season is also associated with MJO phase, which is the eastward movement of oceanic and atmospheric phenomena along the tropics (Pohl and Camberlin, 2006a; Hogan et al., 2015). These studies have shown that during MJO phase 2-4, negative rainfall anomalies were observed across the coastal and, while positive rainfall anomalies were observed over the highland. Based on this research, the mechanisms causing these up to three-week-long wet/dry episodes are well understood (Hogan et al., 2015; Nicholson, 2017). However, the impact of MJO on the long rains is not easily understood, involving changes to intraseasonal aspects such as onset timing and frequency of extreme events (Pohl and Camberlin, 2006b). According to Yang et al. (2020), there is also evidence that the Quasi-Biennial Oscillation (QBO), a stratospheric zonal wind pattern, influences the strength of convection and circulation patterns, which in turn influence rainfall during long rainy seasons.

Variability in East African long rains is also greatly influenced by regional characteristics, including moisture recycling and land-atmosphere interactions. Surface evaporation rates are influenced by changes in plant cover and soil moisture, and these variations contribute to localized convective processes. Rainfall distribution is influenced by topography, especially the Rift Valley and the Ethiopian Highlands, which alter moisture transport and wind patterns (Diem et al., 2014). Moreover, moisture advection from the Indian Ocean is influenced by the interplay of monsoonal winds and the Somali Jet, with stronger winds generally carrying more moisture into the area (Funk et al., 2016; Jain et al., 2021). Increasing an understanding of these mechanisms is essential for seasonal forecasting using dynamical models such as C3S models, which may promise to anticipate long rains fluctuation ahead of the season.

In this chapter, we used dynamical multi-system seasonal retrospective forecasts from the C3S to investigate the predictability of the long rains over EA. These predictions employ state-of-the-art seasonal prediction methods, designed to capture the complex climate dynamics impacting rainfall patterns. Here, we investigated whether the dynamical seasonal prediction systems accurately replicate the temporal and spatial characteristics of the long rainy season. We also identify which forecast systems can describe the MAM rainy season, which enables us to understand the connection with large-scale climatic drivers. This allows us to assess further the models' predictive accuracy across a range of temporal resolutions and investigate how the prediction systems' accuracy was affected by significant climate modes. We try to understand how these teleconnections influence East African long rain patterns and if the models sufficiently consider the interactions by analysing their separate and combined effects. Therefore, in this chapter, we evaluate the predictability of long rains by dynamical multi-system seasonal retrospective forecasts by addressing key questions: Do dynamical seasonal prediction systems reproduce the long rainy seasonal pattern? Which climate drivers are more influential on MAM rainfall variability? When and why is the forecast skill higher or lower, i.e., conditional predictability? Furthermore, we have checked the model's skill dependence on ENSO and IOD phases, considering both their independent and combined effects on the East African long rain pattern.

3.2 Datasets, models, and methods

In this chapter, we focused on the long rains' predictability. We applied the same datasets, models, and methods used to investigate Short Rains and described them in chapter 2, section 2.2.2.

3.3 Model Climatology and Inter-annual variability

To evaluate the capability of the dynamical models to accurately reproduce East African seasonal rainfall patterns during the long rain season, we compared the climatology of the ensemble mean of individual models with the operational dataset. The climatology and interannual seasonal anomaly for models and observational datasets for Season 1 (March-May, MAM) as initialized in February (Figure 3.1). The

rainfall anomaly indices for the MAM season are averaged over Equatorial Eastern Africa (30–50°E, 5°S–10°N), as shown by the blue dashed box in Figure 3.1. The observational datasets (Fig.3.1 i and j) display maximum rainfall over Lake Victoria Basin and the Ethiopian Highlands, regions known for their heavy rainfall during the long rains season. Similarly, most models displayed high rainfall over the highlands and the western part of the region, particularly near the equator. However, the DWD tends to underestimate the rainfall over the highlands, this discrepancy may be attributed to the coarse resolution of the model ensemble compared to observational reanalysis, which can make it challenging to capture topographic effects and localized convection accurately.

The interannual variability of the long rainy season is presented (Fig. 3.1 k) by averaging over part of equatorial East Africa between 5°S-10°N and 30°-50°E (blue box in Fig. 3.1i) following a similar approach to Palmer et al. (2023). The index reveals that 1998 appears to represent the peak rainfall for most coupled models, which is not shown in ERA5. However, compared to GPCP, most models significantly overestimate this event. The observational dataset presents higher interannual variability than models, as the ensemble means smoothing out most of the internal variability that grows from the perturbation in the initial conditions. Despite the observed variability, models and observations generally align well during years of strong positive rainfall anomalies, such as those in 1998 and 2010.

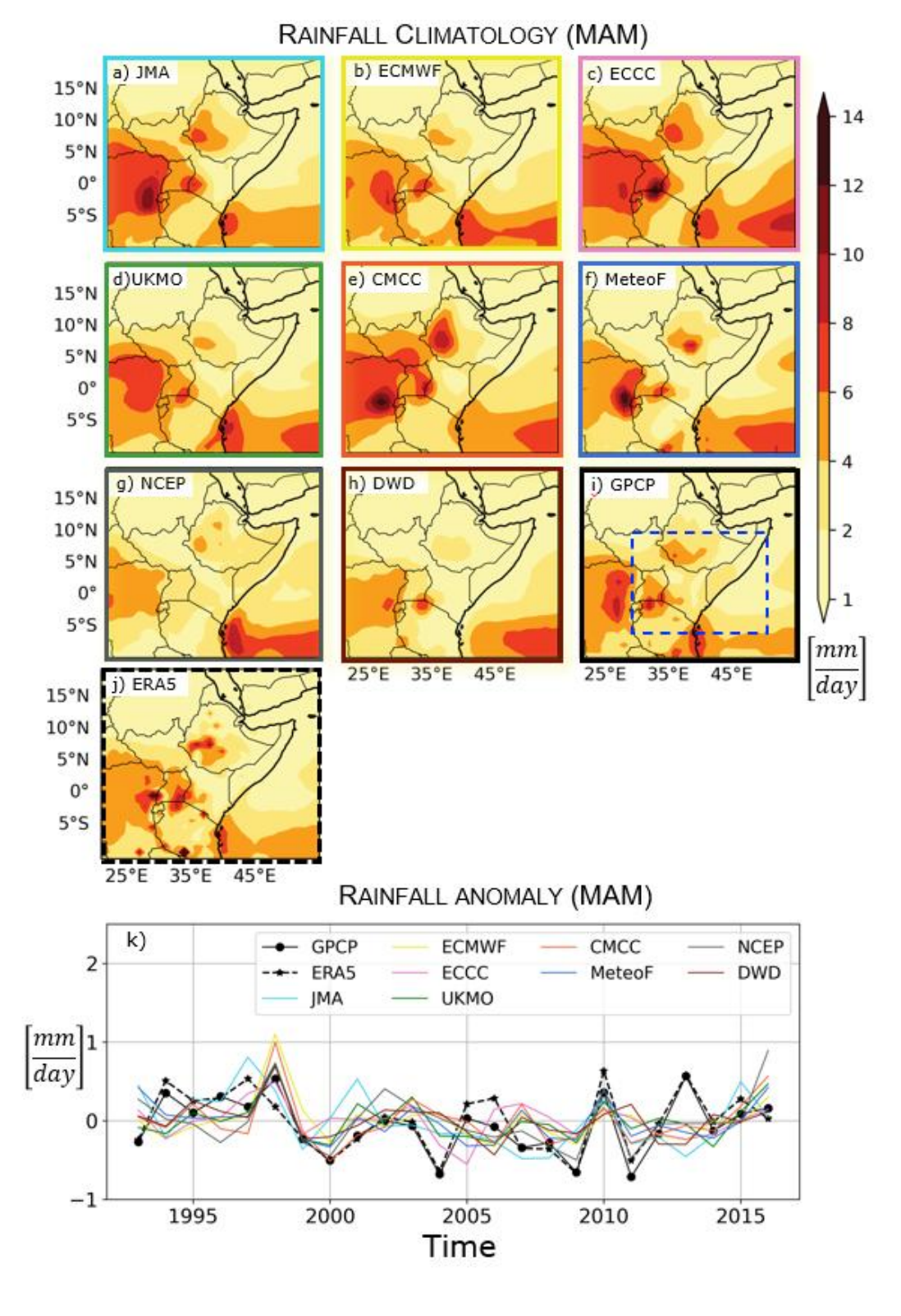


Figure 3.1 Seasonal rainfall climatology during the long rains (Maech-May: MAM) derived from GPCP (i), ERA5 (j), and the seasonal prediction systems from C3S, which includes 8 ocean-atmosphere coupled model ensembles and cover the period 1993—

2016 (a-h). The lower panel shows area-averaged MAM rainfall anomalies for parts of Eastern Africa (30–50°E, 5°S-10°N; blue dashed box in i) for models, ERA5, and the GPCP dataset. Anomalies are computed relative to the climatology shown in the upper panel.

The spatial pattern of rainfall variability during MAM season is represented by the inter-annual standard deviation for both models and GPCP dataset (Fig. 3.2). Over the ocean, GPCP presents maximum variability over Southwest parts of the Indian ocean at while in the model this is true only for ECCC, UKMO, and NCEP. Furthermore, several models but especially JMA, ECCC, MeteoF, and CMCC presents a significant variation in OND season over East African highlands. However, in most lands both observational products and models exhibit less rainfall variability. As GPCP climatology pattern, most of the coupled models show less rainfall variability is shown in Northern parts of East Africa.

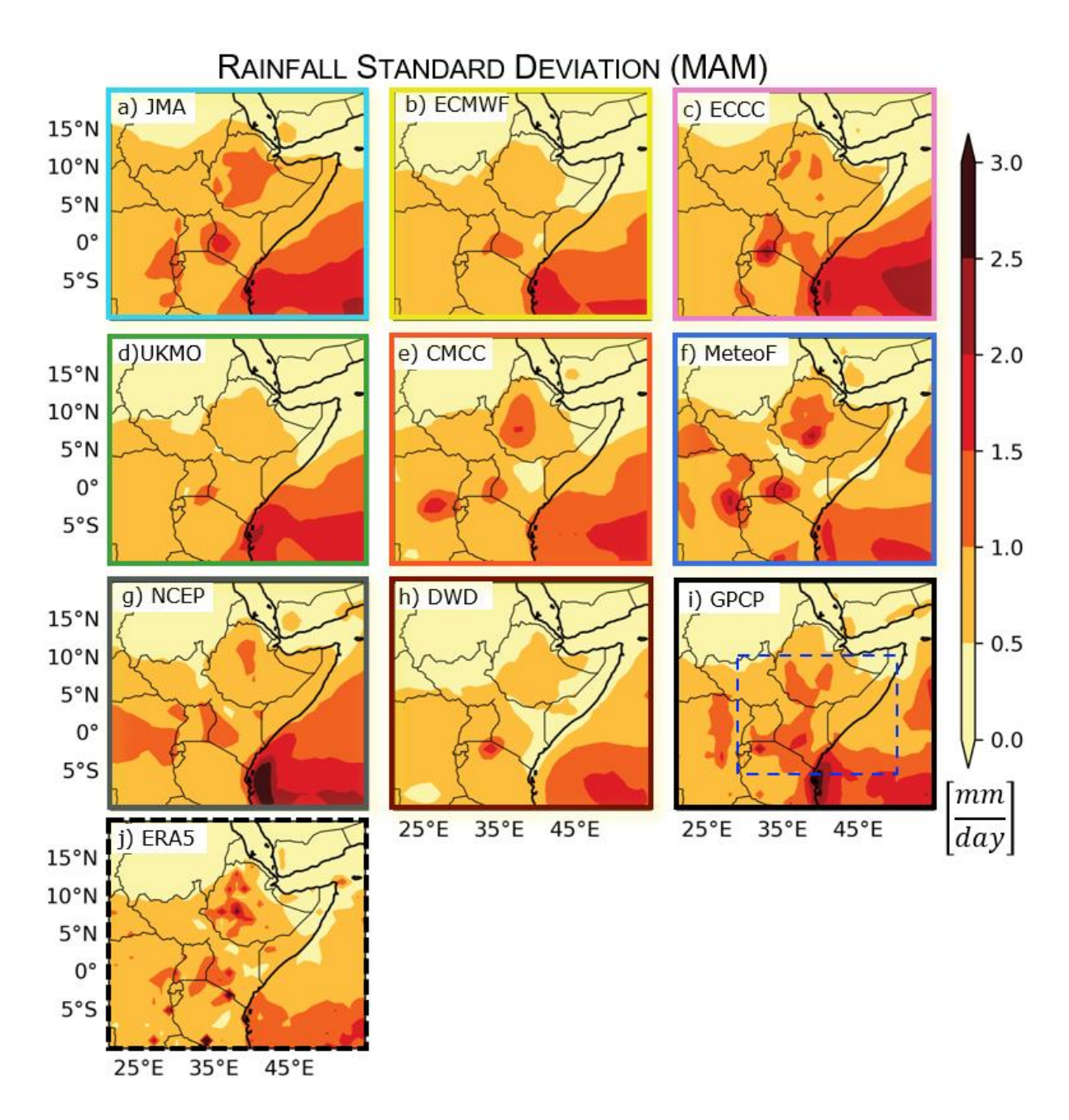


Figure 3.2 Seasonal rainfall standard deviation during the long rains (MAM) derived from the seasonal prediction systems from C3S, which includes 8 ocean-atmosphere coupled model ensembles and covers the period 1993–2016 (c-j) and GPCP (i), ERA5 (j) datasets.

The model biases are computed over the East African region throughout three consecutive lead seasons, i.e., lead1(March-May, MAM) and the months that follow lead2(April-June, AMJ), and lead3 (May-July, MJJ), shown in Fig. 3.3. The biases are calculated as the difference between the GPCP dataset, and the ensemble mean of the

individual models. Models like JMA, ECCC, CMCC, and MeteoF show notable positive biases at lead seasons 1 and 2, suggesting an overestimation of precipitation over the Congo Basin and the southwestern portions of the region. Particularly, models such as CMCC and MeteoF exhibit a significant overestimation of precipitation over the Ethiopian humid highlands, with the first two lead seasons showing up to 6 mm/day. It is noteworthy that the MeteoF model shows the tendency for these positive biases to increase with lead time, indicating the challenges of sustaining reliability over long forecasting lead seasons. These findings highlight the necessity of better model calibration, especially to capture rainfall variability in important areas such as the major highlands.

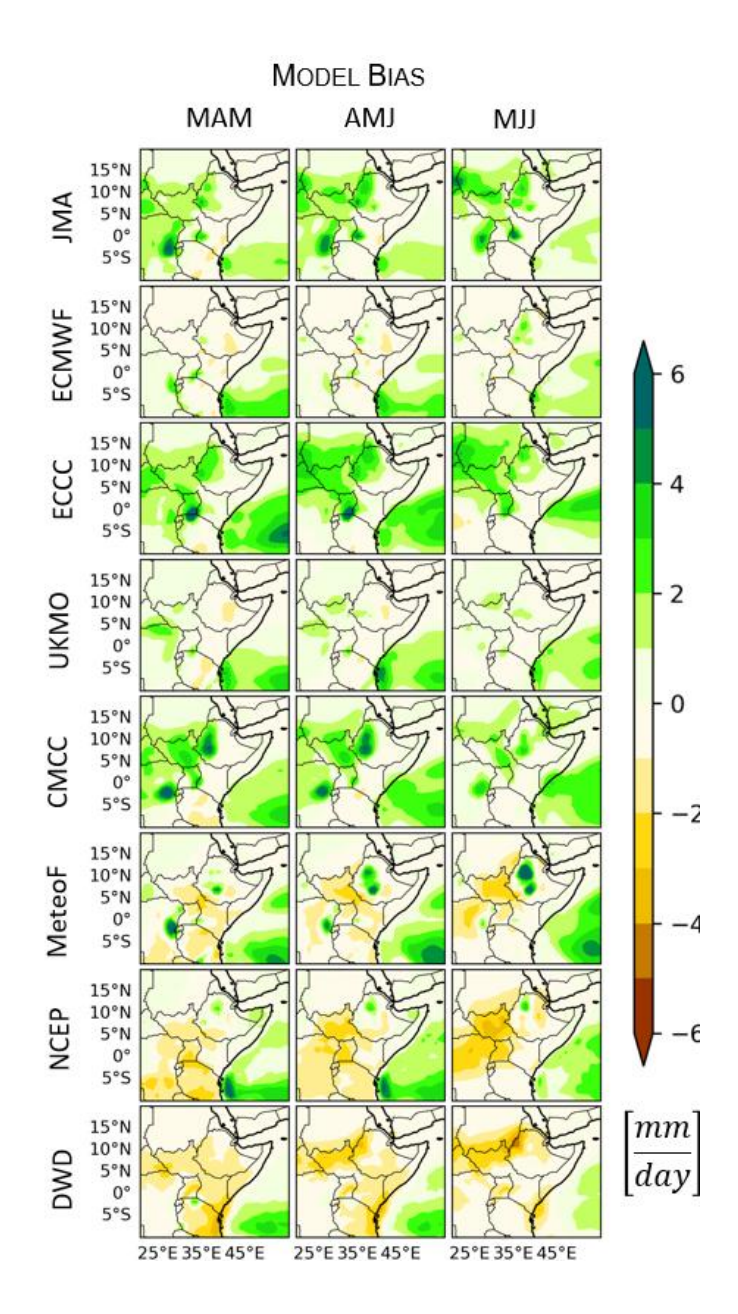


Figure 3.3 Mean bias (Model-GPCP) for C3S model predictions for lead season 1 (March-May: MAM), lead season 2 (April-June: AMJ), and lead season 3 (May-July: MJJ) of rainfall climatology (ensemble mean) which initialized in February during 1993-2016.

3.4 Predictive skill of coupled models

To evaluate the predictive skills of models in forecasting East African long rain pattern, we applied the spatial and temporal anomaly correlations. The ACC analysis is a common statistical metric used to measure the spatial (or temporal) correlation between the simulated and the observed anomaly (section 2.2.3 in chapter 2). Observational datasets such as GPCP and ERA5 are often used as benchmarks for evaluating model performance. Using forecasts initialized in February for the 1993– 2016 hindcast period, we computed pointwise ACC to assess the models' predictive skill in reproducing EA long rains at lead seasons 1 (MAM), 2 (AMJ), and 3 (MJJ). Most models, higher skill appeared across the western Indian Ocean, whereas less or no skill was observed in many parts of the land, especially over highlands. This indicates that most models are shown consistently in replicating the EA long rains. However, throughout all lead seasons, some models like UKMO and NCEP show skill, particularly across portions of the central highlands and Western parts of the Indian Ocean. Some models, such as CMCC and UKMO, exhibit a significant forecasting skill across Northern Eritrea, the Red Sea, and the southern west Indian Ocean up to lead season two. However, as the lead time increases, the model's skill declines, suggesting a reduction in accuracy for longer forecasts. In general, in the case of long rainy seasons, we have seen that different models have varying prediction abilities, as the ACC plots across lead seasons 1 (MAM), 2 (AMJ), and 3 (MJJ) reveal variations in the models' ability to predict rainfall anomalies.

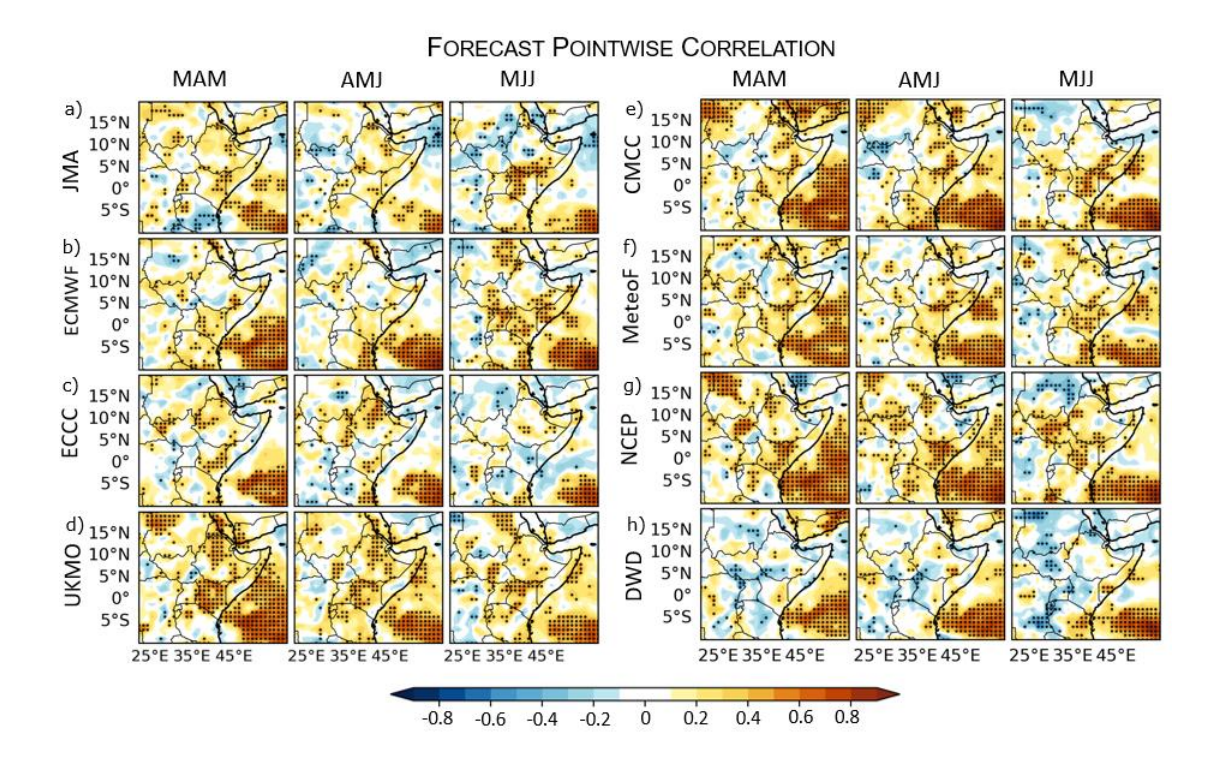


Figure 3.4 Pointwise-correlation maps between GPCP and C3S model predictions for lead season 1 (May-March: MAM), lead season 2 (April-June: AMJ), and lead season 3 (May-July: MJJ) of rainfall anomalies (ensemble mean) during 1993-2016. Stippling indicates area where the correlation between the hindcast and observation are statistically significant at 99% confidence level, as calculated by a two-side Student t-test for 22(N-2) degrees of freedom.

The dependency of the prediction skill on monthly lead-time is evaluated against GPCP anomaly (Fig 3.5 a-h). To understand monthly predictability of long rain, we evaluate the anomaly of each model at specific year. First, we identify the 3 most skillful years (highlighted in colors) in which the models consistently outperform the persistence forecasts for lead time from 1 to 3 months' (Fig. 3a-h). Specifically, when compared to persistence forecasts, 5 out of 8 models present the highest skillful predictions for the year 1997 at 1-3 lead months. Similarly, only two coupled models, ECCC and UKMO, depict the high skill in 1998 and 2010 resulting in the ACC values greater than the persistence at the 2nd lead months (Fig. 3.4 c and d). After lead month 2 (i.e., November, N), there is decreasing skill, with most years exhibiting significantly lower ACC values compared to the persistent skill level. Overall, precipitation

anomalies in the years 1997-1999 are more predictable, with most dynamical prediction systems presenting ACC values greater than the persistence skill. From the monthly dependent ACC, the MAM season models can predict monthly rainfall patterns with noticeable variation within models, highlighting the forecast accuracy decreasing across lead months.

The interannual predictive skill of c3s models for the East African long rains (MAM) is analyzed (Fig 3.5 i). Here, we looked at the correlation between the observed and predicted RFa (the index computed over the blue box indicated in Fig.3.1i: EEARi) across the hindcast periods (1993-2016). The highest skill presented in all models, except MeteoF, during the year 1998. Even though 1997 is the most skillful year identified at monthly lead ACC (Fig 3.5 a-h), at lead season (MAM), the low skill evident in models (Fig 3.5 i). Similarly, in the year 2010 they also presented high correlation values across most coupled models, except for the ECCC and MeteoF.

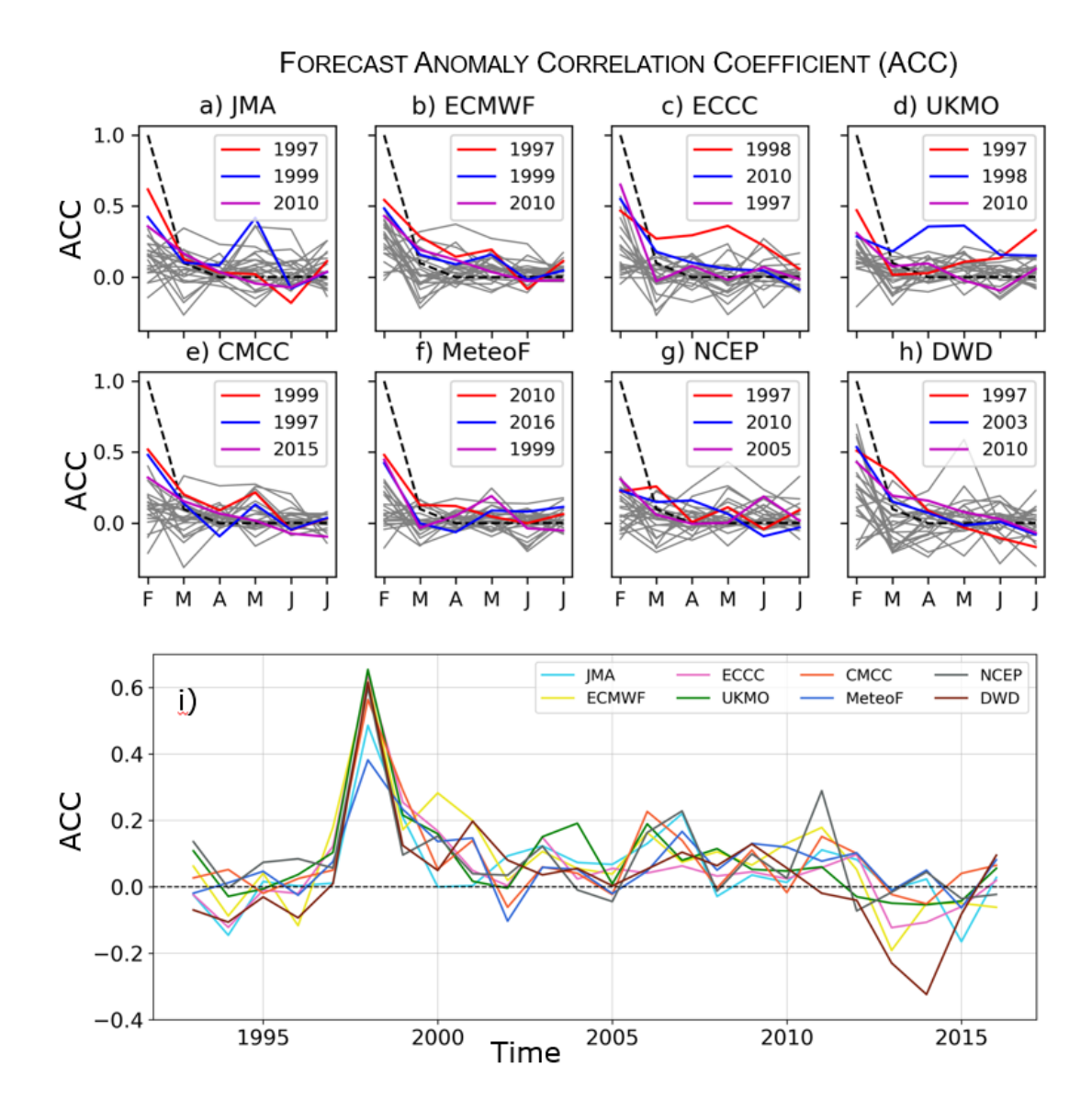


Figure 3.5 Anomaly correlation coefficient (ACC) between GPCP and each C3S model (a-h; shown in the upper panels) for monthly rainfall anomaly over part of Eastern Africa (blue dashed box of Fig. 1i) for each year (grey lines) from lead month 0 (February) to lead month 5 (February). In each subfigure, the top three forecasts stand out with distinct colours: the most accurate year is highlighted in red, the second-best in blue, and the third best in magenta. These forecasts are determined by sorting all predicted years based on their average ACC values across February and March The lower panel (i) illustrates the spatial correlation between each model and GPCP

rainfall anomalies for the MAM season, calculated over Equatorial Eastern Africa (30–50°E, 5°S-10°N)

3.5 Predictability conditional on ENSO and IOD phases

Large-scale climatic drivers, specifically SST anomalies in the Indian and Pacific Oceans, are the primary source of predictability for the East African long rains. Rainfall patterns in the region are significantly influenced by variability in the Pacific Ocean, such as ENSO, and the Indian Ocean. While El Niño or La Niña events frequently alter moisture transport and atmospheric circulation, positive or negative IOD phases can have a substantial impact on the timing and intensity of the long rains. To identify the main source of predictability for the east African long rain pattern, we have seen the association with IOD and ENSO seasonal variability (Palmer & Anderson, 1994; Troccoli, 2010).

The role of tropical SST in modulating East African long rain is analyzed, utilizing indices that monitor rainfall (i.e., EEARi) and SST (ENSO and IOD). Specifically, the Niño 3.4 index (N3.4; SST anomalies averaged over 120°W–170°W, 5°S–5°N) tracks ENSO, while the Dipole Mode Index (DMI; SST anomalies difference between the western Indian Ocean (DMIw), 50°E–70°E, 10°S–10°N, and eastern Indian Ocean (DMIe), 90–110°E, 10°S–0) monitors IOD variability (Saji et al., 1999). The relationship between MAM rainfall anomaly index and DMI across models (Fig. 3 .6a-h) and observational datasets indicates there is a negative relation between DMI and N34 phases. From our analysis, the MAM rainfall season has no clear association with SST when we consider N34 and DMI as evident from observations and models (Fig. 3.5). Even though MeteoF and NCEP models show a relatively high positive correlation between DMI and N34, there is no significant association with MAM rainfall anomaly.

However, when we considered SST over the western Indian Ocean (DMIw) and N34, most coupled models and observations present that SST has a linear association with MAM rainfall anomaly (green colors on Fig. 3.6), except the MeteoF model across the East African region. Some successful predicted year that we identified (Fig. 3.5) is associated with the strongest El Niño event on record (1997/1998), East Africa experienced the largest positive RFa during MAM season (Fig. 3.1 k). While most

models exhibited weak association between N34 and DMI, strong association presented in all models and observational dataset when we considered the western Indian Ocean (DMIw).

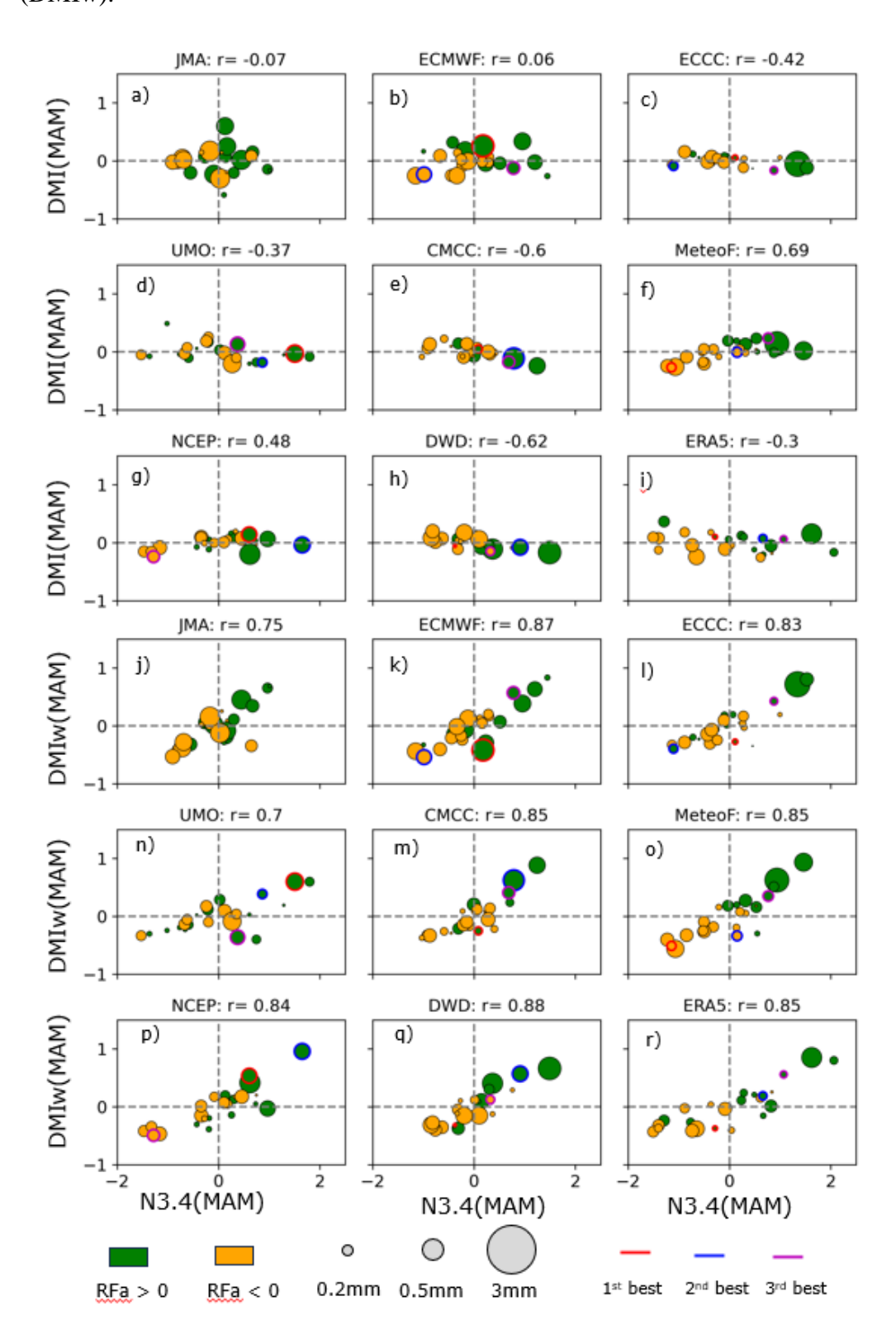


Figure 3.6 Scatterplot of Niño3.4 index (N34; x-axis) versus Dipole Mode Index (DMI; y-axis) during MAM season for each of the 24 years analyzed in both model predictions (a-h) and GPCP dataset (i). The area of the circle is proportional to the absolute value of MAM rainfall anomaly averaged over part of Eastern Africa (blue dashed box of Fig. 1i), with positive (negative) anomaly coloured in green (orange). As in Fig. 3, the best forecasted year is highlighted in red, the second-best in blue, and the third-best in magenta. Additionally, the correlation coefficient between N3.4 and DMI is provided at the top of each subfigure for reference. (j-r) shows a similar analysis but with the western pole of the DMI index (DMIw).

Given East Africa's proximity to the western pole of the Indian Ocean (DMIw region), the interannual variability of the East African long rains is more strongly linked to fluctuations in the Niño3.4 index, demonstrating higher predictability. Statistically, Niño3.4 and DMIw show more consistent SST-rainfall relationships across years during the MAM season. However, when considering the west-east dipole (DMI), the correlation between the long rains and SSTs is notably weaker than the correlation with DMIw. Similarly, the correlation between the long rains and SSTs is relatively a little bit stronger with El Nino Modoki (Fig. 3.7). Hence, these finding highlights that the East African long rains are more closely associated with ENSO than with the overall DMI, as supported by both observational data and model simulations (Fig. 3.6 j-r). The stronger correlation with DMIw, despite the expectation that local SST variations would play a more dominant role, underscores the significant influence of large-scale ocean-atmosphere interactions, such as ENSO, on East Africa's rainfall variability during the long rains.

CONNECTION WITH EL NIÑO MODOKI AND IOD PHASES

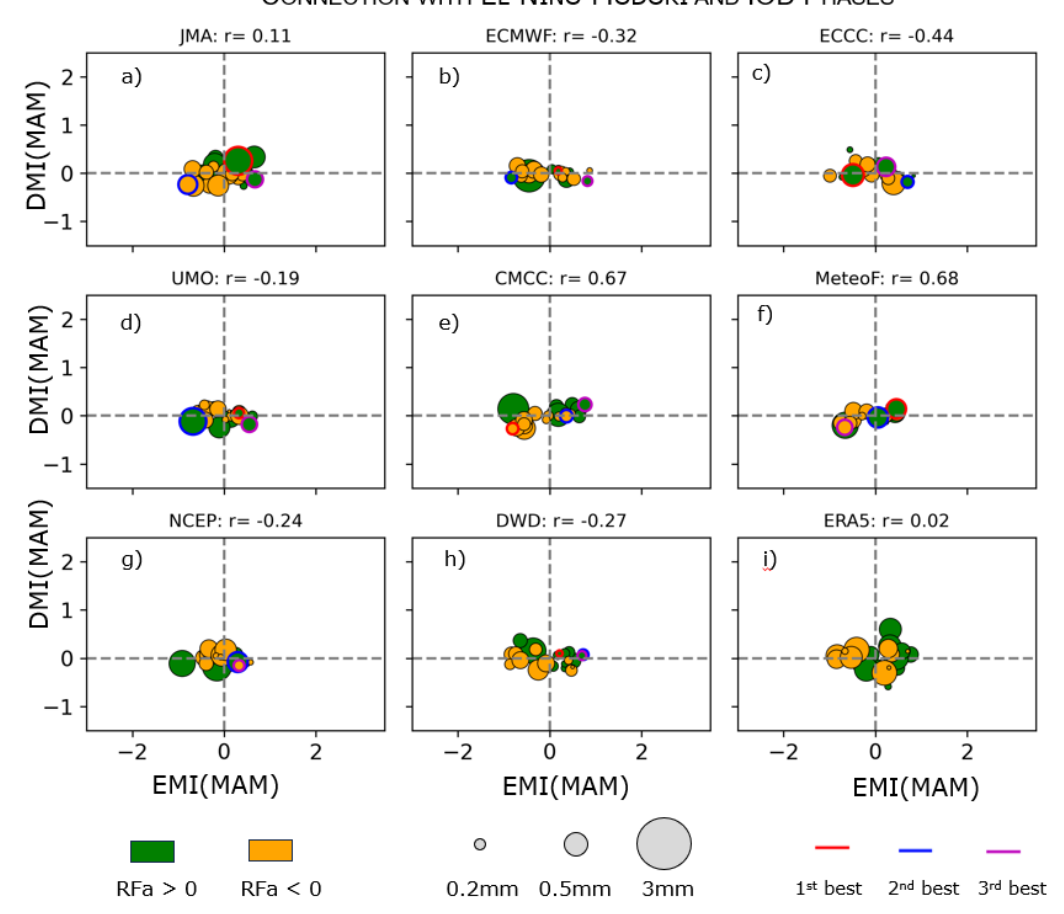


Figure 3.7 Scatterplot of El Niño Modoki index (EMI; x-axis) versus DMI (y-axis during MAM season for each of the 24 years analyzed in both model predictions (a-h) and GPCP dataset (i). The area of the circle is proportional to the absolute value of MAM rainfall anomaly averaged over part of Eastern Africa (blue dashed box of Fig. 2.1i), with positive (negative) anomaly coloured in green (orange). As in Fig. 3.5, the best forecasted year is highlighted in red, the second-best in blue, and the third-best in magenta.

The heatmap shown in Fig. 3.8 presents the correlation between MAM rainfall anomalies (RFa) and key climate indices—N34, DMI, slpDMI, EMI, and UEQ—across various dynamical models. Most models, along with ERA5 (0.41), show significant positive correlations with N34, reinforcing the strong influence of ENSO on MAM rainfall variability. While EMI (El Niño Modoki) shows a weak and inconsistent influence. DMI correlations are more mixed: while CMCC (0.62) and JMA (0.57) align

with observed patterns, others like UKMO (-0.46) and NCEP (-0.57) reveal opposite trends, highlighting model differences in representing IOD impacts.

Particularly, UEQ—zonal wind anomalies over equatorial Africa show strong and consistent negative correlations across most models (e.g., JMA: -0.82, CMCC: -0.83), emphasizing its key role in modulating moisture transport. Likewise, sea level pressure anomalies over the DMI region also exhibit significant negative correlations in models such as JMA (-0.74) and CMCC (-0.84), though these are generally weaker than for UEQ. In general, the CMCC and JMA stand out for capturing stronger and more consistent relationships across all indices. In contrast, models like ECCC and MeteoF show weaker signals, pointing to challenges in simulating the drivers of East African rainfall. While ENSO and UEQ remain the most robust predictors of rainfall variability, inconsistent DMI and slpDMI signals suggest a limited or model-dependent influence of IOD-related SST and pressure anomalies on the region's long rains.

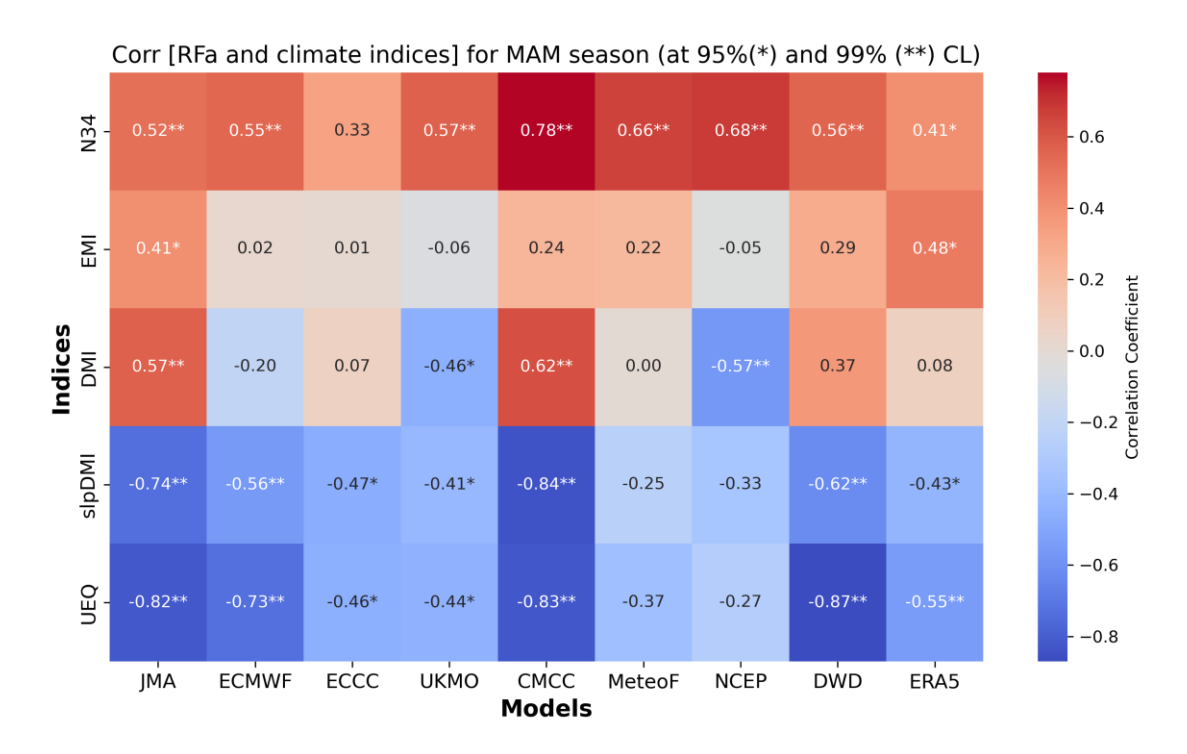


Figure 3.8 Correlation between RFa and climate indices for MAM season. Asterisks (*) and (**) indicate significance at the 95% and 99% confidence levels, respectively.

The interannual variability of SST, sea level pressures, and zonal wind anomaly for the MAM season is shown in, derived from multiple models and the ERA5 dataset

(black points shown in Fig. 3.9), providing insights into key climate drivers influencing East African long rains. Niño3.4 (N34) index, a key measure of ENSO variability, where all models exhibit strong agreement in capturing interannual fluctuations (Fig. 3 .9a). This high coherence between models and ERA5 underscores the robust predictability of ENSO during MAM. The result revealed that East African long rains are linked to El Niño events, with notable peaks during the 1997-98 and 2015-16 El Niño episodes. The SST indices over the Indian Ocean, that is DMI, generally, models capture its variability, the spread between models is wider compared to the N34 index, reflecting greater uncertainty in simulating IOD-related processes. Additionally, we also examine sea level pressure variability of DMI (i.e., slpDMI shown in Fig. 3.7d), which highlights pressure differences associated with IOD variability. While the model patterns align broadly with ERA5, disagreements are noticeable, especially during extreme events.

Equatorial zonal wind anomalies—east-west winds along the equator—play a crucial role in the advection of moist air from the Indian Ocean, significantly influencing regional moisture transport and atmospheric circulation. Among these, the UEQ index stands out as particularly important. While most models capture the general trends of wind anomaly in UEQ, some models present considerable variation. For example, in the year 2000, both ERA5 and most models (except for the ECCC model) show positive anomalies in sea level pressure (SLP) and zonal wind, despite the presence of a negative N34 anomaly (Fig. 3.7d and e). This suggests that during La Niña conditions, the cooling in the eastern and central Pacific enhances the descending branch of the Walker circulation, leading to higher SLP anomalies in those regions (Zhao and Cook, 2011; Williams and Funk, 2021).



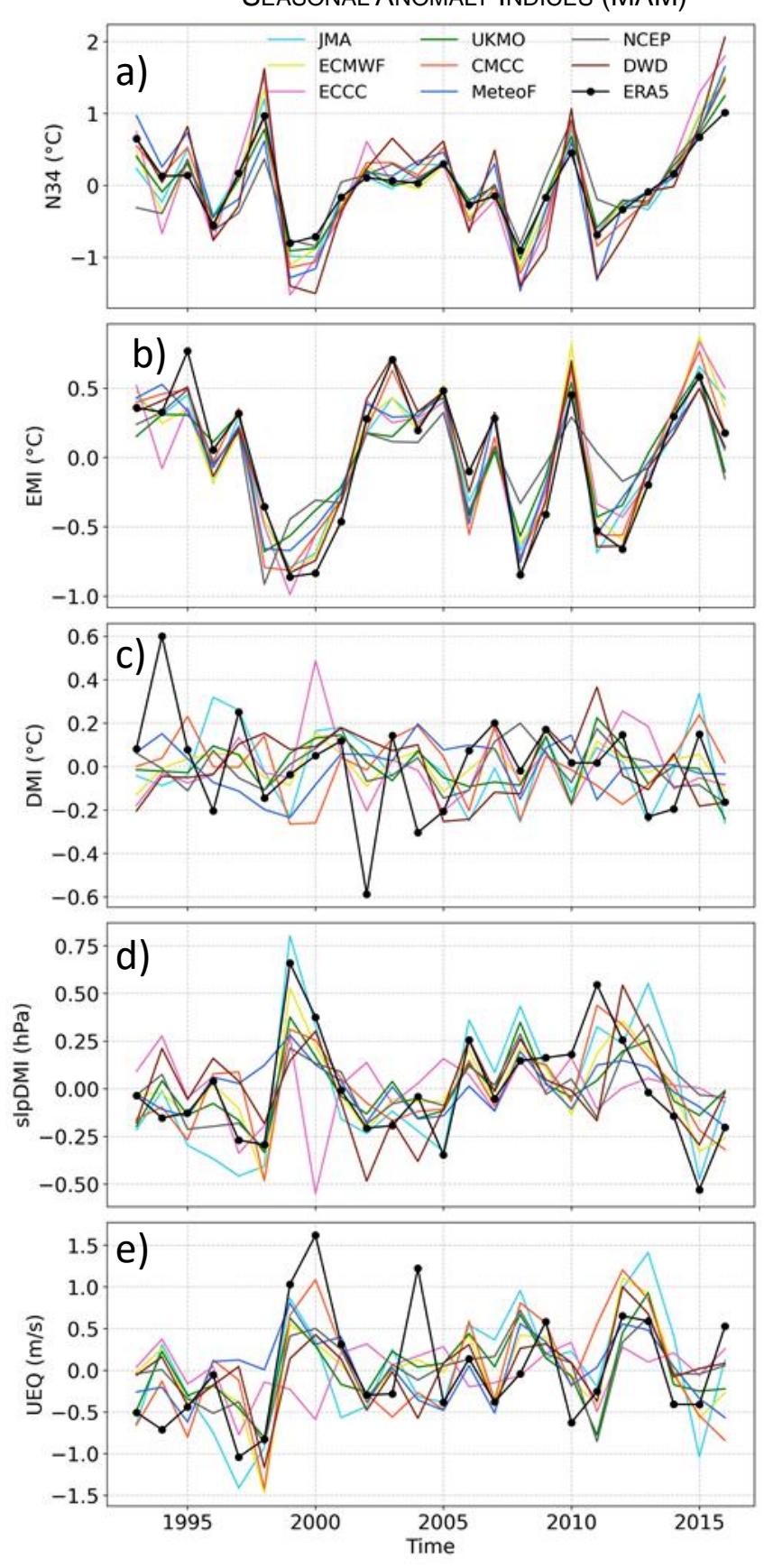


Figure 3.9 Interannual variation of MAM seasonal mean observed, individual coupled model's ensemble means anomalies a) N34(SST anomalies averaged over 120°W–170°W, 5°S–5°N) b) DMI, c) sea level pressure anomaly index over DMI region (slpDMI), d) Equatorial wind anomaly index (UEQ). The rainfall index is area-averaged over Eastern Africa (30–50°E, 5°S-10°N) for both models and ERA5.

3.6 Discussion and Conclusion

This chapter examined the performance of state-of-the-art dynamical seasonal prediction models in capturing the East African long rains, focusing on eight coupled models from the C3S seasonal retrospective forecast systems. We limited our analysis to forecasts initialized in February, which aligns with the onset of the long rainy season in most parts of East Africa.

Despite notable biases, particularly over the Congo Basin and the southwestern parts of the region (Fig. 3.1), most models demonstrated some skill in replicating rainfall anomalies over East Africa, especially in the southern sectors. However, model performance was limited over northern and western Africa. In some parts of the western Indian Ocean, predictive skill persisted through to MJJ seasons, as indicated by statistically significant correlations (Fig. 3.4). Rainfall predictability in the region is strongly linked to large-scale climate drivers, notably ENSO and IOD. The extended 1997–1998 El Niño, for example, led to the highest recorded rainfall anomaly in 1998, as evidenced by both observational datasets and dynamical models. Although the El Niño event peaked in late 1997, sustained ocean-atmosphere responses, such as a disrupted Walker Circulation, continued into early 1998, facilitating enhanced moisture transport into East Africa (Roy et al., 2024).

Our analysis shows that most models capture significant correlations between East African rainfall and the Niño3.4 index as well as the western Indian Ocean Dipole mode index (DMIw). Positive IOD events, marked by warmer SSTs in the western Indian Ocean, strengthen convection and increase moisture transport into East Africa, contributing to higher rainfall. Likewise, El Niño-related warming in the central and

eastern Pacific alters the Walker Circulation, enhancing moisture influx and increasing rainfall intensity in the region.

We evaluated the models' predictive skill up to three lead seasons (MAM to MJJ) by comparing their forecasts with GPCP observational data from 1993 to 2016. Models generally performed better during ENSO years than during IOD phases, underscoring the dominant influence of ENSO on the region's rainfall variability. While the models reliably reproduced Niño3.4 variability, they exhibited greater discrepancies when simulating the DMI and UEQ indices. This highlights the complexity of the coupled ocean-atmosphere processes in the Indian Ocean and their variable representation across models. Overall, the models demonstrate reasonable skill in forecasting East African long rains, particularly under strong ENSO conditions. However, their limited ability to simulate Indian Ocean dynamics suggests the need for further improvements in representing regional teleconnections and air-sea interactions.

4 INVESTIGATE THE ROLES OF ENSO AND IOD ON EAST AFRICAN SHORT RAIN USING EARTH SYSTEM MODEL EXPERIMENTS

4.1 Introduction

Remote teleconnections significantly influence East African rainfall variability, which leads to intra-seasonal to interannual fluctuations that are more noticeable than in many comparable locations across the world (Nicholls, 1997). Although factors like the Southern Annular Mode (Hendon et al., 2007), MJO (Kimani et al., 2020) and Atlantic Multi-decadal Oscillation (Xue et al., 2022) also play a role on rain fall variability, tropical drivers mainly ENSO (Indeje et al., 2000; Macleod & Caminade, 2019) and the IOD (Ashok & Yamagata, 2003; Behera et al., 2005; Saji N. et al., 1999) are recognized as the primary influences on interannual rainfall variability throughout East Africa (Pook and Gibson, 1999; Risbey et al., 2009). IOD often affects East Africa's rainfall, especially during the short rainy season, although the ENSO has a stronger effect throughout both the short and long wet seasons (Palmer et al., 2024). Despite these significant influences, the observable indices used to track ENSO and IOD often exhibit high levels of co-variability (Ashok & Yamagata, 2003), challenging efforts to isolate the individual contributions of each driver to rainfall anomalies (Liguori et al., 2022).

Recent studies argue that the frequent co-occurrence of ENSO and IOD phases makes it difficult to attribute observed East African rainfall patterns solely to one driver. To understand the independent role, it is important to distinguish the physical climate modes (ENSO and IOD) from the indices used to monitor their variability, such as the Niño3.4 index (N34; Trenberth, 1997) for Indian Ocean Dipole (Saji et al., 1999). To disentangle the individual contributions of climate drivers to the interannual variability of rainfall, some studies (e.g., Liguori et al., 2019) have employed both physical and statistical removal techniques. These methods enhance the accuracy of interpreting and attributing East Africa's complex rainfall variability. Analytical approaches have also been widely used to isolate the distinct influences of ENSO and the IOD on rainfall

variability (Liguori et al., 2022; McMonigal & Larson, 2022; Ummenhofer et al., 2009; Wang et al., 2019). Physical and statistical elimination approaches, such as regressionbased procedures and sensitivity experiments in climate models, have been used in research like Ligouri et al. (2022). By separating one mode's influence while accounting for the other, these methods make it possible to interpret each mode's effects more precisely. Studies such as Nicholson & Kim (1997) and Hastenrath et al. (2007) applied multiple regression and partial correlation analysis techniques to isolate the contribution of one mode, and the variability associated with the other mode is regressed out. For instance, by adjusting for Niño3.4 index values, ENSO-related fluctuation can be eliminated, enabling to evaluation of the IOD's remaining influence. To investigate atmospheric reactions to isolated causes, sensitivity experiments utilizing climate models are also frequently used. For example, simulations with SST anomalies limited to the Pacific or Indian Ocean are used (Luo et al., 2008; Tierney et al., 2013). Empirical orthogonal function analysis is another powerful tool to separate dominant modes of variability in climate datasets, distinguishing ENSO and IOD signals (Gupta et al., 2023) Advanced hybrid approaches, combining physical constraints with statistical techniques, such as the physical removal of SST patterns associated with one mode, have also proven effective (e.g., Ligouri et al., 2019)

The triggering mechanism for the IOD using model simulation with and without removal of the ENSO signal was realized by using only climatological wind stress (Fischer et al., 2005). They found that during non-ENSO events, anomalous Hadley circulation over eastern IO causes anomalous southeasterly wind over Java Island, leading to upwelling cold SST, and triggering of upwelling Kelvin wave via the easterly component of the southeasterly wind. Cooling on the east of the IO leads to losses of the climatological heating due to convection, thereby triggering an anticyclone southwest of the anomalous heat sink (Roy et al., 2023). Such an anticyclone intensifies the southeasterly wind, and the process continues. The second mechanism for triggering the IOD is the shift of the Walker circulation during the El Niño phase. El Niño weakens the Walker circulation by shifting the warm pool to the east, leading to losses of the climatological heating over the Maritime-Continental Rossby wave southwest of the

heating source. Such a mechanism occurred in 1997, the greatest El Niño year ever observed (Ashok & Yamagata, 2003)

Debates have arisen about whether the IOD is intrinsically linked to the ENSO or if it operates independently with its dynamics (Fischer et al., 2005; Luo et al., 2010; Saji et al., 1999). The interplay between these phenomena is evident, as developing El Niño events (or positive IOD phases) can induce positive IOD (or El Niño) conditions by triggering easterly (westerly) wind anomalies over the equatorial Indian (Pacific) Ocean through modifications to the Walker circulation (Behera et al., 2006; Luo et al., 2010; Wang et al., 2019; Zhang et al., 2019). However, Saji et al. (1999) found that a strong inverse relationship between the IOD and ENSO appears mostly in the fall season. Both statistical and physical methods were used to eliminate the ENSO signal from the Pacific Ocean. The IOD signal was physically isolated using a global climate model in which the measured SSTs over the Pacific Ocean were substituted with climatological SSTs. To physically isolate the IOD signal, the study employed a GCM using climatological SSTs in place of the observed SSTs over the Pacific Ocean. The results showed that while the IOD signal persisted after removing the ENSO signal, it exhibited weaker amplitude compared to the control run with raw SST data. This suggests that atmospheric forcing may play a primary role in driving the IOD. The statistical relationship between ENSO and IOD is investigated, with a focus on consistent event classifications based on Bjerknes feedback and index thresholds (Lestari & Koh, 2016). In this study, they found that the El Niño and positive IOD mutually enhance each other, but La Niña and positive IOD reduce each other's cooccurrence, demonstrating that co-occurrences are not coincider. On the other hand, there is minimal interaction between La Niña and negative IOD, and any historical coincidences are probably coincidental. Asymmetries in ENSO-IOD interactions and the different paths of El Niño and La Niña influences on the Indian Ocean are highlighted by these findings, which are corroborated by strong statistical tests and observable SST patterns (Cai et al., 2012; Xue et al., 2022).

The IOD is an internal coupled mode in the Indian Ocean, which at times cooccurs with the ENSO in the Pacific (Saji et al., 1999; Murtugudde et al., 2000). The relative influence of IOD and ENSO on East African short rains is not a surprise, as previous studies briefly studied (Behera and Yamagata, 2006; Luo and Yamagata, 2010). About 30% of positive IOD events co-occur with El Niño events (Rao et al., 2002). About 65% of strong IOD events occurred when there was no ENSO in the tropical Pacific. However, 35% of IOD-positive events co-exist with El Niño events, which can suggest possible interactions between the ENSO and the IOD. The coupling process between the Walker circulation associated with the El Niño autumn is a crucial factor in inducing the positive IOD (Ueda and Matsumoto, 2000). Further, Behera and Yamagata (2001) showed that IOD can modulate the Darwin pressure anomalies, thereby affecting the Southern Oscillation Index (SOI). Using long-term data, Ashok et al. (2001) found that the physical existence of the coupled mode states that the major contribution to the IOD comes from the Indian Ocean.

Saji et al. (1999) and Murtugudde et al. (2000) found that the intensity of the IOD and the equatorial zonal winds are strongly dependent on each other. Furtherly (Rao et al., 2002) confirmed that the zonal wind anomalies, the principal forcing for both the surface and subsurface dipoles, can bring the opposite polarity in SST anomalies and bring out the dynamical importance of these zonal winds in the development of dipole SST anomalies. Therefore, in this chapter, we assessed the role of tropical climate modes by isolating the ENSO signal from the Pacific through both statistical and physical methods. Statistical techniques, such as composite analysis and partial correlation, were used to investigate the influence of ENSO from other climate drivers, enabling us to understand its direct impact on East African rainfall variability. Physical approaches, including sensitivity experiments with CESM models, further add to this analysis by simulating atmospheric responses under prescribed SST anomalies associated with ENSO, thereby isolating its influence. we have also used similar techniques to isolate the influence of the IOD to investigate its independent role in causing rainfall variability during the short rainy season. Examining whether this variability is mainly driven by external climate forcings like volcanic eruptions and anthropogenic effects or by internal climate dynamics like the interaction between ENSO and IOD was a major emphasis.

4.2 Dataset, Model, and Methods

4.2.1 Observational data and CESM experiments

The observational SST and precipitation data are sourced from ERA5, a globally gridded monthly dataset with high spatial resolution, covering the period from 1958 to 2022. ERA5 provides detailed and accurate observations, making it ideal for climate analysis and model validation. In addition, monthly precipitation data are obtained from GPCP version 2.3, which combines satellite and gauge-based measurements to produce a consistent and reliable global precipitation record. These datasets are essential for evaluating the performance of climate models and understanding observed climate variability.

Data from the Community Earth System Model (CESM) low resolution (2.5°, 2.5°) from NCAR were used to investigate the effect of internal variability on East African short rain variability. we conducted a series of experiments using CESM, employing four configurations such as CESM_CTRL, CESM_amipFULL, CESM_noIOD, and CESM_noIOD. As indicated in table 4.1 summarizes details of CESM (Community Earth System Model) experiments designed to analyse climate variability and the influence of specific climate drivers (Hurrell et al., 2013). The CESM_CTRL simulation is a fully coupled control experiment that includes dynamic interactions between the ocean, atmosphere, sea ice, and land components, spanning the data period 400-2200. It serves as a baseline for comparison with other experiments. The CESM_amipFULL (Atmospheric Model Intercomparison Project) simulation, an atmospheric-only experiment, uses SST prescribed from CESM_CTRL to isolate atmospheric responses, covering the period 801-1000. The CESM_noIOD experiment suppresses variability related to the IOD, allowing for the examination of its role in rainfall variability. Similarly, the CESM_noENSO simulation eliminates ENSO variability to isolate its impact on global and regional precipitation and temperature patterns. Both the CESM_noIOD and CESM_noENSO experiments span the period 801-1000. All simulations are conducted at low resolution, with SST and precipitation as primary variables to investigate the individual and combined effects of oceanatmosphere processes on the East African short rain variability.

Table 4.1 Description of CESM model configuration applied for this study

Features	CESM_C TRL	CESM_A MIP	CESM_amipF ULL	CESM_noE NSO	CESM_noI OD
Configurat	Fully coupled model with atmosphere, ocean, land, and sea ice components.	Atmospheric model with prescribed observed SSTs climatology (12 months).	Atmospheric model with SSTs from CESM_CTRL.	Partially coupled i.e. excludes ENSO variability.	Partially coupled i.e. excludes IOD variability.
SST Source	Dynamically computed by the coupled ocean-atmosphere model.	Observations	From CESM_CTRL (internally generated SSTs).	Dynamically computed with ENSO signals removed.	Dynamically computed with IOD signals removed.
Ocean- Atmosphe re Coupling	Fully coupled.	No coupling (prescribed SSTs).	No coupling (prescribed SSTs).	Partially coupled except in the ENSO region	Partially coupled except in the Indian Ocean region
Purpose	Study natural variability and long-term trends in a fully coupled system.	Study the atmospheric response to observed SST variability.	Study the atmospheric response to CTRL SST variability.	Isolate climate impacts without ENSO variability.	Isolate climate impacts without IOD variability.

Variability Included	Full variability (e.g., ENSO, IOD).	Observed SST variability.	CESM-generated variability (e.g., ENSO, IOD).	All variability except ENSO.	All variability except variability driven by Indian Ocean SST.
Period covered	801-1000	801-1000	801-1000	801-1000	801-1000

4.2.2 Method of analysis

We analyse five experiments conducted under pre-industrial forcing: three partially coupled and two atmosphere-only runs. The coupled control run (CTRL-coupled) spans 2200 years, with the first 400 years discarded as spin-up. All other experiments cover 200 years, initialized from year 801 of the CTRL-coupled run. All model analyses are based on the 200 years from 801 to 1000. The partially coupled experiments include a full dynamical ocean, but they are run with the SSTs restored to the model monthly mean climatology of CTRL-coupled in specified regions following (Liguori & Di Lorenzo, 2019). Here, we consider two different restoring masks: the first covers a region in the eastern Pacific (180°W to the American coast, 20°S-N) to remove the SST imprint of ENSO variability (noENSO-coupled experiment), and the second covers a region in the Indian and west Pacific oceans (from the African coast to the maritime continent, 20°S to Asian coast) to remove the SST imprint of IOD variability (noIOD-coupled experiment). The CESM1 model and the mask used in the noENSOcoupled experiment have been employed in previous studies specifically designed to constrain ENSO variability (Deser et al., 2017). The mask for the noIOD-coupled experiment is based on recent studies using nudged-SST simulations with CESM1 to explore variability in the Indian Ocean (Zhang et al., 2019). While we adopt a similar Indian Ocean mask, we restrict its eastern boundary to the Maritime Continent to prevent direct influence on the Pacific Ocean, unlike the broader mask extending to the dateline (180°W).

a) Composite analysis

Composite analysis is a technique used to compare dry and wet situations, for example, to identify the circulation features particular to a particular combination of conditions. The key climate processes can then be explained by physical hypotheses derived from this (Boschat et al. 2016). In process-based climate model evaluation, the method can also be used to find common signals in the circulation of models that have biases in one way, such as wet vs dry models (Creese et al. 2019). Composite analysis is a statistical method commonly used in meteorology and climatology to identify and analyze patterns associated with specific phenomena, such as El Niño events or extreme weather conditions (Wilks, 2011). This approach involves segregating data into subsets based on a particular criterion (e.g., above or below a threshold) and averaging the subsets to highlight characteristic patterns. Mathematically, the composite for a variable X can be expressed as

$$Xcomposite = \frac{1}{N} \sum_{i=1}^{N} Xi$$
 (2)

Where *Xcomposite* is the composite mean; N is the number of events or cases considered in the composite, and Xi represents individual data points in the subset of the variable X for the ith event. By isolating features associated with specific conditions, composite analysis helps researchers understand the influence of key drivers on climatic variables

b) Partial correlation analysis

Partial correlation analysis is a statistical method used to quantify the strength and direction of the relationship between two variables while controlling for the effects of one or more additional variables (Behera et al., 2005). In the context of East African short rainfall anomalies, this method is particularly useful for isolating the independent contributions of ENSO and IOD. By holding one variable constant (e.g., ENSO), the partial correlation can reveal the specific influence of the other variable (e.g., IOD) on

rainfall anomalies. By using this method, we can distinguish between the associated effects of ENSO and IOD, which frequently co-occur and influence rainfall patterns over East Africa during the OND season. Partial correlation analysis results are useful in determining whether short rainfall anomalies are driven more by ENSO than IOD. For instance, studies have shown that during certain years, the IOD exerts a stronger influence on East African rainfall compared to ENSO, particularly when ENSO signals are weak (Behera et al., 2005). Conversely, during strong El Niño years, ENSO can overshadow the IOD's influence, highlighting the need to account for both drivers independently (Schreck & Semazzi, 2004). It is applied to measure the association of EASR with DMI and ENSO by removing one of these factors, calculated as follows:

$$r_{13,2} = \frac{r_{13} - r_{12} \cdot r_{23}}{\sqrt{(1 - r_{12}^2)} \sqrt{(1 - r_{23}^2)}}$$
 (3)

where r_{13} is a correlation between DMI and the rainfall anomaly index, r_{12} is the correlation between DMI and Niño 3.4 index, r_{23} Correlations between Niño 3.4 and rainfall anomaly index

4.3 Rainfall Climatology

The rainfall seasonal climatology for the OND season across East Africa is shown in Fig. 4.1, which compares different CESM model experiments with observational datasets (ERA5 and GPCP). The upper panel (Fig. 4.1a-f) displays the regional distribution of rainfall climatology for each dataset, while Fig. d) presents the seasonal precipitation cycle averaged over Equatorial East Africa is presented (shown in blue colour dotted line, Fig 4.1.1a). Both the observational data set and model output exhibit a bimodal precipitation pattern, peaking during the long rains (MAM) and short rains (OND). While the models capture the general seasonal cycle, discrepancies are evident, particularly in the magnitude of rainfall tends to underestimate rainfall during March and April. Whereas CESM_noIOD and CESM_noENSO exhibit closer alignment with observations during February through April, which is part of the long rainy season. In comparison to observational data, the seasonal rainfall cycle over equatorial East Africa is generally captured by the CESM model simulations (Fig. 4.1),

which exhibit consistent patterns but differ in intensity. During the OND season, CESM_CTRL and CESM_amipFULL closely reproduce the observed peaks, showing strong alignment with each other. However, these models overestimated the OND rainfall pattern in contrast to the GPCP and ERA5 datasets. The seasonal cycle is accurately replicated by CESM overall, however, its overestimation during the OND season needs further research.

The seasonal climatology, the ERA5 (Fig. 4 .1a) dataset represents the observational data, showing a pronounced rainfall maximum over the central parts of the analysed region, particularly in the Congo basin far from the coast. The CESM_AMIP (Fig. 4 .1d) model, which uses a prescribed SST pattern, simulates weaker rainfall, indicating reduced sensitivity to tropical climate modes. On the other hand, the CESM_noENSO (Fig. 4 .1e) and CESM_noIOD (Fig. 4 .1f) models present the rainfall maxima are slightly weaker and spatial gradients less pronounced than in ERA5. The CESM_noENSO model (Fig. 4.1 e) shows a notable reduction in rainfall over the region, suggesting the model has a notable systematic bias in rainfall patterns.

RAINFALL CLIMATOLOGY (OND) a) ERA5 b) CESM CTRL c) CESM_amipFULL 15°N 10°N 12 5°N 0° 10 5°S 8 d) CESM_AMIP e) CESM_noENSO f) CESM_noIOD 6 15°N 4 10°N 5°N 2 0° 5°S mm25°E 35°E 25°E 35°E 45°E day g) Precipitation Seasonal Cycle Over Equitorial East Afrcia ERA5 GPCP CESM_CTRL CESM_amipFULL CESM AMIP CESM_noENSO mmCESM noIOD day 2 1 M M À Ś Ó Ď Α Ν Month

Figure 4.1 Seasonal OND rainfall climatology for ERA5 (a), model (b-f) and seasonal cycle of monthly rainfall (g) averaged over Equatorial East Africa region (30–50°E, 5°S-10°N) for observational dataset (dotted line) and CESM coupled models averaged over available years (801-1000), GPCP (1979 to present), and ERA5 (1958-2022).

There is interannual variability in the rainfall anomalies across all model experiments, with variations in the frequency and magnitude of events. A wider range of anomalies is produced by the complex interactions between ENSO and IOD, which are reflected in the CESM_CTRL simulation (Fully coupled control Run). Eliminating ENSO or IOD lowers this fluctuation, demonstrating their crucial influence on East African

rainfall. The models with the highest variability, CESM_CTRL and CESM_amipFULL, have standard deviations of 0.82 and 0.83 mm/day, respectively (Fig. 4.2 .2a and b). This suggests that the combined effects of ENSO and IOD continue to influence these models' natural variability.

The standard deviation of CESM_noENSO, on the other hand, is smaller at 0.69 mm/day, indicating less fluctuation because of the elimination of ENSO-related impacts (Fig. 4.2c). Whereas CESM noIOD with a standard deviation of 0.45 mm/day, exhibits the most variability since the elimination of IOD further reduces seasonal variations in rainfall (Fig 4.2 d). These findings demonstrate the distinct roles that ENSO and IOD play in the region's rainfall variability. While the lower variability in CESM_noENSO and CESM_noIOD indicates the lowered influence when these important climate causes are omitted, the larger variability in CESM_amipFULL highlights the important role of atmospheric variables in regulating East African rainfall. Even though CESM_amipFULL and CESM_CTRL depict almost similar patterns and variability, in CESM_CTRL (coupled model), ocean dynamics can dampen atmospheric variability through feedback mechanisms such as thermocline adjustments or changes in ocean heat content, which act as a buffer. On the other hand, CESM_amipFULL relies solely on prescribed SSTs without such feedback, allowing atmospheric processes (e.g., convection and moisture transport) to respond more freely to the imposed SST anomalies, leading to slightly higher variability.

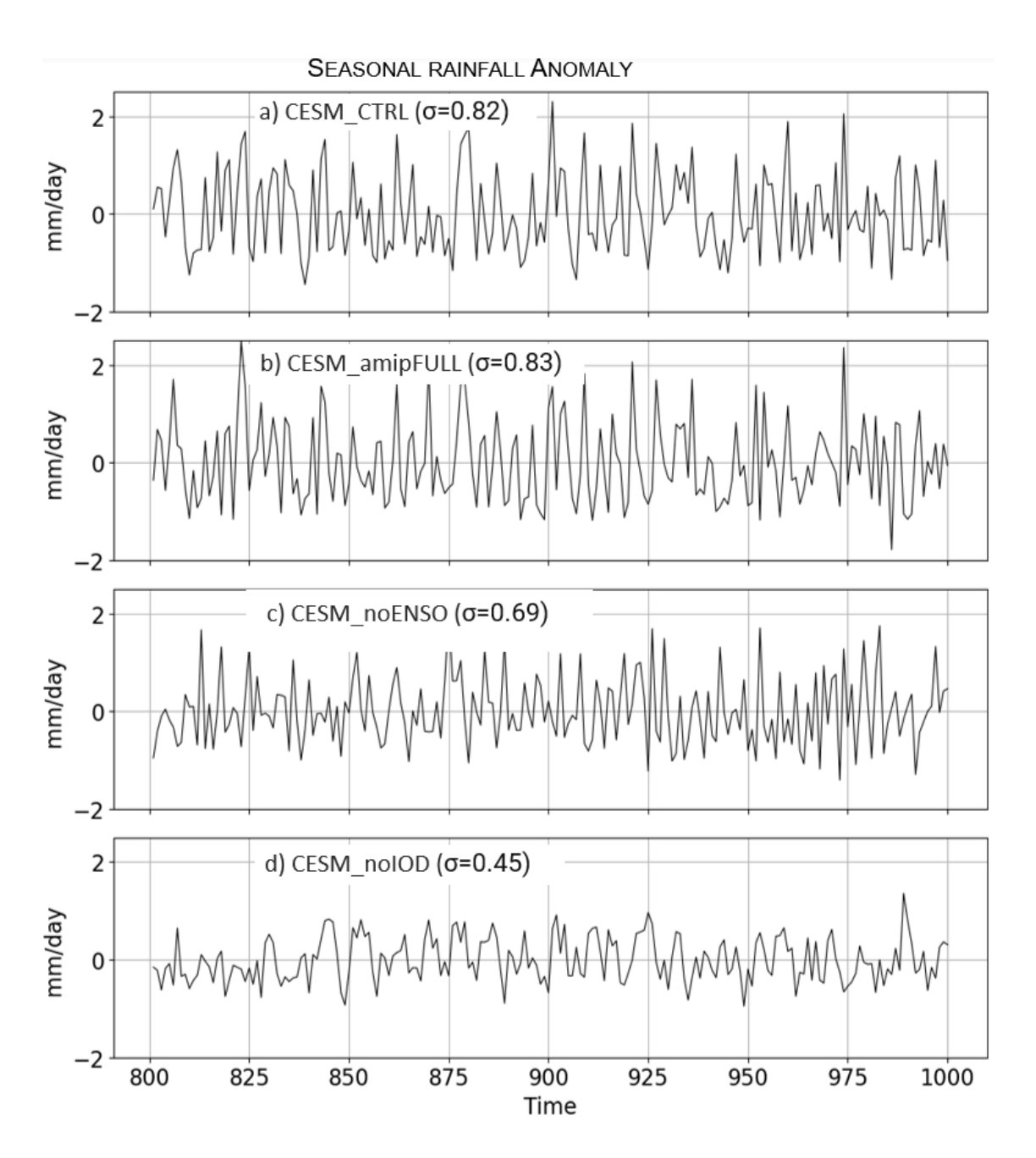


Figure 4.2 Seasonal OND rainfall anomalies over East Africa derived from CESM experiments for the period 800–1000. The anomaly calculated over Equatorial Eastern Africa (30–50°E, 5°S-10°N)

4.4 Rainfall variability

Model bias describes the differences between the model's simulations and observational data that can be attributed to the model's assumptions, parameterizations, or structural constraints. The mean bias in rainfall anomalies between CESM model

simulations and ERA5 over EA (Fig 4.3). The control simulation (CESM_CTRL; Fig 4.1a) displays both positive and negative biases in typical areas of the region. There is a noticeable negative bias close to 3°S, especially west of Lake Victoria, which suggests that rainfall in this region is significantly underestimated. On the other hand, some portion of western Indian and Western Ethiopia have moderate positive biases, indicating an overestimation of precipitation. While it captures the general structure of East African rainfall (Fig 4.1 b) noticeable differences arise in magnitude and spatial distribution compared to ERA5. These biases point to difficulties in accurately modelling localized rainfall mechanisms across intricate terrains. As presented in control experiment, similar rainfall biases are detected in the CESM amipFULL simulation (Fig 4.3 b), which accounts for observed SST forcing, though with somewhat smaller magnitudes. The positive biases in the eastern parts of the analysed region seem less severe and more dispersed, but the negative bias close to 3°S is still noticeable. This suggests that while adding observed SST forcing enhances the rainfall simulation to some extent, it does not completely remove the systemic biases.

The spatial patterns in CESM_AMIP experiments (Fig 4.3c), where the models are only influenced by observed SSTs, are unchanged; however, positive biases become slightly noticeable near equator and western Ethiopia which is far from East African coast. This indicates that while SST forcing somewhat captures regional variability, it has trouble fully resolving local precipitation processes. The recurrence of biases calls attention to shortcomings in the model's depiction of land-atmosphere feedback and convection, particularly in the vicinity of Lake Victoria. Here we can say that CESM_AMIP simulations, which use observed SSTs as forcing, display relatively higher positive biases over the southwest portion of the Indian Ocean compared to CESM_CTRL and CESM_amipFULL. The better agreement with ERA5 highlights the significant role of realistic SST forcing in rainfall biases.

The bias patterns in the CESM_noENSO experiment (Fig. 4.3d) are qualitatively like the control simulation, even if ENSO variability is eliminated. There is still a significant negative bias close to 3°S, as well as numerous smaller positive biases in other areas. This suggests that ENSO does not significantly influence the mean rainfall biases in this area. Similarly, CESM_noIOD exhibits bias patterns that are

nearly identical to CESM_CTRL when the Indian Ocean Dipole (IOD) is removed (Fig. 4.3e). Biases in both ENSO and IOD exclusion runs are persistent, indicating that their influence on the mean rainfall bias in the study area is minimal. Regionally, dry bias anomalies are especially evident across Kenya and some portions of the southern Congo Basin, suggesting that precipitation in these regions is slightly underestimated. On the other hand, orographic areas like the Bale Mountains in Ethiopia and the Mitumba Mountains in Uganda exhibit wet bias anomalies.

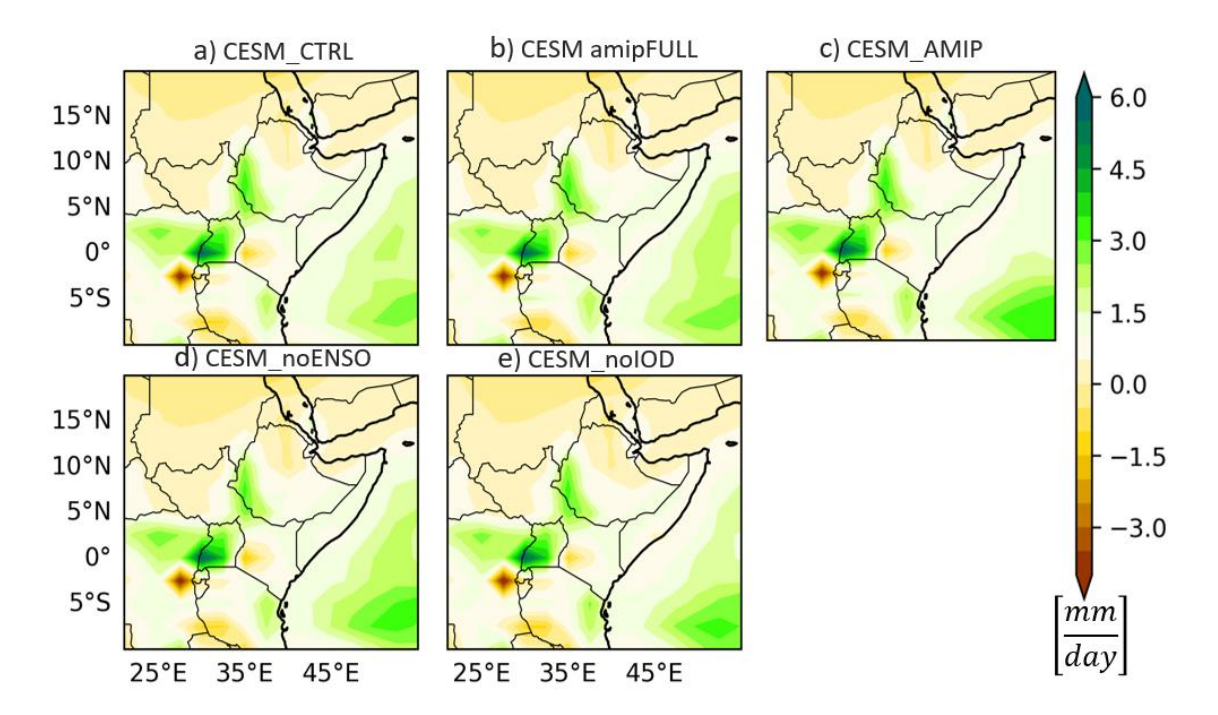


Figure 4.3 Seasonal OND rainfall bias (a-e) for CESM coupled models. The mean bias is computed as the difference between each model (CESM_CTRL and CESM_amipFULL (801-1000), CESM_AMIP (400-2200), and the observational dataset ERA5(1958-2022)

4.5 Characterization of ENSO and IOD

To characterize ENSO and IOD, we applied the Dipole Mode Index (DMI), which represents the gradient of SST anomalies between the eastern and western equatorial Indian Oceans, to identify anomalous years for the IOD. To identify between strong ENSO and IOD years, thresholds based on standard deviations, a commonly used technique in climate research, were used (Saji et al., 1999). Positive or negative

IOD anomalous years are identified as SST anomalies with a DMI greater than ± 0.5 standard deviations (Saji et al., 1999). When the Niño 3.4 index exceeds ± 0.7 standard deviation, events are classified as El Niño (positive ENSO) or La Niña (negative ENSO). La Niña events (negative ENSO) are characterized by Niño 3.4 values below -0.7, whereas El Niño events (positive ENSO) are identified when the Niño 3.4 index exceeds +0.7 standard deviation (Trenberth, 1997).

In the observations (4.4a), during only ENSO (positive) years (top-left), strong warming occurs over the equatorial Pacific Ocean, consistent with the typical El Niño pattern, while the Indian Ocean shows minimal anomalies. In contrast, during only IOD (positive) years (top-centre), there is a clear dipole pattern over the Indian Ocean: positive anomalies (warming) in the western basin and negative anomalies (cooling) in the eastern basin. During the co-occurrence of IOD (positive) and El Niño (top-right), the warming in the Pacific associated with El Niño dominates, and the Indian Ocean exhibits a strong dipole pattern. For the combined scenarios (bottom row), all ENSO (positive) and all IOD+ENSO (positive) reveal more widespread warming across the Pacific and Indian Oceans, indicating the superimposed effects of ENSO and IOD.

The CESM CTRL model (4.4 b) captures similar spatial patterns to observations but with notable differences. During only ENSO (positive) years (top-left), the equatorial Pacific exhibits strong warming resembling El Niño, although the magnitude and spatial extent appear slightly weaker compared to observations. During only IOD (positive) years (top-center), the Indian Ocean dipole pattern is evident, but the cooling in the eastern basin appears less pronounced than in observations. Pure IOD and ENSO (positive) years (top-right), the Pacific warming is prominent, and the IOD signature remains visible in the Indian Ocean. In all ENSO (positive) and all IOD (positive) scenarios (bottom row), the CESM CTRL model reproduces the broad Pacific warming and Indian Ocean dipole features reasonably well, while biases are evident compared to observations.

In the case of CESM amipFULL simulations (4.4 c), the SST anomalies are prescribed in the model's boundary conditions, particularly from the control experiment SSTs. Therefore, the patterns closely resemble those in the CESM CTRL but with some

differences due to atmospheric dynamics. Thus, during only ENSO (positive) years (top-left), the equatorial Pacific warming remains dominant, consistent with El Niño, while during only IOD(+ve) years (top-center), the dipole pattern in the Indian Ocean is apparent, but slightly weaker than in observations. The only IOD+ENSO (positive) years (top-right) display combined Pacific warming and Indian Ocean dipole anomalies like the CTRL experiment. The all ENSO (positive) and all IOD+ENSO (positive) panels (bottom row) exhibit broader and more consistent SST warming patterns across the Pacific, with notable dipole features in the Indian Ocean, reflecting the combined influence of ENSO and IOD.

Comparing with Observational data, the CESM experiments (CESM_CTRL and CESM_amipFULL) capture the general SST anomaly patterns during ENSO and IOD years, such as Pacific warming during El Niño and the dipole signature in the Indian Ocean. However, the models tend to underestimate the magnitude and spatial extent of anomalies, particularly in the Indian Ocean during only IOD (positive) years. In all datasets, ENSO appears to exert a stronger influence on SST anomalies globally, especially in the Pacific Ocean. The co-occurrence of IOD with ENSO amplifies warming patterns in the Indian Ocean. The CESM_CTRL fully coupled model and CESM amipFULL atmospheric-only model show similar SST patterns, but differences arise due to coupling in control which allows the ocean-atmosphere feedback processes to evolve dynamically. In contrast, CESM amipFULL uses prescribed SSTs, limiting internal variability. This analysis highlights the ability of CESM models to reproduce observed SST anomalies during ENSO and IOD years while revealing areas for improvement, particularly in representing the Indian Ocean dipole magnitude and its independent role.

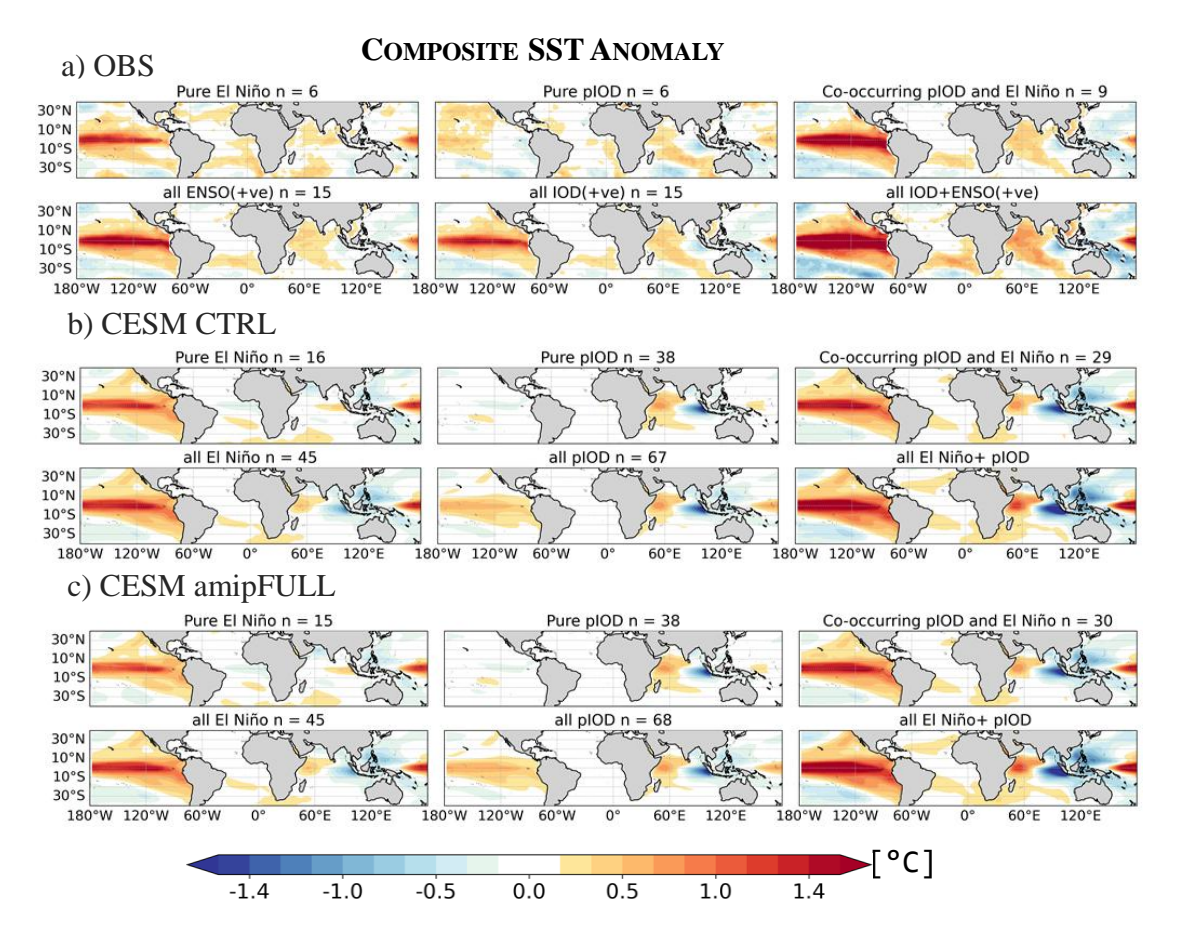


Figure 4.4 Composite SST anomaly over tropics for the OND season from observational data (ERA5) and the CESM model experiment. The anomalies are computed for climatological periods for ERA5 (1958-2022), and models (801 –1000) when only IOD occurs (first column panels), only El Niño occurs (second column panels), and both IOD and ENSO occur together (the third column panels).

CESM_noIOD experiments

In the case of the noIOD experiment, the composite SST anomalies over the tropical region during the OND season are presented in Fig. 4.5. Here, we compare the two scenarios: (1) years with only ENSO-positive events (n = 23) and (2) all ENSO-positive years (n = 57). In the case of only ENSO-positive, the SST anomalies reveal a strong warming signal presented in the central and eastern Pacific, characteristic of El Niño conditions, while minimal anomalies are observed in other regions, particularly the Indian Ocean. In contrast, the case of all ENSO-positive shows a broader warming

pattern that suggests additional contributions, possibly from residual IOD influences, despite the noENSO experimental setup.

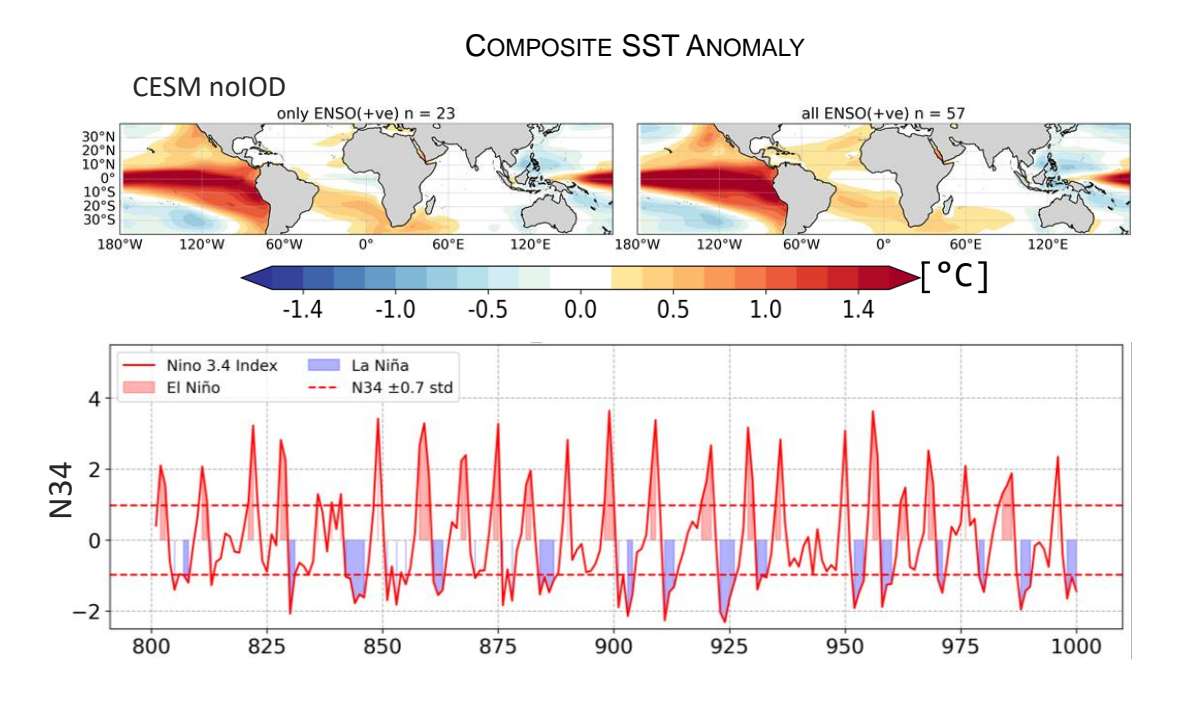


Figure 4.5 Composite SST anomaly over Tropics for OND season from CESM noENSO experiment.

CESM_noENSO experiments

We also investigate the composite SST anomalies during the OND season from the CESM noENSO experiment (Fig. 4.6), highlighting the role of IOD as tracked by DMI (the bottom panel). The anomalies are computed for climatological periods CESM noENSO (0801 -1000) when only IOD occurs (first column panel), and only El Niño occurs (second column panel). Therefore, we identified anomalies for years with only positive IOD events (n = 45) and all positive IOD years (n = 64). In years with only positive IOD events, the SST anomaly pattern reveals a strong west-east gradient in the Indian Ocean, with normal conditions in the western equatorial region and the eastern equatorial Pacific.

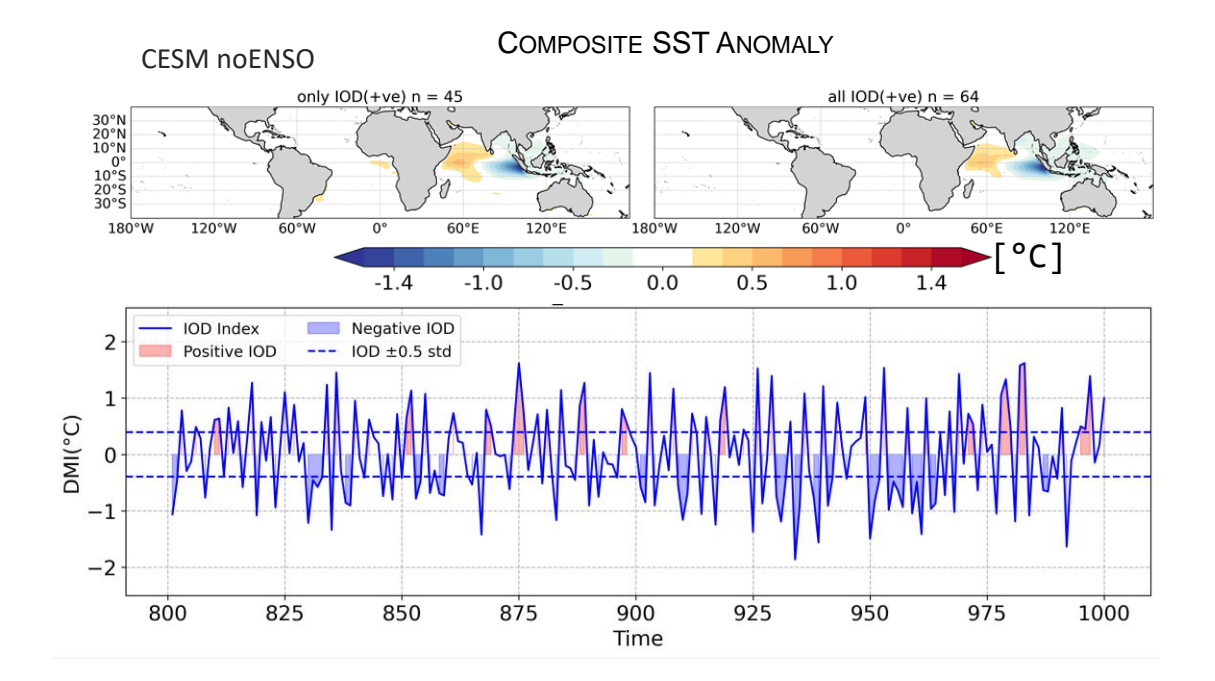


Figure 4.6 Composite SST anomaly for the OND season from the CESM noENSO experiment. The DMI index computed the difference between the West and East Indian Ocean model experiments.

4.6 IOD and ENSO Driven East African Short Rain Variability

IOD and ENSO are the major factors influencing East African rainfall variability during the OND season through SST-induced changes to convection and the large-scale atmospheric circulation; the region's rainfall variability can be influenced independently or in combination. The intricate interaction of ENSO and IOD influences the variability of EASR. Here, as shown in Fig. 4.7, we examine the association of EASRi with DMI (right column denoted in red) and Niño3.4 (left column, denoted in blue). As a result, EASRi shows a moderately positive association with Niño3.4 (r = 0.57) for the ERA5 dataset, but a greater correlation with DMI (r = 0.79), indicating the IOD's dominant role in influencing rainfall patterns. The connection with Niño3.4 is relatively weaker in the CESM tests (CESM_CTRL: r=0.28, CESM_amipFULL: r=0.23). In contrast, the DMI consistently demonstrates strong correlations in these tests (r=0.81 and r=0.83, respectively), indicating the dominant influence of the IOD on East African short rains in these simulations.

The independent influence of the IOD and ENSO on EASR is further proven by the noENSO and noIOD experiments (Fig. 4.5 and 4.6). The results demonstrate that, during the OND season, the IOD has a greater influence on regulating East African rainfall, whereas ENSO has a smaller and secondary effect. The case of the noIOD experiment has depicted that a negative correlation exists between N34 and EASRi (r = -0.53), suggesting that ENSO alone is not responsible for favourable rainfall anomalies. In contrast, the noENSO experiment keeps a strong link between DMI and EASRi (r = 0.83), confirming the robust and independent influence of the IOD. Therefore, these results prove that the IOD plays a dominant role in controlling East African short rains during OND, particularly in CESM simulations. The robustness of the IOD's impact is confirmed by the high correlations between the DMI and the East African short rains as presented in both observations and CESM simulations. The IOD continues to impact even when ENSO variability is reduced, highlighting its independent role in triggering rainfall anomalies. On the other hand, the negative correlation presented noIOD experiment indicates that ENSO by itself is unable to generate good rainfall conditions.

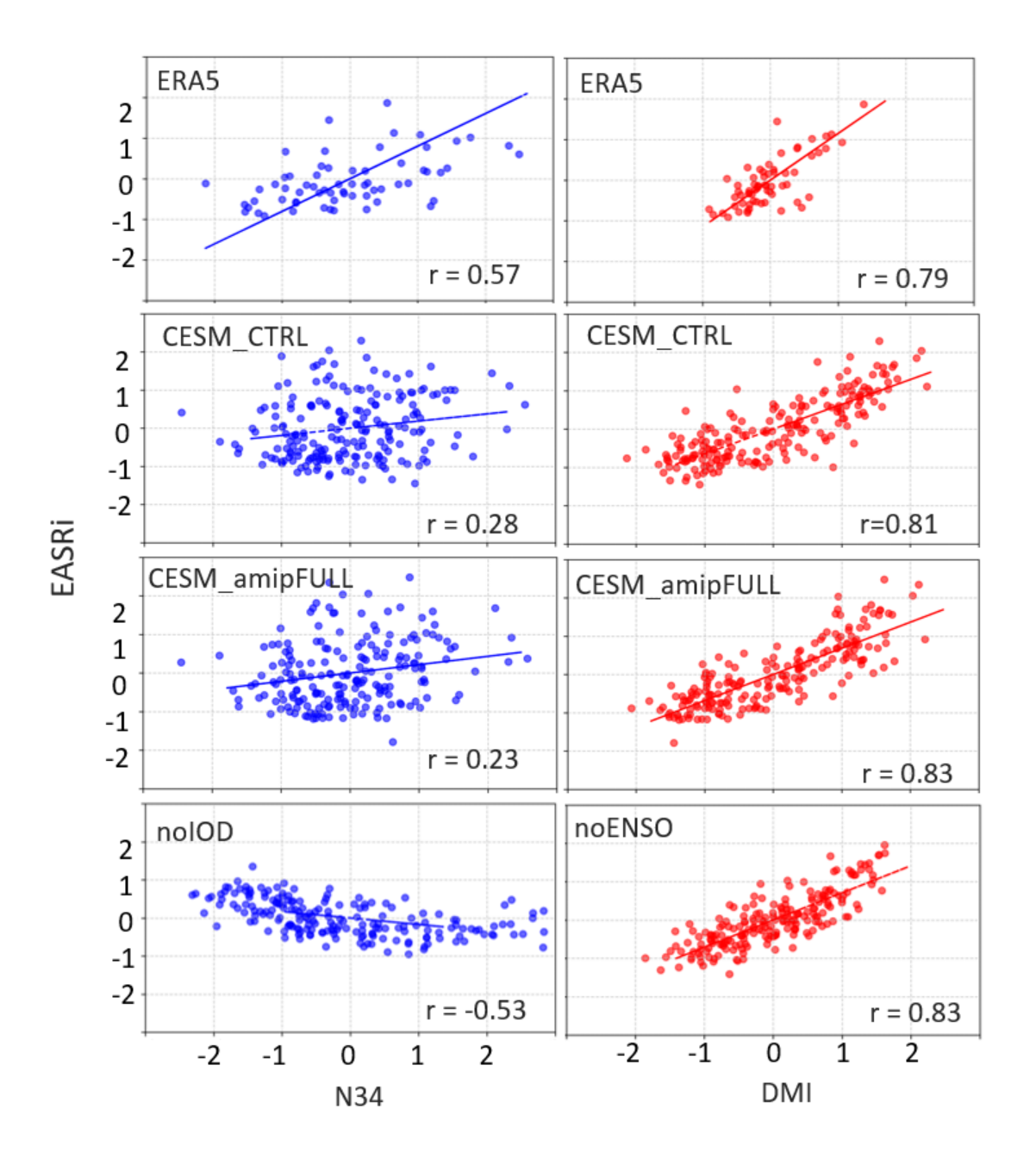


Figure 4.7 Scatterplot of East African short rain index (EASRi) versus N34 (first column indicated in blues colour), and IOD (the second column indicated in red colour) during the OND season for ERA5 reanalysis, CESM experiments. The solid line indicates the linear regression line.

4.6.1 Positive phases

Composite rainfall anomalies are computed for years with significant anomalies during IOD and ENSO events. During IOD phases, anomalous years are selected when

the DMI index exceeds 0.5 standard deviations (std), showing significant positive or negative IOD phases. Similarly, for ENSO, seasonal composite rainfall anomalies are calculated during El Niño years when the Niño3.4 (N34) index exceeds 0.7 standard deviations. These thresholds help identify the years with strong SST anomalies, allowing for a clearer understanding of how these phenomena influence seasonal rainfall patterns over East Africa. We examined the composite rainfall anomalies over East Africa during OND season using three IOD/ENSO phases (Fig.4.8): positive ENSO only(left), positive IOD only (center), and Joint IOD and ENSO positive phases (right column; identified as sorting common years that co-exist both ENSO and IOD). The variation in sample sizes (n) for each phase indicates the frequency of IOD/ENSO events. During positive ENSO phases, CESM_CTRL and CESM_amipFULL exhibit stronger and more localized dry anomalies, especially over central and northern regions, while the observational data present similar but weak rainfall anomalies with slight drying over East Africa.

For the positive IOD phase, all datasets reveal extensive wet anomalies over East Africa, confirming the main role of the IOD on rainfall variability. This effect is well captured by the CESM_CTRL and CESM_amipFULL simulations, which show intensified wet anomalies. The rainfall anomalies increased during the combined positive ENSO and IOD phases, with all datasets displaying significantly wet conditions throughout East Africa. While CESM_CTRL and CESM_amipFULL exhibit more pronounced wet anomalies, especially in the southern and central regions. Therefore, from Fig. 4.8, we can understand that the spatial patterns and magnitude of rainfall anomalies underscore the obvious role of the IOD, both individually and in combination with ENSO, in modulating East African OND rainfall. While CESM simulations align reasonably well with ERA5, they tend to overestimate rainfall responses, particularly during the combined phase.

COMPOSITE RF ANOMALY(OND)

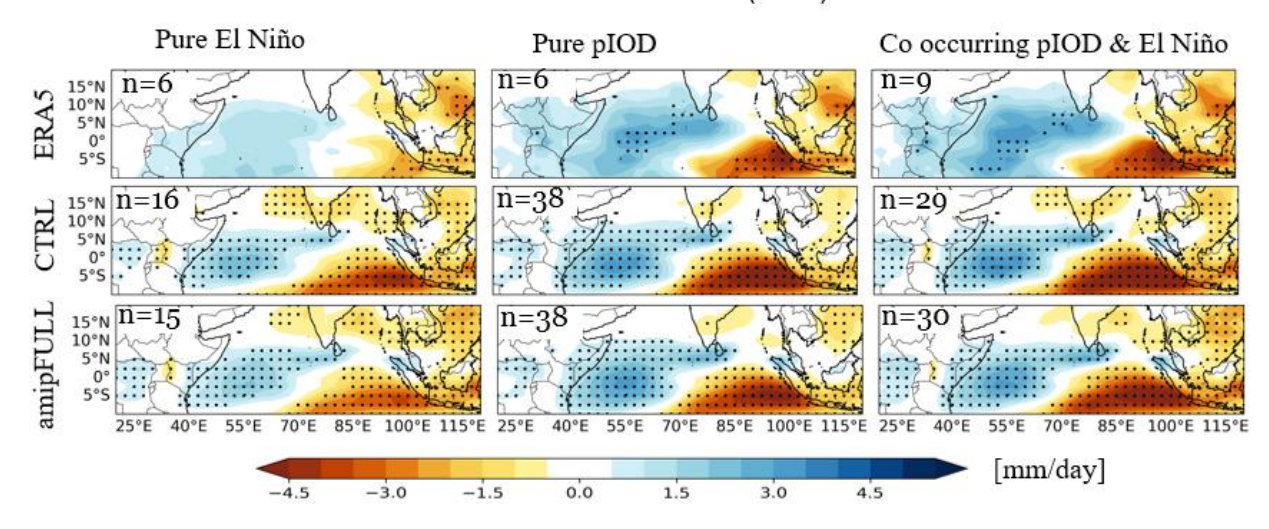


Figure 4.8 Composite rainfall anomaly over East Africa region for OND season from observational data (ERA5) and CESM model experiment during positive phase of ENSO/IOD. The anomalies are computed for climatological periods (ERA5 1958-2022) and models (0801–1000) when pure positive IOD (pIOD) occurs (first column panels), pure El Niño occurs (second column panels), and co-occurring of pIOD and El Niño (the third column panels). The sample size(n) is the number of events that exceed the threshold standard deviation of SST anomaly indices. The Stippling indicates significant composite anomalies (p < 0.05) relative to neutral years.

4.6.2 Negative phase

We also looked at the composite rainfall anomalies of the OND season during negative IOD/ENSO phases (Fig.4.9): Pure La Niña only(left), negative IOD (nIOD) and co-occurring of nIOD and La Niña (right column; identified as sorting common years that co-exist). The variation in sample sizes (n) for each phase indicates the frequency of nIOD/ La Niña events. During La Niña phases, CESM_CTRL and CESM_amipFULL exhibit localized wet anomalies, especially over central and northern regions, similarly, the observational data set presents similar but wet rainfall anomalies over land and some parts of the western Indian Ocean. Whereas during the negative IOD phase, all datasets reveal extensive dry anomalies over East Africa as expected, confirming the main role of IOD on rainfall variability. This effect is well captured by the CESM_CTRL and CESM_amipFULL simulations, which show

increased dry anomalies. The rainfall anomalies are significantly reduced during the combined negative ENSO and IOD phases, with all datasets displaying significantly dry conditions throughout East Africa. While CESM_CTRL and CESM_amipFULL exhibit more pronounced negative anomalies, especially over the ocean part. In general, we can understand that the spatial patterns and magnitude of rainfall anomalies underscore the obvious role of the IOD, both individually and in combination with ENSO, in modulating East African OND rainfall.

COMPOSITE RF ANOMALY(OND) Pure La Niña Pure nIOD Co occurring nIOD & La Niña 15°N 10°N 5°N n n=10 n=11 _{15°N} n=15 n=44 5°N 55°E 70°E 40°E [mm/day] 0.0 -3.0 -1.5 1.5 3.0

Figure 4.9 Composite rainfall anomaly over East Africa region for OND season from observational data (ERA5) and CESM model experiment during negative phase of ENSO/IOD. The anomalies are computed with respect to climatological periods (ERA5 1958-2022) and models (0801 -1000) when pure negative IOD (nIOD) occurs (first column panels), pure La Niña (second column panels) and co-occurring nIOD and La Niña occur together (the third column panels). The sample size(n) which numbers of events that exceeds threshold standard deviation of SST anomaly indices. The Stippling indicates significant composite anomalies (p < 0.05) relative to neutral years.

4.6.3 Independent roles of ENSO and IOD

To understand the independent roles of IOD and ENSO, two CESM experiments (CESM noIOD and noENSO) are applied. By isolating the effects of each event, these models enable identify the roles to rainfall variability. Therefore, we have tested for both positive and negative phases of IOD and ENSO (shown in Fig 4.10).

During the positive phase, the CESM_noIOD experiment (left column) presents significant negative rainfall anomalies over central parts of the East Africa region. Hence, ENSO plays a part in lowering rainfall when ENSO is removed. In the case of the CESM_noENSO experiment we noticed primarily above normal rainfall, especially in the coast and southwestern parts of the Indian ocean. The combined effects of ENSO and IOD are reflected in the joint anomalies (right column), where the IOD's positive contribution partially offsets ENSO's strong positive influence, creating a more balanced pattern with the strongest positive anomalies continuing to exist in the eastern parts of the region under analysis, including the ocean portion.

The CESM_noENSO experiment exhibits extensive negative anomalies during the negative phase, suggesting that IOD is responsible for the drying effect in East Africa's coastal and southeast regions. The CESM_noIOD experiment, on the other hand, demonstrates notable positive anomalies along central and southern East Africa, which is in line with the IOD's negative phase's localized wetting effect. With IOD-driven positive anomalies along the coast partially offsetting ENSO-driven negative anomalies in core regions, the joint anomalies exhibit a complex spatial structure. In CESM_noENSO and noIOD tests, we found that ENSO and IOD have geographically different effects on East African rainfall variability, with ENSO having a greater influence during the positive phase and a more limited interaction during the negative phase.

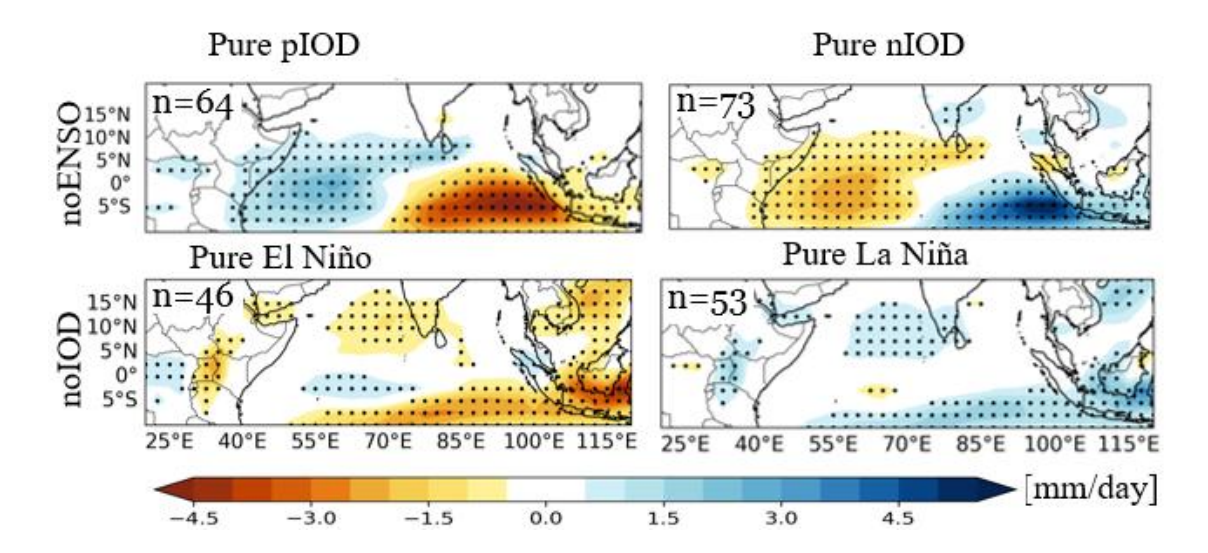


Figure 4.10 Composite rainfall anomaly over East Africa region for OND season from CESM noIOD and noENSO experiments during positive phase (first column) and negative phase (second column). The anomalies are computed concerning climatological models (0801 –1000). The sample size(n) is the number of events that exceed the threshold standard deviation of SST anomaly indices. The Stippling indicates significant composite anomalies (p < 0.05) relative to neutral years.

Furthermore, we applied statistical analysis using the partial correlation technique between SST and rainfall anomalies over East Africa during the OND season, as presented for both observations (OBS) and the CESM_CTRL model (Fig. 4.11). The analysis is divided into two components: (1) the influence of the IOD (DMI) while excluding ENSO (N34), and (2) the influence of ENSO (N34) while excluding the IOD (DMI). This method effectively isolates the independent roles of ENSO and IOD in East African short rainfall variability. Using equation 3, we computed the partial correlations for observations (OBS) and CESM models, the top panel indicates the influence of the IOD (DMI) while excluding ENSO. When we exclude the ENSO signal, strong positive signals are exhibited over equatorial and northern East Africa (5°S–15°N), indicating that a positive IOD event leads to above-normal rainfall in this region. This result aligns with the known IOD mechanism, where warm SST anomalies in the western Indian Ocean enhance convection and moisture transport towards East Africa. While we exclude the roles of ENSO signals for observations (bottom panel), we observed weak or no significant correlations appear over East Africa, suggesting

that ENSO's direct influence on OND rainfall is limited when the IOD is excluded. The spatial pattern indicates that ENSO primarily affects regions outside East Africa, with negative correlations appearing over the western Indian Ocean and positive signals in the central and eastern Indian Ocean. This highlights that ENSO's impact on East African short rains may depend on its interaction with the IOD.

In the CESM_CTRL model, the top panel shows the independent roles of the IOD while excluding ENSO. As observations, the CESM_CTRL model captures a strong positive relationship between the IOD and East African rainfall anomalies. Positive correlations dominate the equatorial and northern East African regions, extending into the western Indian Ocean. Compared to observations, the CESM_CTRL model shows slightly higher strength and spatial extent of these correlations. Nonetheless, the model effectively simulates the critical role of the IOD in modulating East African short rains. CESM_CTRL isolates the role of ENSO while excluding the influence of the IOD. weak or negative correlations are presented over East Africa, highlighting the limited direct influence of ENSO on rainfall in the region. However, significant negative correlations emerge over the Indian Ocean, consistent with ENSO-driven cooling patterns during El Niño events. These findings suggest that ENSO's primary impact on East African rainfall is indirect, often mediated through its interaction with the IOD.

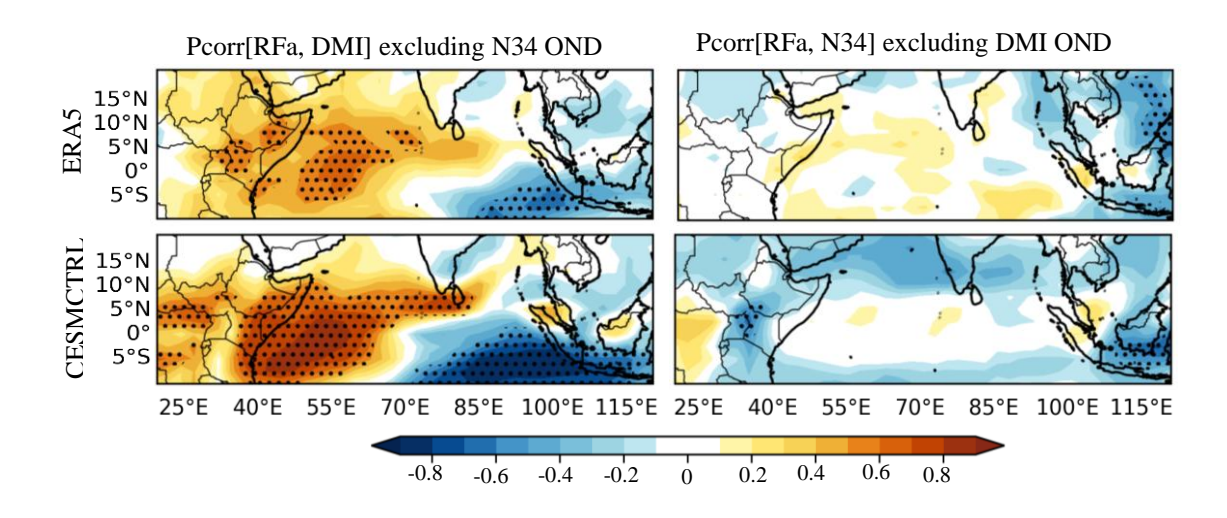


Figure 4.11 Partial correlation between SST indices and rainfall anomaly from the C3S models after excluding Niño-3.4 (upper) and DMI (bottom) during the OND season.

Stippling indicates the area where the correlation between sea surface temperature indices and RF anomaly, which are statistically significant at a 99% confidence level as calculated by a two-sided Student t-test for 22(N-2) degrees of freedom.

4.7 Discussion and Conclusion

In this chapter, we investigate the independent roles of ENSO and IOD in modulating EASR variability from Community Earth System Model (CESM) experiments such as CESM-CT, CESM-noENSO, CESM-noIOD, and CESMamipFULL (atmosphere-only simulation with SSTs coming from the CESM_CTRL coupled). In the analysis, we confirmed that IOD has the dominant role in driving East African short rains during the OND season, as evidenced by strong positive correlations in both observations and the CESM_CTRL and CESM_noIOD experiments. On the other hand, ENSO has a weaker influence, with its impact largely dependent on its interaction with IOD. The CESM_CTRL model performs well in reproducing the observed relationships, making it a valuable tool for understanding the independent contributions of ENSO and IOD to regional climate variability. In summary, the CESM_CTRL model and observational data demonstrate how the Indian Ocean SST variability dominates EASR during the OND season. Positive (negative) IOD SST anomalies exhibit a strong correlation with above-normal (below-normal) rainfall in East Africa. Warm SST anomalies in the western Indian Ocean promote convection and moisture transport to the EA region, which is in line with the known mechanism of the IOD (Ummenhofer et al., 2009). Here in this study, ENSO influence is restricted in the absence of the IOD, as evidenced by the weak or non-existent direct association between East African rainfall and both observations and the CESM model. Nevertheless, ENSO continues to have an impact beyond East Africa, with positive signals in the middle and eastern Indian Ocean and negative correlations over the western Indian Ocean (Schott & Mccreary, 2001). Given the complexity of the mechanisms driving East African short rains (Walker et al., 2020), our results further suggest that ENSO's impact on rainfall is primarily indirect, often facilitated through its interaction with the IOD.

5 GENERAL DISCUSSION

Using observations and models, we assessed the predictability of two major east African rainy seasons i.e. long rain and short rains under seasonal retrospective forecast systems from the C3S. Given our aim, we only considered the forecast initialized at the beginning of the short and long rainy season, namely in September and February, respectively. The predictability East African short rains were evaluated of using eight seasonal retrospective forecast systems from C3S, focusing on September-initialized forecasts. In the seasonal climatology, both models and observational dataset depicts a noticeable rainfall maximum over the central parts of the analysed region, particularly in Congo basin which is far from the coast (see Fig 2.1 in chapter 2 and Fig 4.1 in chapter 4). This feature is typical of the OND season, where rainfall is driven by the seasonal migration of the ITCZ and local monsoon dynamics (Nicholson, 2017).

In terms of ACC, most models demonstrate skill in predicting OND rainfall anomalies across East Africa, with notable biases (Fig. 2.1). Along the East African coast (near Somalia) and parts of the western Indian Ocean, models exhibit skill extending to DJF, likely due to SST persistence in the western Indian Ocean (Fig. 2.6). These findings align with prior studies, such as Behera et al. (2005) and Bahaga et al. (2016). Model skill shows strong inter-annual variability, with skilful years typically coinciding with mature ENSO and IOD phases. While El Niño events are linked to significant rainfall anomalies, the Indian Ocean SST response to ENSO, as indicated by DMI, plays a more influential role than the direct ENSO-driven impacts (e.g., atmospheric bridge). The sign of the DMI reliably predicts the rainfall anomaly sign, unlike Niño3.4. Consistent with Yamagata et al. (2002) and Black et al. (2003), the east-west SST dipole and zonal circulation patterns are key drivers of short rain variability. However, during the 2015/2016 El Niño, most models failed to replicate OND rainfall patterns, except for NCEP and ECCC. This failure is attributed to a weaker positive IOD phase compared to 1997/1998, reducing Indian Ocean Walker circulation intensity (Macleod & Caminade, 2019).

In the third chapter of this study, we also evaluate the predictability of long rainy season using similar models applied in chapter two. The capability of C3S coupled

models to replicate East African rainfall anomalies at consecutive lead seasons i.e. MAM (Lead 1), AMJ (lead 2), and MJJ (lead 3) varies when compared to GPCP data. The significance of ocean-atmosphere interactions as shown by Kebacho & Chen, (2022) the fact that most models exhibit considerable skill across the western Indian Ocean, where comparable correlations remain throughout all seasons (Fig 3.4). While most models consistently showed moderate to high skill throughout East Africa during the short rainy season (Fig. 2.4), the skills in the long rainy season noticed more modeldependent and localized. These is because of long rains (MAM) are driven by a variety of regional and global causes, including ENSO and Indian Ocean dynamics, rather than by a single large-scale phenomenon like the IOD (Kebacho & Chen, 2022b; Vigaud et al., 2017). This fluctuation reflects the intrinsic complexity of these climatic drivers (Nicholson, 2017). According to Funk et al., (2018), East African long rains are more influenced by ENSO when warmer or cooler SSTs occur in the western Pacific. Strong El Niño episodes may be followed by cool La Niña conditions in the East Pacific dry long rainy season relate to higher SSTs in the western equatorial Pacific, while dry conditions during the MAM season are linked to warmer SSTs in the western Pacific. Here, our study also found similar results, with significant correlations between the MAM rainfall index and the N34 index in most models, consistent with the observational dataset. This indicates a robust connection between ENSO events and East African long rains (as shown in Figures 3.6, 3.7, and Table 3.1).

The Walker circulation, which reduces the magnitude of rainfall during long rainy season which is reinforced by warmer SSTs over the western Pacific (Roy et al., 2024). For example, during 2016–2017, this SST pattern caused droughts and dry seasons to follow one another (Funk et al., 2018). Because the IOD peaks months later, from September to November, than the long rains, variations in the long rains are less susceptible to changes in IOD (Shaaban and Roundy, 2017). In our study, we confirm this finding: both observational datasets and model simulations consistently show lower rainfall variability during the long rains. Similar to the GPCP climatology, most coupled models indicate less MAM rainfall variability, particularly in the northern regions of East Africa (Fig 3.2). However, during short rainy season the rainfall variability is higher as evident in both observational dataset and most c3s models. As

shown in Fig 3.4 most c3s models depicts skill in over ocean and Eastern parts of the analysed region, but perform less well or inconsistently, especially in northern and western EA regions. The successful predicted year that we identified (Fig. 3.5) is associated with the strongest El Niño event on record (1997/1998), East Africa experienced the largest positive RFa during MAM season (Fig. 3.1 k) however less in magnitude compared to OND season (presented in Fig. 2.1 k). Additionally, there are considerable differences in the skill amongst models, suggesting that over East Africa, it is difficult to consistently capture the complex links between ocean-atmosphere coupling, regional moisture transport during the long rains (Nicholson, 2018).

The East African regional rainfall variability is frequently determined by the interplay between ENSO and IOD (Wang et al., 2019). The Indian Ocean's atmospheric circulation patterns can be altered by positive ENSO phases, which are defined by warm SSTs in the central and eastern Pacific (Shaaban, 2015). Depending on the IOD phase, these modifications may intensify or lessen rainfall anomalies brought on by the IOD (McMonigal & Larson, 2022). On the other hand, when ENSO is not present, the IOD uses its well-established mechanism of SST-induced convection changes to independently generate regional rainfall variability (Roy et al., 2024). This is true as Behera et al. (2005) and Yamagata et al. (2003) stated that 79% of the extreme years of short rains are associated with IOD anomalous years using the SINTEX-F1 model. It is therefore natural to expect that the atmospheric circulation change associated with the IOD is a major driver of the anomalous short rains. To understand the independent roles of IOD and ENSO on East African short rain variability, we investigated using the CESM experiments analysis. Consistent to previous studies (Luo et al., 2010; Wang et al., 2019) we noticed significant correlation between positive OND rainfall and IOD phases. In the observational data set (ERA5), EASRi shows a moderate positive correlation with N34 (r = 0.57) and a stronger correlation with DMI (r = 0.79), indicating that the IOD has a dominant influence on East African short rains (Fig. 4.7). The association between the DMI and the East African Short Rain Index (EASRi) peaks during boreal fall, aligning with the short rains season and supporting previous findings (Behera et., 2005). These values remain largely unchanged even when the influence of Niño3.4 is excluded, indicating the robust role of the IOD. Both simple and partial

correlation coefficients in the model align well with observations. Thus, the IOD's crucial significance is further highlighted by the noticeably reduced rainfall responses depicted in the suppressed IOD variability experiment (CESM-noIOD). These results are consistent with previous studies (Saji et al., 1999 and Behera et al., 2005) they found that the IOD to be a major cause of rainfall anomalies in East Africa, where as ENSO's direct influence on EASR is comparatively weaker, as evidenced by weak correlations between ENSO and rainfall in both observations and CESM_CTRL simulations (Fig 4.9). ENSO's impact is more pronounced when it interacts with the IOD, emphasizing its indirect role. For instance, during concurrent positive ENSO and positive IOD events, the rainfall anomalies are amplified, highlighting the synergistic effects of these phenomena. Without the IOD, as in the CESM-noIOD experiment, ENSO's influence on EASR is minimal. This is consistent with findings from studies like Black et al. (2003), which reported limited ENSO impacts on East African rainfall when isolated from IOD variability.

6 GENERAL CONCLUSIONS

This PhD thesis aims to examine the predictability of seasonal rainfall patterns and investigate the roles of ENSO and IOD that influence the two major rainy seasons (long rains, MAM, and short rains, OND) over East Africa. First, we evaluated the predictive skill of eight coupled ocean-atmosphere seasonal prediction models provided by C3S in reproducing the East African rainfall pattern. While most models show significant mean rainfall biases over highlands, they generally perform well in predicting OND rainfall anomalies over the coastal region. However, their skill is limited or absent in some northern and western areas. Along the Somali coast and over parts of the Western Indian Ocean, models demonstrate notable skill, up to lead season 3, which is linked to the persistence of SST anomalies in the Western Indian Ocean. However, during the long rainy season, models perform more accurately in reproducing rainfall anomaly during ENSO years than during IOD phases, indicating that large-scale interactions between atmospheric and oceanic conditions influence the long rain patterns of the East African region.

In 1997 and 1998, the model's strong performance compared to persistence forecasts often coincided with the mature phases of ENSO and IOD. The IOD, tracked using the DMI, effectively predicts the sign of OND rainfall anomalies. Despite East Africa's proximity to the IOD's west pole, the correlation between short rains and IOD is strongest when both east and west poles are considered. This suggests that broader-scale IOD variability, associated with changes in the Walker Circulation, drives East African rainfall variability more than localized SST fluctuations. Long rainy season patterns appear to be more impacted by large-scale atmospheric-oceanic interactions, as the models demonstrate higher predictive skill in simulating the MAM season during ENSO compared to IOD years.

Using CESM experiments, we demonstrated that IOD exerts a stronger influence than ENSO (Niño3.4) on East African short rains during the OND season. Observations from ERA5 show a moderate positive correlation between EASRi and Niño3.4 (r = 0.57) but a much stronger correlation with DMI (r = 0.79), suggesting the IOD's dominant role. CESM simulations further support this, showing weaker

correlations between EASRi and Niño3.4 (r = 0.28-0.23), while the DMI consistently maintains high correlations (r = 0.81-0.83). The noIOD experiment reveals a negative correlation between Niño3.4 and EASRi (r = -0.53), confirming that ENSO alone is insufficient to produce favourable rainfall anomalies. Conversely, the noENSO experiment retains a strong correlation between DMI and EASRi, affirming the IOD's independent and robust influence on rainfall patterns.

Overall, we found that the IOD has a critical role in shaping East African short rains, with ENSO having a smaller role. The IOD's influence remains significant even when ENSO variability is excluded, highlighting its capacity to drive rainfall anomalies independently. These findings align with prior research and underscore the importance of the IOD in regulating rainfall during the OND season, particularly in CESM simulations, where its dominance is evident across different experimental setups. This study offers valuable insights into the predictability of East African rainfall; however, several limitations should be acknowledged. Notably, the analysis does not fully account for other potential drivers such as regional topography, tropical circulation systems, and local land-atmosphere interactions beyond ENSO and IOD. Additionally, the limited spatial resolution of the models may hinder their ability to capture localized weather systems, likely contributing to the observed biases. Therefore, addressing the sources of rainfall bias should be a primary focus of future research, as dynamical models consistently exhibit notable errors over many East African highland regions and parts of the western Indian Ocean. Moreover, in our area of interest (East Africa), limited availability and accuracy of observational datasets, such as station-based rainfall measurements, may introduce additional uncertainties in model validation.

REFERENCES

- Adler, R. F., Huffman, G. J., Chang, A., Ferraro, R., Xie, P.-P., Janowiak, J., Rudolf, B., Schneider, U., Curtis, S., Bolvin, D., Gruber, A., Susskind, J., Arkin, P., And, ##,
 & Nelkin, E. (2003). The Version-2 Global Precipitation Climatology Project (GPCP) Monthly Precipitation Analysis (1979-Present).
 http://precip.gsfc.nasa.gov
- Amha, Y., Demissie, T., Amdihun, A., Otieno, V., Afiesimama, E., Murombedzi, J., & Radeny, M. (2023a). *Unrelenting catastrophic droughts and successive failed rainy seasons in the Greater Horn of Africa What can we do better to protect millions of smallholder farmers and livestock keepers from extreme weather and climate crisis?*
- Amha, Y., Demissie, T., Amdihun, A., Otieno, V., Afiesimama, E., Murombedzi, J., & Radeny, M. (2023b). *Unrelenting catastrophic droughts and successive failed rainy seasons in the Greater Horn of Africa What can we do better to protect millions of smallholder farmers and livestock keepers from extreme weather and climate crisis?*
- Ashok, K., Behera, S. K., Rao, S. A., Weng, H., & Yamagata, T. (2007). El Niño Modoki and its possible teleconnection. *Journal of Geophysical Research: Oceans*, 112(11). https://doi.org/10.1029/2006JC003798
- Bahaga, T. K., Kucharski, F., Tsidu, G. M., & Yang, H. (2016). Assessment of prediction and predictability of short rains over equatorial East Africa using a multi-model ensemble. *Theoretical and Applied Climatology*, *123*(3–4), 637–649. https://doi.org/10.1007/s00704-014-1370-1
- Behera, S. K., Luo, J.-J., Masson, S., Delecluse, P., Gualdi, S., & Navarra, A. (2005). Paramount Impact of the Indian Ocean Dipole on the East African Short Rains: A CGCM Study.

- Berhane, F., & Zaitchik, B. (n.d.). *Modulation of Daily Precipitation over East Africa* by the Madden-Julian Oscillation*. https://doi.org/10.1175/JCLI-D-13
- Cai, W., Van Rensch, P., Cowan, T., & Hendon, H. H. (2012). An Asymmetry in the IOD and ENSO teleconnection pathway and its impact on australian climate. *Journal of Climate*, *25*(18), 6318–6329. https://doi.org/10.1175/JCLI-D-11-00501.1
- Camberlin, P., & Philippon, N. (2002). *The East African March-May Rainy Season:*Associated Atmospheric Dynamics and Predictability over the 1968-97 Period.
- Cherchi, A., & Navarra, A. (2013). Influence of ENSO and of the Indian Ocean Dipole on the Indian summer monsoon variability. *Climate Dynamics*, *41*(1), 81–103. https://doi.org/10.1007/s00382-012-1602-y
- Christensen, H. M., & Berner, J. (2019). From reliable weather forecasts to skilful climate response: A dynamical systems approach. *Quarterly Journal of the Royal Meteorological Society*, 145(720), 1052–1069. https://doi.org/10.1002/qj.3476
- Deser, C., Guo, R., & Lehner, F. (2017). The relative contributions of tropical Pacific sea surface temperatures and atmospheric internal variability to the recent global warming hiatus. *Geophysical Research Letters*, *44*(15), 7945–7954. https://doi.org/10.1002/2017GL074273
- Doi, T., Behera, S. K., & Yamagata, T. (2022). On the predictability of the extreme drought in East Africa during the short rains season. *Geophysical Research Letters*. https://doi.org/10.1029/2022gl100905
- Endris, H. S., Lennard, C., Hewitson, B., Dosio, A., Nikulin, G., & Artan, G. A. (2019). Future changes in rainfall associated with ENSO, IOD and changes in the mean state over Eastern Africa. *Climate Dynamics*, *52*(3–4), 2029–2053. https://doi.org/10.1007/s00382-018-4239-7

- Fischer, A. S., Terray, P., Gualdi, S., & Delecluse, P. (2005). *Two Independent Triggers for the Indian Ocean Dipole/Zonal Mode in a Coupled GCM*.
- Funk, C., Harrison, L., Shukla, S., Pomposi, C., Galu, G., Korecha, D., Husak, G., Magadzire, T., Davenport, F., Hillbruner, C., Eilerts, G., Zaitchik, B., & Verdin, J. (2018). Examining the role of unusually warm Indo-Pacific sea-surface temperatures in recent African droughts. *Quarterly Journal of the Royal Meteorological Society*, 144, 360–383. https://doi.org/10.1002/qj.3266
- Gebremeskel, G., Tang, Q., Sun, S., Huang, Z., Zhang, X., & Liu, X. (2019). Droughts in East Africa: Causes, impacts and resilience. In *Earth-Science Reviews* (Vol. 193, pp. 146–161). Elsevier B.V. https://doi.org/10.1016/j.earscirev.2019.04.015
- Gebremeskel Haile, G., Tang, Q., Leng, G., Jia, G., Wang, J., Cai, D., Sun, S., Baniya, B., & Zhang, Q. (2020). Long-term spatiotemporal variation of drought patterns over the Greater Horn of Africa. *Science of the Total Environment*, 704. https://doi.org/10.1016/j.scitotenv.2019.135299
- Gualdi, S., Borrelli, A., Davoli, G., Masina, S., Navarra, A., Sanna, A., Tibaldi, S., & Cantelli, A. (2020). *The new CMCC Operational Seasonal Prediction System Issue TN0288 CMCC Technical Notes*. https://doi.org/10.25424/CMCC/SPS3.5
- Hamilton, H. L., Núñez Ocasio, K. M., Evans, J. L., Young, G. S., & Fuentes, J. D. (2020). Topographic Influence on the African Easterly Jet and African Easterly Wave Energetics. *Journal of Geophysical Research: Atmospheres*, 125(8). https://doi.org/10.1029/2019JD032138
- Hitoshi, Y., Chihiro, M., Takashi, N., Takafumi, K., Takayuki, T., Kazutaka, Y., Ryoji, N., Yukimasa, A., & Ryouhei, S. (2020). *Upgrade of JMA's Operational Global Model*. http://oceans11.lanl.gov/trac/CICE.

- Hoell, A., & Funk, C. (2014). Indo-Pacific sea surface temperature influences on failed consecutive rainy seasons over eastern Africa. *Climate Dynamics*, *43*(5–6), 1645–1660. https://doi.org/10.1007/s00382-013-1991-6
- Hogan, E., Shelly, A., & Xavier, P. (2015). The observed and modelled influence of the Madden-Julian Oscillation on East African rainfall. *Meteorological Applications*, *22*(3), 459–469. https://doi.org/10.1002/met.1475
- Huffman, G. J., Adler, R. F., Behrangi, A., Bolvin, D. T., Nelkin, E. J., Guojun, G. U., & Ehsani, M. R. (2023). The New Version 3.2 Global Precipitation Climatology Project (GPCP) Monthly and Daily Precipitation Products. *Journal of Climate*, 36(21), 7635–7655. https://doi.org/10.1175/JCLI-D-23-0123.1
- Indeje, M., Semazzi, F. H. M., & Ogallo, L. J. (2000). ENSO signals in East African rainfall seasons. *International Journal of Climatology*, 20(1), 19–46. https://doi.org/10.1002/(SICI)1097-0088(200001)20:1<19::AID-JOC449>3.0.CO;2-0
- Izumo, T., Vialard, J., Lengaigne, M., De Boyer Montegut, C., Behera, S. K., Luo, J. J., Cravatte, S., Masson, S., & Yamagata, T. (2010). Influence of the state of the Indian Ocean Dipole on the following years El Nío. *Nature Geoscience*, *3*(3), 168–172. https://doi.org/10.1038/ngeo760
- Kebacho, L. L., & Chen, H. (2022a). The dominant modes of the long rains interannual variability over Tanzania and their oceanic drivers. *International Journal of Climatology*, 42(10), 5273–5292. https://doi.org/10.1002/joc.7532
- Kebacho, L. L., & Chen, H. (2022b). The dominant modes of the long rains interannual variability over Tanzania and their oceanic drivers. *International Journal of Climatology*, 42(10), 5273–5292. https://doi.org/10.1002/joc.7532
- Kimani, M., Hoedjes, J. C. B., & Su, Z. (2020). An assessment of MJO circulation influence on air-sea interactions for improved seasonal rainfall predictions

- over East Africa. *Journal of Climate*, *33*(19), 8367–8379. https://doi.org/10.1175/JCLI-D-19-0296.1
- Lashkari, H., & Jafari, M. (2021). Annual displacement and appropriate index to determine ITCZ position in East Africa and the Indian Ocean regions. *Meteorology and Atmospheric Physics*, 133(4), 1111–1126. https://doi.org/10.1007/s00703-021-00797-y
- Lauriane Baté Laurent Dorec, C. A. J.-F. G. (2021). *Documentaton of the METEO-FRANCE seasonal forecastng system 8 Officiac reference nueber ser* □ *ice contract:* 2018/C3S_330_Météo-France/SC1 ECMWF COPERNICUS REPORT.
- Lestari, R. K., & Koh, T. Y. (2016). Statistical Evidence for Asymmetry in ENSO–IOD Interactions. *Atmosphere Ocean*, 54(5), 498–504. https://doi.org/10.1080/07055900.2016.1211084
- Liguori, G., & Di Lorenzo, E. (2019). Separating the North and South Pacific Meridional Modes Contributions to ENSO and Tropical Decadal Variability. *Geophysical Research Letters*, 46(2), 906–915. https://doi.org/10.1029/2018GL080320
- Liguori, G., McGregor, S., Singh, M., Arblaster, J., & Di Lorenzo, E. (2022). Revisiting ENSO and IOD Contributions to Australian Precipitation. In *Geophysical Research Letters* (Vol. 49, Issue 1). John Wiley and Sons Inc. https://doi.org/10.1029/2021GL094295
- Luo, J. J., Masson, S., Behera, S., & Yamagata, T. (2007). Experimental forecasts of the Indian Ocean dipole using a coupled OAGCM. *Journal of Climate*, *20*(10), 2178–2190. https://doi.org/10.1175/JCLI4132.1
- Lyon, B. (2014). Seasonal drought in the Greater Horn of Africa and its recent increase during the March-May long rains. *Journal of Climate*, *27*(21), 7953–7975. https://doi.org/10.1175/JCLI-D-13-00459.1

- MacLeod, D. (2019a). Seasonal forecasts of the East African long rains: insight from atmospheric relaxation experiments. *Climate Dynamics*, *53*(7–8), 4505–4520. https://doi.org/10.1007/s00382-019-04800-6
- MacLeod, D. (2019b). Seasonal forecasts of the East African long rains: insight from atmospheric relaxation experiments. *Climate Dynamics*, *53*(7–8), 4505–4520. https://doi.org/10.1007/s00382-019-04800-6
- Manzanas, R. (2020). Assessment of Model Drifts in Seasonal Forecasting:

 Sensitivity to Ensemble Size and Implications for Bias Correction. *Journal of Advances in Modeling Earth Systems*, 12(3).

 https://doi.org/10.1029/2019MS001751
- Marathe, S., Ashok, K., Swapna, P., & Sabin, T. P. (2015). Revisiting El Niño Modokis. *Climate Dynamics*, 45(11–12), 3527–3545. https://doi.org/10.1007/s00382-015-2555-8
- McGee, D., Donohoe, A., Marshall, J., & Ferreira, D. (2014). Changes in ITCZ location and cross-equatorial heat transport at the Last Glacial Maximum, Heinrich Stadial 1, and the mid-Holocene. *Earth and Planetary Science Letters*, *390*, 69–79. https://doi.org/10.1016/j.epsl.2013.12.043
- McMonigal, K., & Larson, S. M. (2022). ENSO Explains the Link Between Indian Ocean Dipole and Meridional Ocean Heat Transport. *Geophysical Research Letters*, 49(2). https://doi.org/10.1029/2021GL095796
- Merryfield, W. J., Baehr, J., Batté, L., Becker, E. J., Butler, A. H., Coelho, C. A. S., Danabasoglu, G., Dirmeyer, P. A., Doblas-Reyes, F. J., Domeisen, D. I. V., Ferranti, L., Ilynia, T., Kumar, A., Müller, W. A., Rixen, M., Robertson, A. W., Smith, D. M., Takaya, Y., Tuma, M., ... Yeager, S. (2020). Current and emerging developments in subseasonal to decadal prediction. *Bulletin of the American Meteorological Society*, 101(6), E869–E896. https://doi.org/10.1175/BAMS-D-19-0037.1

- Merryfield, W. J., Lee, W. S., Boer, G. J., Kharin, V. V., Scinocca, J. F., Flato, G. M., Ajayamohan, R. S., Fyfe, J. C., Tang, Y., & Polavarapu, S. (2013). The canadian seasonal to interannual prediction system. part I: Models and initialization. *Monthly Weather Review*, 141(8), 2910–2945. https://doi.org/10.1175/MWR-D-12-00216.1
- Murtugudde, R., McCreary, J. P., & Busalacchi, A. J. (2000). Oceanic processes associated with anomalous events in the Indian Ocean with relevance to 1997-1998. In *Journal of Geophysical Research: Oceans* (Vol. 105, Issue C2, pp. 3295–3306). Blackwell Publishing Ltd. https://doi.org/10.1029/1999jc900294
- Navarra, A., Tribbia, J., & Conti, G. (2013). Atmosphere-ocean interactions at strong couplings in a simple model of El Niño. *Journal of Climate*, *26*(23), 9633–9654. https://doi.org/10.1175/JCLI-D-12-00763.1
- Nicholson, S. E. (2017). Climate and climatic variability of rainfall over eastern Africa. *Reviews of Geophysics*, 55(3), 590–635. https://doi.org/10.1002/2016RG000544
- Nicholson, S. E. (2018a). The ITCZ and the seasonal cycle over equatorial Africa. Bulletin of the American Meteorological Society, 99(2), 337–348. https://doi.org/10.1175/BAMS-D-16-0287.1
- Nicholson, S. E. (2018b). The ITCZ and the seasonal cycle over equatorial Africa. *Bulletin of the American Meteorological Society*, 99(2), 337–348. https://doi.org/10.1175/BAMS-D-16-0287.1
- Nicolì, D., Bellucci, A., Ruggieri, P., Athanasiadis, P. J., Materia, S., Peano, D., Fedele, G., Hénin, R., & Gualdi, S. (2023). The Euro-Mediterranean Center on Climate Change (CMCC) decadal prediction system. *Geoscientific Model Development*, 16(1), 179–197. https://doi.org/10.5194/gmd-16-179-2023

- Oelfke, C., And, C., Webster, P. J., & Cole, J. E. (2003). *Interdecadal Variability of the Relationship between the Indian Ocean Zonal Mode and East African Coastal Rainfall Anomalies*.
- Ogutu, G. E. O., Franssen, W. H. P., Supit, I., Omondi, P., & Hutjes, R. W. A. (2017). Skill of ECMWF system-4 ensemble seasonal climate forecasts for East Africa. *International Journal of Climatology*, *37*(5), 2734–2756. https://doi.org/10.1002/joc.4876
- Onyutha, C., Ayugi, B., Tabari, H., Ngoma, H., & Ongoma, V. (2022). Drought across East Africa under climate variability. In *Climate Impacts on Extreme Weather:*Current to Future Changes on a Local to Global Scale (pp. 159–173). Elsevier. https://doi.org/10.1016/B978-0-323-88456-3.00002-2
- Palmer, P. I., Wainwright, C. M., Dong, B., Maidment, R. I., Wheeler, K. G., Gedney, N., Hickman, J. E., Madani, N., Folwell, S. S., Abdo, G., Allan, R. P., Black, E. C. L., Feng, L., Gudoshava, M., Haines, K., Huntingford, C., Kilavi, M., Lunt, M. F., Shaaban, A., & Turner, A. G. (2023a). Drivers and impacts of Eastern African rainfall variability. In *Nature Reviews Earth and Environment* (Vol. 4, Issue 4, pp. 254–270). Springer Nature. https://doi.org/10.1038/s43017-023-00397-x
- Palmer, Wainwright, C. M., Dong, B., Maidment, R. I., Wheeler, K. G., Gedney, N., Hickman, J. E., Madani, N., Folwell, S. S., Abdo, G., Allan, R. P., Black, E. C. L., Feng, L., Gudoshava, M., Haines, K., Huntingford, C., Kilavi, M., Lunt, M. F., Shaaban, A., & Turner, A. G. (2023b). Drivers and impacts of Eastern African rainfall variability. In *Nature Reviews Earth and Environment*. Springer Nature. https://doi.org/10.1038/s43017-023-00397-x
- Park, S., Kang, D., Yoo, C., Im, J., & Lee, M. I. (2020). Recent ENSO influence on East African drought during rainy seasons through the synergistic use of satellite and reanalysis data. *ISPRS Journal of Photogrammetry and Remote Sensing*, 162, 17–26. https://doi.org/10.1016/j.isprsjprs.2020.02.003

- Parker, W. S. (2010). Predicting weather and climate: Uncertainty, ensembles and probability. *Studies in History and Philosophy of Science Part B Studies in History and Philosophy of Modern Physics*, 41(3), 263–272. https://doi.org/10.1016/j.shpsb.2010.07.006
- Pohl, B., & Camberlin, P. (2006). Influence of the Madden-Julian Oscillation on East African rainfall. I: Intraseasonal variability and regional dependency. *Quarterly Journal of the Royal Meteorological Society*, 132(621), 2521–2539. https://doi.org/10.1256/qj.05.104
- Preethi, B., Sabin, T. P., Adedoyin, J. A., & Ashok, K. (2015a). Impacts of the ENSO Modoki and other tropical indo-pacific climate-drivers on African rainfall. *Scientific Reports*, *5*. https://doi.org/10.1038/srep16653
- Preethi, B., Sabin, T. P., Adedoyin, J. A., & Ashok, K. (2015b). Impacts of the ENSO Modoki and other tropical indo-pacific climate-drivers on African rainfall. *Scientific Reports*, *5*. https://doi.org/10.1038/srep16653
- Rao, S. A., Behera, S. K., Masumoto, Y., & Yamagata, T. (2002). Interannual subsurface variability in the Tropical Indian Ocean with a special emphasis on the Indian Ocean Dipole. In *Deep-Sea Research II* (Vol. 49). www.ifremer.fr/sismer
- Roy, I., Mliwa, M., & Troccoli, A. (2024). Important drivers of East African monsoon variability and improving rainy season onset prediction. *Natural Hazards*, *120*(1), 429–445. https://doi.org/10.1007/s11069-023-06223-3
- Saha, S., Moorthi, S., Wu, X., Wang, J., Nadiga, S., Tripp, P., Behringer, D., Hou, Y. T., Chuang, H. Y., Iredell, M., Ek, M., Meng, J., Yang, R., Mendez, M. P., Van Den Dool, H., Zhang, Q., Wang, W., Chen, M., & Becker, E. (2014). The NCEP climate forecast system version 2. *Journal of Climate*, 27(6), 2185–2208. https://doi.org/10.1175/JCLI-D-12-00823.1
- Saji N., Goswami B., Vinayachandran P., & Yamagata T. (1999). A dipole mode in the tropical Indian Ocean. *Letters to Nature*.

- Schott, F. A., & Mccreary, J. P. (2001). The monsoon circulation of the Indian Ocean. In *Progress in Oceanography* (Vol. 51). www.elsevier.com/locate/pocean
- Schreck, C. J., & Semazzi, F. H. M. (2004). Variability of the recent climate of eastern Africa. *International Journal of Climatology*, 24(6), 681–701. https://doi.org/10.1002/joc.1019
- Shaaban, A. A. (2015). Modulation of East African Precipitation by the Indian Ocean Dipole (IOD) and ENSO.
- Sillmann, J., Thorarinsdottir, T., Keenlyside, N., Schaller, N., Alexander, L. V., Hegerl, G., Seneviratne, S. I., Vautard, R., Zhang, X., & Zwiers, F. W. (2017). Understanding, modeling and predicting weather and climate extremes: Challenges and opportunities. In *Weather and Climate Extremes* (Vol. 18, pp. 65–74). Elsevier B.V. https://doi.org/10.1016/j.wace.2017.10.003
- Stevens, B., Giorgetta, M., Esch, M., Mauritsen, T., Crueger, T., Rast, S., Salzmann, M., Schmidt, H., Bader, J., Block, K., Brokopf, R., Fast, I., Kinne, S., Kornblueh, L., Lohmann, U., Pincus, R., Reichler, T., & Roeckner, E. (2013). Atmospheric component of the MPI-M earth system model: ECHAM6. *Journal of Advances in Modeling Earth Systems*, *5*(2), 146–172. https://doi.org/10.1002/jame.20015
- Ummenhofer, C. C., Gupta, A. Sen, England, M. H., & Reason, C. J. C. (2009). Contributions of Indian Ocean sea surface temperatures to enhanced East African rainfall. *Journal of Climate*, *22*(4), 993–1013. https://doi.org/10.1175/2008JCLI2493.1
- Vellinga, M., & Milton, S. F. (2018a). Drivers of interannual variability of the East African "Long Rains." *Quarterly Journal of the Royal Meteorological Society*, 144(712), 861–876. https://doi.org/10.1002/qj.3263
- Vellinga, M., & Milton, S. F. (2018b). Drivers of interannual variability of the East African "Long Rains." *Quarterly Journal of the Royal Meteorological Society*, 144(712), 861–876. https://doi.org/10.1002/qj.3263

- Vigaud, N., Lyon, B., & Giannini, A. (2017). Sub-seasonal teleconnections between convection over the Indian Ocean, the East African long rains and tropical Pacific surface temperatures. *International Journal of Climatology*, *37*(3), 1167–1180. https://doi.org/10.1002/joc.4765
- Viste, E., & Sorteberg, A. (2013). The effect of moisture transport variability on Ethiopian summer precipitation. *International Journal of Climatology*, *33*(15), 3106–3123. https://doi.org/10.1002/joc.3566
- Walker, D. P., Birch, C. E., Marsham, J. H., Scaife, A. A., Graham, R. J., & Segele, Z. T. (2019). Skill of dynamical and GHACOF consensus seasonal forecasts of East African rainfall. *Climate Dynamics*, *53*(7–8), 4911–4935. https://doi.org/10.1007/s00382-019-04835-9
- Wang, H., Kumar, A., Murtugudde, R., Narapusetty, B., & Seip, K. L. (2019). Covariations between the Indian Ocean dipole and ENSO: a modeling study. *Climate Dynamics*, *53*(9–10), 5743–5761. https://doi.org/10.1007/s00382-019-04895-x
- Webster et al 1999 Coupled Ocean–atmosphere dynamics in the Indian Ocean during 1997–98. (n.d.).
- Wilks D. (2011). Series Editors. In *Statistical Methods in the Atmospheric Sciences* (p. ii). Academic Press. https://doi.org/10.1016/b978-0-12-385022-5.00022-1
- Williams, A. P., & Funk, C. (2011). A westward extension of the warm pool leads to a westward extension of the Walker circulation, drying eastern Africa. *Climate Dynamics*, *37*(11–12), 2417–2435. https://doi.org/10.1007/s00382-010-0984-y
- Xue, J., Luo, J. J., Zhang, W., & Yamagata, T. (2022). ENSO-IOD Inter-Basin Connection Is Controlled by the Atlantic Multidecadal Oscillation. *Geophysical Research Letters*, 49(24). https://doi.org/10.1029/2022GL101571

- Yamagata, T., Behera, S. K., Rao, S. A., Guan, Z., Ashok, K., & Saji, H. N. (2003).

 American Meteorological Society Comments on "Dipoles, Temperature Gradients, and Tropical Climate Anomalies." *Source: Bulletin of the American Meteorological Society*, 84(10), 1418–1422. https://doi.org/10.2307/26216895
- Yang, W., Seager, R., Cane, M. A., & Lyon, B. (2014a). The East African long rains in observations and models. *Journal of Climate*, *27*(19), 7185–7202. https://doi.org/10.1175/JCLI-D-13-00447.1
- Yang, W., Seager, R., Cane, M. A., & Lyon, B. (2014b). The East African long rains in observations and models. *Journal of Climate*, *27*(19), 7185–7202. https://doi.org/10.1175/JCLI-D-13-00447.1
- Zhang, C. (2005). Madden-Julian Oscillation. In *Reviews of Geophysics* (Vol. 43, Issue 2, pp. 1–36). https://doi.org/10.1029/2004RG000158
- Zhang, L., Han, W., Karnauskas, K. B., Meehl, G. A., Hu, A., Rosenbloom, N., & Shinoda, T. (2019). Indian Ocean Warming Trend Reduces Pacific Warming Response to Anthropogenic Greenhouse Gases: An Interbasin Thermostat Mechanism. *Geophysical Research Letters*, 46(19), 10882–10890. https://doi.org/10.1029/2019GL084088
- Zhao, S., & Cook, K. H. (2021). Influence of Walker circulations on East African rainfall. *Climate Dynamics*, 56(7–8), 2127–2147. https://doi.org/10.1007/s00382-020-05579-7